TWO YEARS OF AEROSOL PROPERTIES AND DIRECT RADIATIVE EFFECTS MEASURED AT A REPRESENTATIVE SOUTHEASTERN U.S. SITE

A Thesis
by
William Bullitt Beuttell Jr

Submitted to the Graduate School
Appalachian State University
In partial fulfillment of the requirements for the degree of
MASTER OF SCIENCE

December 2011
Department of Physics and Astronomy

TWO YEARS OF AEROSOL PROPERTIES AND DIRECT RADIATIVE EFFECTS MEASURED AT A REPRESENTATIVE SOUTHEASTERN U.S. SITE

A Thesis
by
William Bullitt Beuttell, Jr
December 2011

APPROVED BY:

_____
James P. Sherman
Chairperson, Thesis Committee

_____
Brett F. Taubman
Member, Thesis Committee

_____
Rahman Tashakkori
Member, Thesis Committee

_____
Michael Briley
Chairperson, Department of Physics and Astronomy

_____
Edelma D. Huntley
Dean, Research and Graduate Studies

FOREWORD

The research detailed in this thesis will be submitted to The Journal of Atmospheric Chemistry and Physics (ACP), an international peer-reviewed open access journal operated by the European Geosciences Union which is published by Copernicus Publications. The thesis has been prepared according to their journal submission criteria.

ABSTRACT

TWO YEARS OF AEROSOL PROPERTIES AND DIRECT RADIATIVE EFFECTS MEASURED AT A REPRESENTATIVE SOUTHEASTERN U.S. SITE

William Bullitt Beuttell, Jr, B.S., Appalachian State University

M.S., Appalachian State University

Chairperson: James P. Sherman Ph.D

The southeastern U.S. is one of only a small number of regions worldwide which has not exhibited warming over the past century. Recent studies (Goldstein et al., 2009) show that negative aerosol direct radiative effects are consistent with a warm-season regional cooling effect linked to secondary organic aerosol loading. Two years of NOAA-ESRL supported aerosol measurements made at the Appalachian Atmospheric Interdisciplinary Research (AppalAIR) facility at Appalachian State University (36.214 N, 81.693 W, 1080m ASL) are presented, along with satellite-based measurements (MODIS-Aqua) of aerosol optical depth, cloud fraction, and surface albedo. Aerosol optical property statistics are placed in the context of those made at other U.S. ESRL stations. Direct aerosol radiative effect calculations reveal high seasonal variability, with negative broadband summer forcing values of $\sim$ -10 W/m^2 (-4W/m^2) when actual (standard) cloud fraction, surface albedo, and single-scattering albedo values are used. Hierarchical cluster analyses were used to broadly classify

the aerosol source types that influence the Southeastern U.S. aerosol optical properties.

Recently-added aerosol hygroscopic growth measurements (a sample of which are presented) will facilitate improved aerosol source type classification and aerosol light scattering humidity dependence scaling of direct radiative effect calculations.

DEDICATION

I would like to dedicate this thesis to four people. The first is the late Dr. Andrew Graham, who was instrumental in helping me pursue physics as an undergraduate major by providing guidance and friendship during a key period of my life. I must also dedicate this thesis to my mother, father, and brother. Without their continued support and unwavering love, I would not have been capable of accomplishing my goals or pursuing a stimulating and prosperous life. Thank you Mom, Dad, and Adam, I love you all and would be lost without you.

ACKNOWLEDGEMENTS

Funding for this research was made possible by the Graduate Research Associate Mentor (GRAM) program. I received funding from this program in the form of a two-year assistantship provided through the Appalachian State University Cratis D. Williams Graduate School. Without the GRAM program support none of this would have been possible.

In addition to the funding agent of this research, a large amount of thanks must go out to several individuals for their assistance, guidance and mentorship through my current graduate career. My thesis committee members which include Dr. James (Jim) Sherman, Dr. Brett F. Taubman, Dr. Rahman Tashikori; the entire NOAA Earth Systems Research Laboratory (ESRL) Aerosols research group, and Dr. Patrick Sheridan.

Several publicly available data retrieval services must be acknowledged for their support in this research. NASA Land Processes Distributed Active Archive Center (LP DAAC) for calculating and providing MODIS remotely sensed satellite data products. Oak Ridge National Laboratory (ORNL) Distributed Active Archive Center for Biogeochemical Dynamics (DAAC) for providing MODIS Land Product Subsets of surface reflectance at multiple wavelengths. NASA Aerosol Robotic Network (AERONET) for providing Ångström Exponents used to scale aerosol optical depths from 550nm to 700nm.

TABLE OF CONTENTS

LIST OF TABLES

LIST OF FIGURES

LIST OF ACRONYMS

AAE: Absorption Ångström Exponent

AERONET: AErosol RObotic NETwork

AOD: Aerosol Optical Depth

APP: NOAA ESRL Aerosol site location index for Appalachian State University located in Boone, NC

AppalAIR: Appalachian State University Atmospheric Interdisciplinary Research

BND: Bondville, IL Research site, part of the NOAA ESRL Aerosol Network.

CRDS: Cavity Ring-Down Spectrometer

DRE: Direct Radiative Effect

IPCC: Intergovernmental Panel on Climate Change

LIDAR: Light Detection and Ranging

MODIS: Moderate Resolution Imaging Spectroradiometer

NASA: National Aeronautics and Space Administration

NOAA: National Oceanic and Atmospheric Administration

PSAP: Particle Soot Absorption Photometer

RH: Relative Humidity

RR: Radiance Research

SAE: Scattering Ångström Exponent

SEUS: South Eastern United States

SGP: NOAA ESRL Aerosol site location index for Southern Great Plains Research site located in Lamont, OK.

SSA: Single-Scattering Albedo

THD: NOAA ESRL Aerosol site location index for Trinidad Head Research site located in Trinidad Head, CA.

TOA: Top Of Atmosphere (In particular reference to the top of the troposphere)

USCCSP: United States Climate Change Science Program

CHAPTER 1 - INTRODUCTION

1.1 Thesis Objectives

Work entailed in this thesis comprises investigations of the initial two years of aerosol optical property measurements made from the NOAA Earth Systems Research Laboratory (NOAA-ESRL) collaborative aerosol monitoring site at Appalachian State University (APP) combined with NASA satellite measurements made through the column of atmosphere over Boone, N.C (36.214^{o} N , 81.693^{o} W). The goal of the aerosol monitoring program at APP is to better understand how aerosols impact regional climate change and air quality, including seasonal and long-term variations in aerosol optical and microphysical properties and radiative effects, and the relative contributions of aerosol source regions and aerosol types to these effects.

The objectives of this thesis are as follows.

1. Illustrate the large seasonal variability in key aerosol optical properties and aerosol optical loading in the southeastern U.S. (SEUS). This will be accomplished through statistical comparisons of aerosol optical properties between APP and three other regionally representative NOAA-ESRL sites in the U.S.
2. Estimate the direct effect of aerosol on net solar radiation (termed Direct Radiative Effect-DRE).

3. Present initial aerosol hygroscopic growth measurements and explain how the data will be used in future studies to improve aerosol direct radiative effect calculations and aerosol source type classification.
4. Apply a hierarchical agglomerative cluster analysis using three key intrinsic aerosol optical properties to broadly classify the aerosol types with the largest influence on summer and winter as they provide the most contrasting radiative effects between seasons in the SEUS.

1.2 What Are Atmospheric Aerosols?

Aerosols are a suspension of fine solid or liquid particles in a gas (Seinfeld and Pandis, 2006) and are often observed as smoke, dust or haze. Aerodynamic particle diameters range from a few nanometers to tens of micrometers. Aerosols are generally classified as either primary or secondary. Primary aerosols are emitted directly into the atmosphere while secondary aerosols result from gas-to-particle conversion of precursor species. Both primary and secondary aerosols may result from a variety of natural or anthropogenic (e.g., human-influenced sources (Figure 1.1).

Natural aerosol sources include wind driven dust, sea salt, volcanic emissions, and plant emissions (biogenic). Primary anthropogenic aerosol generation occurs mostly from automobile emissions, industrial emissions, and biomass burning (which can also be a natural source). An example of secondary aerosols includes particles produced by the photooxidation of volatile organic gaseous precursors such as isoprene (Seinfeld and Pandis, 2006) which also play a dominate role in the seasonal variability of aerosol optical properties

in the SEUS. Concentrations of such volatile organic molecules including but not limited to isoprene in the SEUS are comparable to those in the Amazon (Portmann et al., 2009).

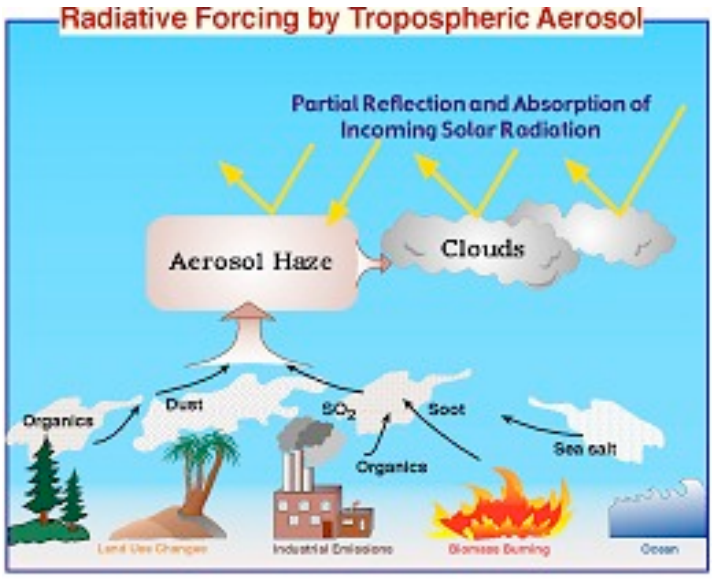

Figure 1.1. Cartoon of Radiative Forcing of Aerosols. Reprinted with Permission. (NOAA Pacific Marine Environmental Laboratory website)

1.3 How Do Aerosols Affect Regional Climate?

Aerosols directly affect solar radiation by scattering and absorbing some of the incident shortwave energy through a column of atmosphere. This direct interaction with solar energy has been termed the aerosol direct radiative effect (DRE-Charlson et al., 1992). Aerosols also serve as cloud condensation nuclei, thereby indirectly affecting the solar radiation budget by altering cloud reflectivity and lifetimes, in addition to precipitation potential (IPCC, 2007). Figure 1.2 illustrates both the direct and indirect radiative effects of atmospheric aerosols. The scope of this thesis will only deal with the direct effects of

aerosols in the troposphere.

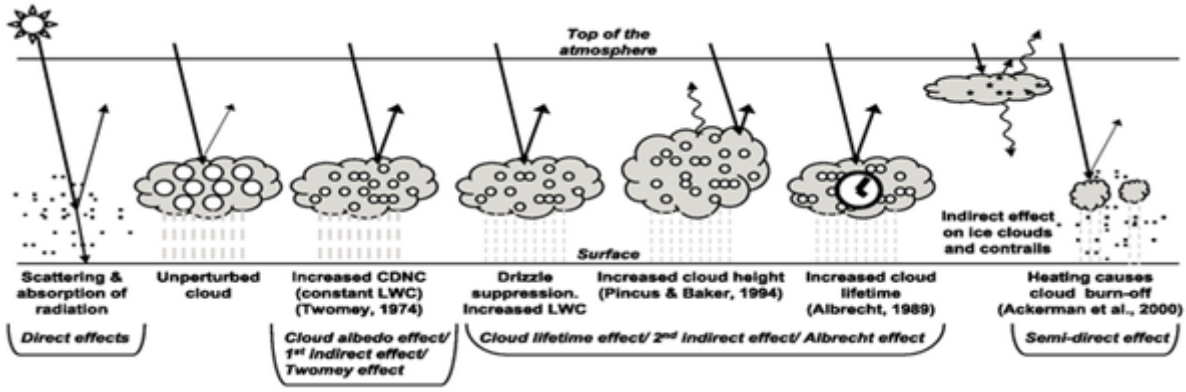

Figure 1.2. Diagram of TOA Radiative Effects. Reprinted with Permission. (Climate Change 2007. The Physical Science Basis. Working Group I Contribution to the Fourth Assessment Report of the Intergovernmental Panel on Climate Change, Chapter 2, Figure 2.10, (pg154).Cambridge University Press).

1.4 Need for Long Term In Situ Aerosol Monitoring in the SEUS

Aerosol direct and indirect radiative effects have been estimated to be of similar magnitude but opposite sign to greenhouse gas forcing in some regions of the world (Charlson et al., 1992; Kiehl and Briegleb, 1993). Perturbations to the Earth's climate due to greenhouse gases such as carbon dioxide (CO_2) and methane (CH_4) are well-understood; however, the IPCC has deemed the magnitude of the uncertainties surrounding aerosol radiative effects to be much greater than that of greenhouse gases (Figure 1.3).

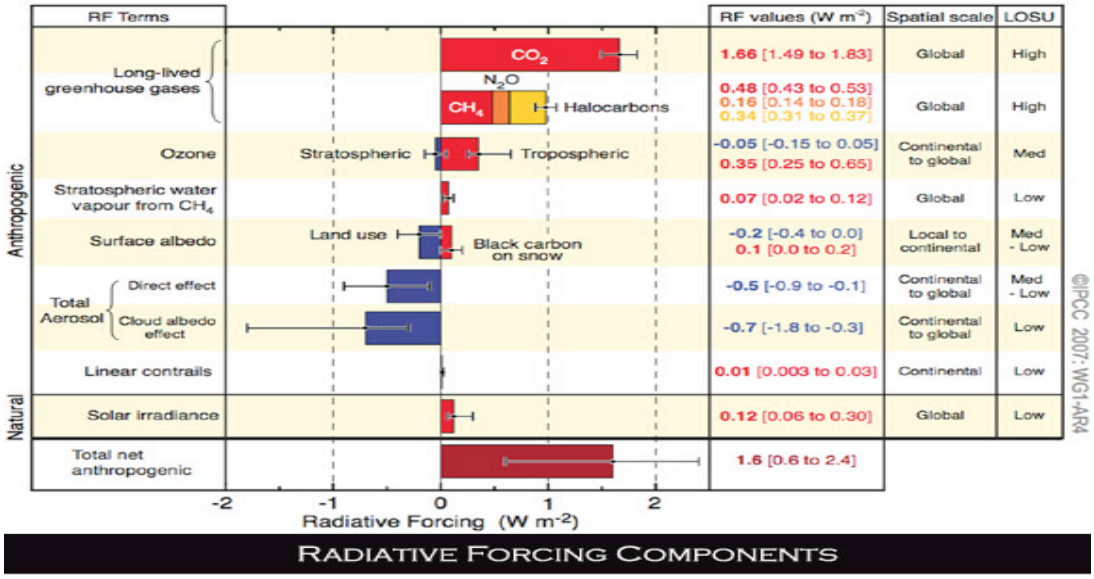

Figure 1.3. Global Mean Radiative Forcing (RF) Components (90% confidence intervals) Reprinted with Permission. (Climate Change 2007. The Physical Science Basis. Working Group I Contribution to the Fourth Assessment Report of the Intergovernmental Panel on Climate Change, Technical Summary, Figure TS.5, (pg32) Cambridge University Press).

As Global Climate Models (GCM) become more powerful the limitations in accuracies hope to be resolved through additional research in quantifying aerosol radiative effects. The IPCC recommends that additional research be done to better understand the optical and microphysical properties of aerosols, which should reduce these uncertainties in aerosol radiative effects.

The climatic perturbations due to aerosols as well as changes in air quality, and visibility are largely regional in nature. This results from the short atmosphere lifetimes (~3-10 days) of aerosols which are naturally removed by either wet (precipitation) or dry deposition (contact with surface) and inhomogeneous distribution of sources. This is in contrast to greenhouse

gases, many of which remain in the atmosphere for decades or longer and are thus well-mixed. This necessitates continuous aerosol measurements made from regionally representative locations.

While the interactions of aerosols on the solar shortwave budget and ultimately the climate can be complex, a simple indicator of those effects can be seen in changes in regional surface temperatures. Only a few locations globally have experienced a cooling trend during the last century (Portmann 2009)(Figure 1.4). One such region is the SEUS. Recent studies (Goldstein et al., 2009; Saxena et al., 1999) have shown that the effects of aerosols are consistent with a cooling effect in the SEUS during summer months.

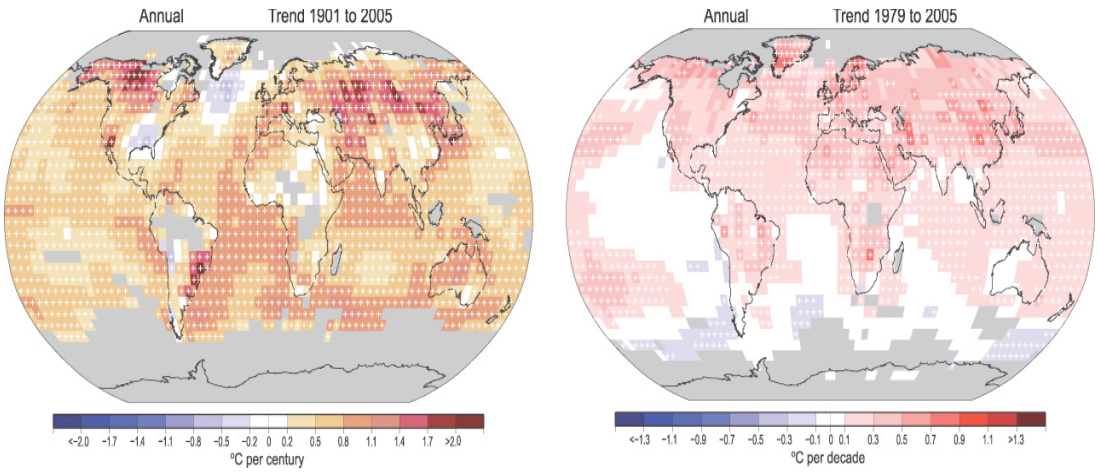

Figure 1.4. Average Surface Temperature Changes of °C per Century (LEFT) and °C per Decade (RIGHT). Reprinted with Permission. (Climate Change 2007. The Physical Science Basis. Working Group I Contribution to the Fourth Assessment Report of the Intergovernmental Panel on Climate Change, Technical Summary, Figure TS.6, (pg37) Cambridge University Press).

In addition to reducing the uncertainties of aerosol radiative effects, long term in situ ground based measurements provide a means for validating satellite measurements of key aerosol optical properties (Kahn et al., 2009). Recent studies show systematic errors in key aerosol optical properties when derived from satellite retrievals over particular regions (Levy et al., 2010). Understanding systematic relationships among aerosol optical properties should prove useful in reducing uncertainties in remotely sensed data by increasing confidence and better understanding the assumptions used in the data retrievals (Delene and Ogren, 2001).

1.5 Thesis Structure

- Chapter 2 provides detail on the experimental methods and techniques used by the NOAA-ESRL aerosol monitoring network, followed by an introduction to the data products used in this thesis.
- Chapter 3 details characterization efforts and the implementation of a humidograph system. This chapter also provides an explanation of my instrumentation contribution to the APP research group.
- Chapter 4 summarizes two years of aerosol optical property measurements and compares APP to three other established NOAA sites. APP illustrates a high seasonality and large aerosol optical loading measured in the summer months as compared to the other three sites. Preliminary direct radiative effect calculations will be presented as an approximation of the broadband (using 700nm as a proxy) values. Initial results of the humidograph system will be provided as frequency distributions of hygroscopic growth factors of the three most recent seasons as well as a few

periods of interesting anti-correlation between light scattering and hygroscopicity. Also, a hierarchical agglomerative cluster analysis for broadly classifying aerosol types will be provided.

- Chapter 5 provides some of the future plans for improving research which include implementation of a micro-pulse LIDAR, multiple chemistry instruments, and an improved humidograph system.
- Chapter 6 provides a summary of the work contained in this thesis and makes some suggestions for the future of aerosol research at APP.

CHAPTER 2- AEROSOL MEASUREMENTS AT APP-EXPERIMENTAL TECHNIQUES AND DATA PRODUCTS

This chapter is intended to provide an overview of the instrumentation and theory of operation needed to undertake long term aerosol radiative studies. A brief explanation of the experimental techniques associated with each measurement is presented, along with an explanation of the resulting data products. The reader is referred to more authoritative works (Delene and Ogren, 2001; Sheridan et al., 2001) for detailed treatments. In addition to the NOAA-supported in situ aerosol data products, remote sensing measurements of column-averaged aerosol optical loading, surface reflectance and cloud properties are needed in the simple box model used in this thesis work to calculate aerosol DRE. These data products are currently obtained from satellite-based measurements and will be briefly discussed as well. The chapter will end with a brief explanation of the magnitude and sources of each associated uncertainty for the respective aerosol optical properties. This analysis provides some context for claims made later in Chapter 4.

2.1 NOAA-ESRL Aerosol Monitoring Network

The NOAA Global Monitoring for Climate Change (GMCC) program began making baseline measurements roughly 40 years ago to aid in the understanding of the current and future impacts on the climate due to anthropogenic activities. Today the NOAA research group has expanded across the globe and is conducting measurements with almost 20 active

collaborative sites while continuing to maintain many of the original baseline sites (Figure 2.1). Each of these sites was selected based on a lack of local pollution sources and thereby possessing aerosol optical properties that are regionally representative. The semi-rural location of the APP site in the Appalachian Mountains is a regionally representative of the southeastern U.S. (Sherman et al., 2011)

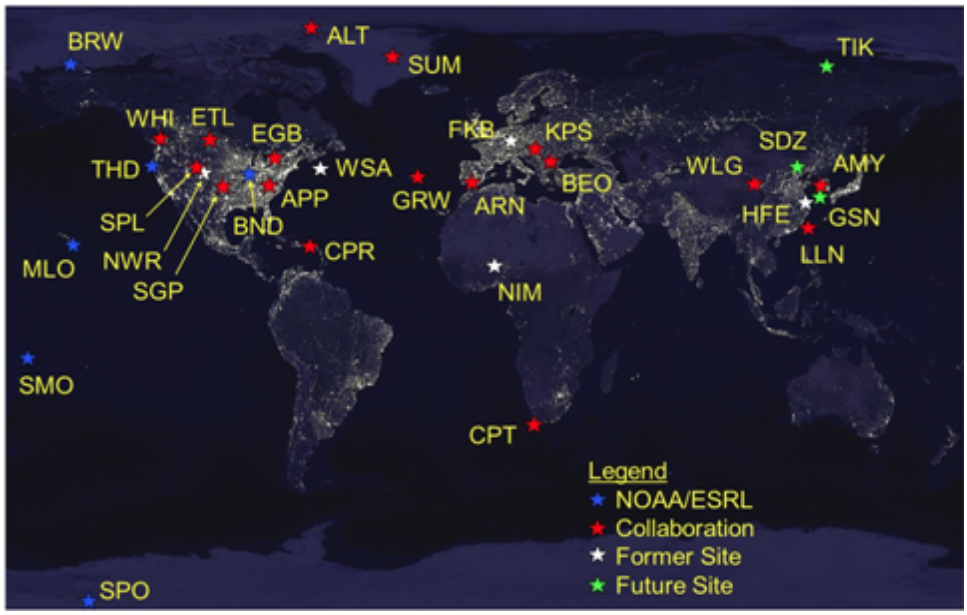

Figure 2.1. MAP of NOAA-ESRL Aerosol Monitoring Sites. Reprinted with Permission. (NOAA ESRL Aerosols Website)

In this thesis, aerosol optical properties measured at the Appalachian State University site (APP) will be placed in the context of those measured at the other three U.S. sites. (1) The Southern Great Plains (SGP) site in Lamont, OK; (2) Bondville, IL site (BDN) in rural central Illinois; and (3) Trinidad Head (THD) site in coastal Northern California. Geographical information and common aerosol types observed at each of the sites is provided in Table 2.1.

Table 2.1. NOAA-ESRL Aerosol-Monitoring Stations in U.S.

Site Location	**Boone, NC**	**Lamont, OK**	**Bondville, IL**	**Trinidad Head, CA**
Station ID	APP	SGP	BND	THD
Latitude	36.213° N	36.605° N	40.053° N	41.054° N
Longitude	81.692° W	97.485° W	88.372° W	124.151° W
Elevation (m)	1080	315	230	107
Geography Information	Small town in Southern Appalachian mountains	Rural, southern great plains	Rural location-25km from Univ. Illinois campus,	Northern California marine location
Common aerosol sources	Biomass burning, secondary organics resulting from interactions between tree emissions and pollutants, some power plant emissions	Agricultural emissions dust, oil refineries and power plants	Regional industrial emissions, corn and soy agricultural influences	Sea salts and other marine influences, occasional forest fires and inter-continental transport from East Asia

The four sites are each home to different aerosol types due to different source types and regions as well as seasonal variations. The comparison of aerosol optical properties measured at the four sites (Section 4.1) illustrates the common and unique features measured at the APP site. All sites maintain similar instrumentation and follow identical protocols to allow measurements to be directly comparable. In situ instrumentation at each site measure aerosol total light scattering, hemispheric back scattering, and light absorption coefficients at three visible wavelengths for two particle size cuts (sub 10μm particles and sub-1μm particles) as well as particle number concentration. Hourly averages of these variables are calculated and used to derive radiatively important intensive aerosol properties. All quality

assured data from the NOAA Aerosol monitoring sites is publicly available at the NOAA-ESRL website and at the World Data Center for Aerosols.

2.2 Aerosol Sampling Infrastructure for In Situ Measurements of Lower Atmospheric (Troposphere) Aerosol Properties

The APP site is located at the highest point on Appalachian State University campus and stands as the home for the Appalachian Atmospheric Interdisciplinary Research (AppalAIR) group. Sampling at higher elevations allows detection of regional baseline aerosols, a major focus of the ESRL and a reason for initiating research in the SEUS. However, this regional representativeness is contingent upon the site being unperturbed by local anthropogenic sources. Some evidence of this claim can be found in plots of diurnal absorption and scattering coefficients which are found in Appendix A.

The sampling inlet stack found at APP is 34 m tall (Figure 2.2) to avoid sampling the locally wind-blown ground-level aerosols and the adjacent tree emissions (Delene and Ogren, 2001). An inlet screen prevents insects, birds, and other material from being drawn into the system. Air flow entering the stack is drawn into the sampling tube at a rate of 150 lpm, which is subsequently divided by the sampling instruments. Sampled air is heated to maintain a relative humidity of ≤40% so as to isolate the aerosol optical properties from their humidity dependence. Following dehumidification, sampled air is split into two flow paths. A portion of the flow is routed to a Condensation Nucleus Counter (CNC) while the remainder is routed to the size segregation impactor box and then to the other instruments. A schematic of the system flow paths is seen in Figure 2.2.

Figure 2.2. Photo of 34 m Tall Inlet Stack at APP. Sampling building is in the lower left corner of the photo.

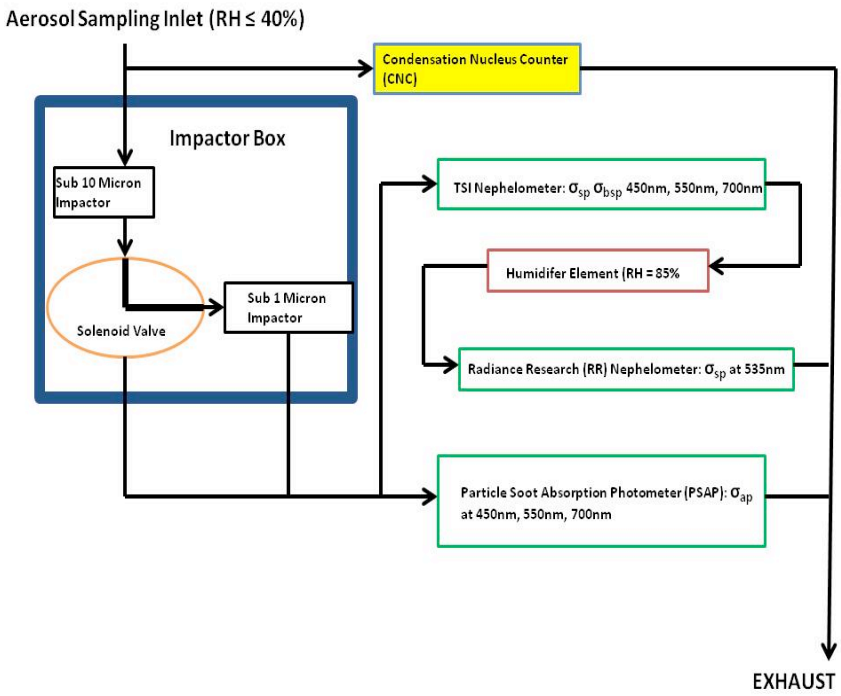

Figure 2.3. Simplified Flow Diagram for NOAA Aerosol Sampling System at APP site (Boone, NC). Sampled air inlet (1000 lpm at stack inlet then to 150 lpm at building inlet prior to impactor box) is displayed in the top left corner and exhaust is at the bottom left of the diagram.

Size-segregation is accomplished by an elutriation method of impacting particles with greater aerodynamic diameters than those being passed for measurement. A software controlled alternating solenoid selects the two pathways which allow either sub-10 μm or sub-1μm diameter particles to pass at six minute intervals. Following the impactor box, the air flow to be sampled passes on to the scattering and absorption-measuring instruments (Table 2.2) and is then exhausted into the atmosphere by pumps located outside of the building.

The entire sampling system is controlled using a NOAA developed Linux-based control/acquisition known as CPD2. CPD2 logs all raw data and forms 5-minute averages, which are further averaged over 1-hour and 24-hour periods for each of the two size cuts. The

data are transferred to the NOAA server every hour, where instrument-dependent corrections are applied. The archived data are accessed weekly by APP site personnel for editing and quality assurance. This quality assurance eliminates unrealistic values and spikes caused by instrument noise and local pollution plumes respectively. CPD2 reports all data as well as system status and instrument conditions back to NOAA ESRL scientists in Boulder, Colorado.

Table 2.2. Aerosol Optical and Microphysical Properties directly measured by NOAA instruments at APP site. All measurements at low humidity began in June 2009. Humidified nephelometer measurements began in September 2010.

Instrument	Measured quantities	Wavelength channels
TSI 3563 Nephelometer	Total aerosol light scattering and light backscattering coefficients	450 nm, 550 nm, 700 nm
Radiance Research (RR) Nephelometer	Total light scattering coefficients at an elevated RH (nominally at ~85% RH)	530 nm
TSI Particle Soot Absorption Photometer (PSAP)	Aerosol light absorption coefficients	467 nm, 530 nm, 660 nm
TSI Condensation Nucleus Counter (CNC)	Particle number concentration	N/A

2.3 NOAA Instrumentation

2.3.1 TSI Nephelometer

The TSI 3563 integrating nephelometer (Figure 2.4) measures the total aerosol light scattering and aerosol hemispheric back scattering coefficients at three visible wavelengths (450nm, 550nm, 700nm). All nephelometers employ the geometry designed by Beuttell and

Brewer (1949) with the TSI model 3563 being the industry standard following an extensive characterization (Anderson et al., 1996).

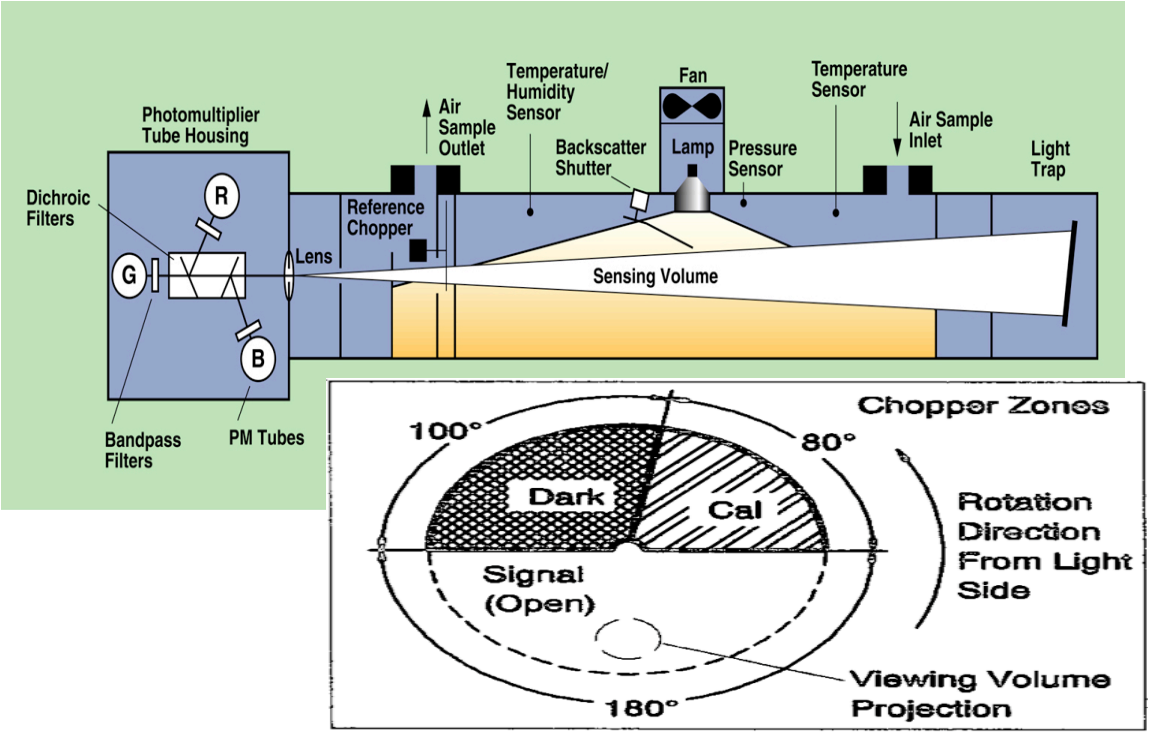

Figure 2.4. TSI Nephelometer and Reference Chopper Schematics. Displayed are the instrument geometry and working components. The backscatter shutter blocks all angles below 90 degrees allowing a measurement of light only scattered in the backwards hemisphere. The sub-image displays the reference chopper blade and the angles of rotation at which the instrument signal is used for the appropriate measurement.

The instrument employs what is now considered a standard scattering geometry which requires the receiving optics and electronics for the TSI are located on one end of the instrument while a light trap is fixed at the opposite end. A 75-watt quartz-halogen flash lamp is orthogonally to the sensing volume which it serves to provide illumination for. Flash lamp light immediately passes through an opal glass diffuser so as to obtain scattering angles from 7º– 170º for integration by the detector. The upper limit of 170º is due to a shadow plate. The hemispheric backscattering coefficient measurement integrates scattering angles

between 90º – 170º and is performed when a shutter moves into place so as to block the forward hemisphere scattering. Ideally, the scattering angles for total and hemispheric backscattering would be 0º – 180º and 90º – 180º, respectively. The angular truncations must be accounted for by using a size dependent truncation correction based on the Ångstrom exponent (Anderson and Ogren, 1998).

Light traveling towards the measuring optics must pass through a collimating lens before being separated with dichroic filters. Two dichroic filters separate the light into three separate beams of limited bandwidth that are then directed towards three photomultiplier tubes with spectral filters placed in front of them to allow peak transmission at 450 nm, 550 nm, and 700 nm respectively. Each spectral filter establishes a detection bandwidth of 50 nm for each measurement channel. The reference chopper (sub image of Figure 2.4) is used to either obstruct or pass the scattered light signal. Obstructing the signal allows dark and calibration measurements. The dark portion of the chopper blocks the signal to allow a measurement of the photo multiplier tubes (PMT) background signal. Calibration measurements allow some of the scattered light to pass the light to the PMTs allowing for a measurement of the flash lamp stability (Anderson et al., 1999). The nephelometer measurements of aerosol scattering coefficients must be calibrated bi-weekly using two gases with known scattering coefficients. This process is explained in more detail in Chapter 3. In addition to frequent calibrations, corrections factors are necessary due to limitations in the physical design of the instrument.

The first and most simple correction is accomplished by maintaining an average temperature and pressure. Light scattering measurements are sensitive to changes in temperature and pressure as those parameters directly affect the extinction coefficients. The more important corrections account for non-idealities stemming from angular truncation and the non-lambertian (slightly noncosine weighted distribution of light intensity) light source. These corrections are well characterized and make use of an empirical equation based on the spectral dependence of the extinction coefficient (Anderson and Ogren, 1998).

2.3.2 Radiance Research (RR) Nephelometer

Operated in series with the TSI nephelometer at the APP site, the Radiance Research (RR) nephelometer is employed as a crucial part of the humidograph system (Chapter 3) to study the humidity dependence of aerosol light scattering. The RR nephelometer (Figure 2.5) is operated at a higher relative humidity (85%) and is only capable of making a total light scattering measurement at 530nm due to the use of a single wavelength LED and the absence of a backscatter shutter. A correction to 550nm using the scattering Ångström exponent allows the calculation of a hygrocopic growth function (explained in Chapter 3). The RR nephelometer provides a less expensive alternative to adding an additional TSI unit.

The emitted beam passes through an opal glass diffuser to produce scattering angular coverage of 10º to 170º, which is 3 degrees less than the TSI range. An internal chopper paddle functions similar to the reference chopper in the TSI except there is not a calibration portion of the chopper. RR nepehelometer instrument calibration will be explained in Chapter 3. The paddle is made of a section of common circuit board material with a small

hole cut in the center. A small mirror with very low transmission is placed here to obstruct the beam, an improvement in stability over the previous piece of Mylar. The paddle alternates between the open and closed states so as to alternately measure the light scattering of the sampling volume or the PMT dark signal for subtraction respectively. When the mirror of the paddle obstructs the beam path, a small amount of signal is passed through allowing a dark measurement since the transmission of the mirror is very low and allows only a limited detectable signal it allows (when calibrated) a reference scattering measurement.

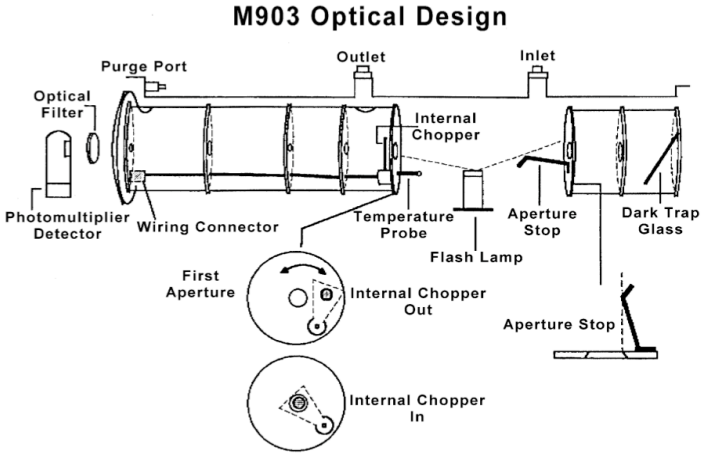

Figure 2.5. Schematic of the Radiance Research (RR) Nephelometer. The RR nephelometer at APP does not have a flash lamp but instead has an LED and a diffuser prior to the sampling volume. Integration occurs across 10^{o}-170^{o} over a single wavelength (530nm).

2.3.3 Radiance Research Particle Soot Absorption Photometer (PSAP)

The PSAP serves as the industry standard for determining atmospheric aerosol light absorption (Figure 2.6). The absorption measurement technique is based on transmission of

diffuse LED light by a quartz fiber filter at three visible wavelengths (467nm, 530nm, and 660nm).

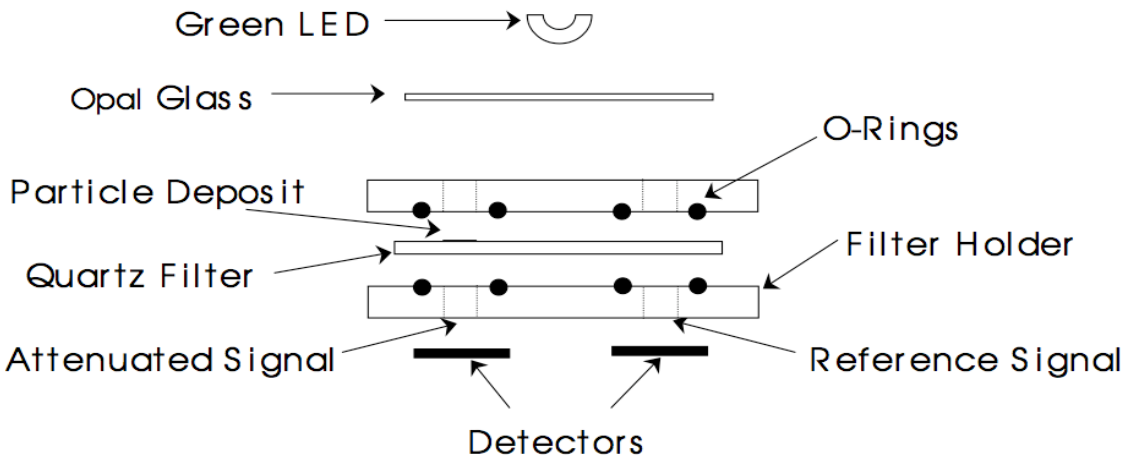

Figure 2.6. Schematic of the Particle Soot Absorption Photometer (PSAP). While not shown in this schematic, the PSAP has two filters. One that samples the deposited aerosols and a reference filter that provides an unloaded reference transmission measurement. The light is diffused by an opal glass diffuser and the instrument has three LEDs (467nm, 530nm, and 660nm). (NOAA-ESRL Website)

Detectors below the filters measure the transmitted beam intensity(I_t), which is then related to the measure of the uncorrected aerosol absorption coefficient σ_{apb^*} using 2.1.

$$\sigma_{apb^*} = \frac{A}{V} \ln\left(\frac{I_t - 1}{I_t}\right) \tag{2.1}$$

I_t is the average intensity of transmitted light during a given time step, A refers to the filter spot size surface area, and V is the volumetric air flow rate passing through the filter. Due to the scattering of light caused by embedded particles on the filter and the variation in filter sample spot size area caused by poor o-ring seating corrections are needed. These corrections, have been well characterized by Bond et al., (1999) and the corrections for unwanted scattering from embedded particles is represented below in 2.2 (Cappa et al., 2008).

$$\sigma_{ap,psap} = 0.873\left[\frac{\sigma_{apb^*}}{1.0796 \cdot T_r + 0.71}\right] \times \frac{1}{1.22} \quad (2.2)$$

A final corrected equation (2.3) was developed for the PSAP measured absorption coefficientσ_{ap}. This correction accounts for spot size area deviation, flow rate variations and signal attenuation due to aerosol light scattering by the embedded particles (Cappa et al., 2008).

$$\sigma_{ap} = \sigma_{ap,psap} - 0.016 \times \sigma_{sp,psap} \quad (2.3)$$

The total contribution of light scattering due to embedded particles $\sigma_{sp,psap}$ was determined empirically as $\sigma_{sp,psap} = \sigma_{ext} - \sigma_{ap,psap}$ and described in detail by Smith and Atkinson (2001); Patterson et al., (2004); Baynard et al., (2007) using Cavity Ring-Down (CRD) spectroscopy techniques.

A CPD2 quality assurance algorithm flags all data when the PSAP transmission drops below 0.75 or 75% and discards all data with transmission values of ≤ 0.5 or 50%, as the uncertainty due to scattering increases dramatically (Cappa et al., 2008).

Several of the intensive aerosol optical properties discussed below utilize both the measured scattering and absorption coefficients and thus necessitate values of each at common wavelengths. To this end PSAP-measured aerosol coefficients are scaled to 450 nm, 550 nm, 700 nm using a power-law relationship between aerosol absorption and the spectral dependence (absorption Ångström exponent (AAE)) of that coefficient (Lewis et al., 2008) for varying wavelengths is shown in 2.4.

$$\sigma_{ap_{700nm}} = \sigma_{ap_{660nm}} * \left(\frac{660nm}{700nm}\right)^{AAE} \quad (2.4)$$

2.3.4 TSI Condensation Nucleus Counter (CNC)

The CNC (Figure 2.7) employs laser light scattered by sampled particles to count the particles. Knowledge of particle counts and flow rate are used to calculate aerosol number density. Sampled air passes through a heated butanol saturation chamber followed by a condensing chamber where the alcohol vapor condenses on to the particles. This condensation allows the particles to grow in size, thereby enhancing countability.

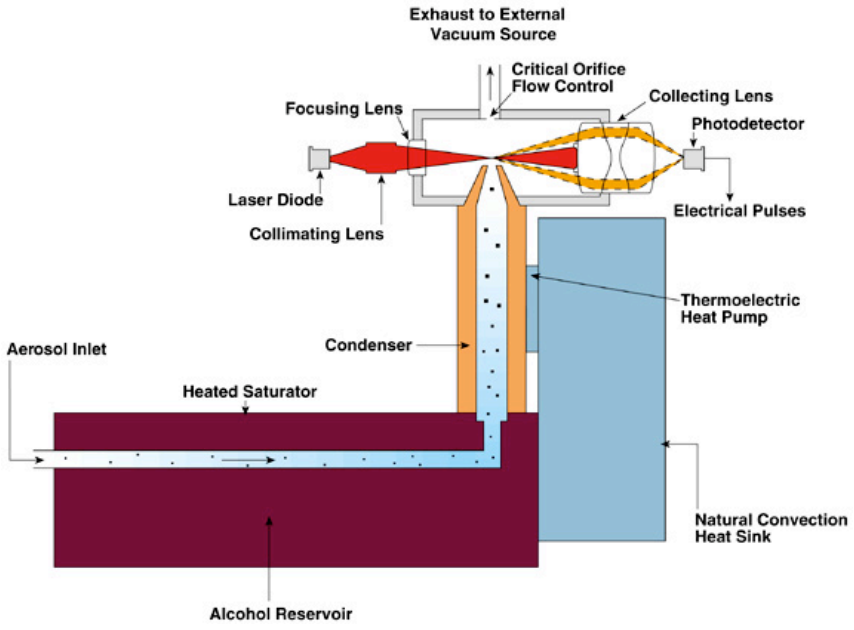

Figure 2.7. Schematic of TSI Condensation Nucleus Counter (CNC). Particles are represented by black dots moving from left (inlet) to right in the alcohol reservoir (saturation chamber).

2.4 Derived Aerosol Optical Properties

The aerosol total light scattering, hemispheric backscattering, and absorption measurements at three wavelengths are used to derive the following intrinsic aerosol optical properties for both the sub-1 μm and sub-10 μm size cuts.

2.4.1 Single-Scattering Albedo (SSA)

SSA provides a measure of how "white" or reflective an aerosol is. SSA is defined as the ratio of the total aerosol light scattering coefficient to total aerosol light extinction coefficient (the sum of absorption plus scattering) at a particular wavelength as shown in 2.5.

$$\text{SSA} = \frac{\sigma_{sp}}{\sigma_{sp}+\sigma_{ap}} \tag{2.5}$$

Purely scattering aerosols such as sulfates possess near-unity SSA values while black carbon possess very low SSA approximately ~0.16 (dependent on mixing) for visible wavelengths (Haywood and Shine, 1995).

2.4.2 Hemispheric Backscatter Fraction (b)

Hemispheric backscatter fraction (b) is the ratio of the back scatter coefficient to the total scattering coefficient measured by the TSI nephelometer as shown in 2.6.

$$b = \frac{\sigma_{bsp}}{\sigma_{sp}} \tag{2.6}$$

It thus represents the fraction of the scattered light into the backward hemisphere by the particles, referenced to the direction of the illuminating light beam. b provides qualitative information on particle size and is also used as an input for the empirical formula defined by Wiscombe and Grams (1976) for calculating upscatter fraction (Section 2.4.5), a parameter used in the box model approach for calculating direct radiative effect (Section 4.3) (Koontz and Ogren, 2003).

The magnitude of b values provides qualitative information on particle size through manipulation of the aerosol light scattering phase function. Mie theory (Bohren and Huffman, 1983) predicts that aerosol particles with diameters on the order of the illuminating

wavelength and larger will scatter light primarily along the forward direction yielding small b values which produces a less symmetric scattering phase function. In contrast, particles much smaller than the illuminating wavelength will scatter light symmetrically in all directions (b values approaching 0.50).

2.4.3 Upscatter fraction (β)

β is used to calculate aerosol radiative forcing efficiency and direct radiative effects and represents the fraction of incident solar light scattered in the upward hemisphere. It is the same as hemispheric backscatter when the sun or light source is directly overhead. The upscatter fraction is necessary for estimating the amount of solar radiation scattered back into space by aerosols since the sun is rarely level with the horizon. Hemispheric backscatter fraction b serves as an input parameter for the empirically approximated equation for upscatter fraction (Wiscombe and Grams, 1976) as illustrated with 2.7.

$$\beta = 0.0817 + 1.8495b - 2.9682b^2 \tag{2.7}$$

The distinction between "upwards" and "backwards" is important since the top of the atmosphere (TOA) solar irradiance that is scattered into the upper hemisphere constitutes an upward radiation flux, thereby reducing the energy available to heat the Earth-atmosphere system.

2.4.4 Absorption Ångström Exponent (AAE) and Scattering Ångström Exponent (SAE)

The absorption Ångström exponent (AAE) describes the wavelength dependence of the aerosol absorption coefficient as shown in 2.8.

$$AAE = \frac{-log\left(\frac{\sigma_{ap\lambda_1}}{\sigma_{ap\lambda_2}}\right)}{\log\left(\frac{\lambda_1}{\lambda_2}\right)} \tag{2.8}$$

One application of the AAE is to scale absorption to wavelengths other than those measured. It is used to scale other intensive aerosol properties to equivalent wavelengths and can be used to broadly classify aerosol types when combined with SSA and b data. Wavelength dependence of aerosol light absorption can be used to help distinguish between some aerosol types (organic carbon, black carbon or dust) and can be used along with other aerosol optical properties (SSA and b) to broadly classify aerosol types (see Section 4.5). For example, AAE values above 1.0 are consistent with increased organic carbon (OC) concentrations (Schnaiter et al., 2006) and Angstrom exponent values near 1.0 would indicate black carbon (BC) (Russell et al., 2007). However, direct comparison of AAE values should only be carried out if the measurements are at equal wavelengths. Therefore, for this thesis, it will simply be stated that the higher the values relative to one another provides a fair indication into the relative amount of organic material sampled at the sites. The broad classification of dust and sulfates would be difficult since the visible light absorption is fairly low for dust and sulfates possess next to zero visible light absorption.

It should be noted that there are some limitations associated with the Ångström exponent. Ideally measurements of aerosol light absorption would be available over a large spectral range. A linear fit of the logarithm of spectral light absorption is then used to deduce AAE (via the slope). In practice, absorption at two wavelengths is often employed to generate a coefficient believed to represent the spectral range used. Furthermore, the slope varies with wavelength and so the value calculate over a limited spectral range may not necessarily be used to extrapolate the spectral dependence of aerosol light absorption over a larger

wavelength range. Regardless, relative values of AAE can be used along with other aerosol optical properties to obtain information regarding aerosol type, as discussed in Section 4.5.

Scattering Ångström exponent (SAE) represents the wavelength dependence of the scattering coefficient as shown in 2.9.

$$SAE = \frac{-log\left(\frac{\sigma_{sp\lambda_1}}{\sigma_{sp\lambda_2}}\right)}{\log\left(\frac{\lambda_1}{\lambda_2}\right)} \tag{2.9}$$

SAE provides qualitative information of the relation of mean particle sizes (Pereira et al., 2011). SAE values approaching 4 represent air molecules which would be a situation of particles being much smaller than the wavelength of the illuminating light source. SAE values near zero represent particles much larger than the wavelength (e.g., rain droplets).

2.5 Relevant Remotely-Sensed Data Products

In addition to SSA and b, the box model calculation of aerosol DRE (Haywood and Shine, 1995) (to be explained later in this section) also requires knowledge of variables obtained only through remote sensing techniques. These include aerosol optical depth (AOD), cloud fraction A_c, and surface albedo R_s.

All remotely sensed variables used in this thesis were obtained via the NASA Moderate Resolution Imaging Spectroradiometer (MODIS) instrument, located aboard the NASA Aqua and Terra earth-orbiting satellites. MODIS platforms (Aqua and Terra) utilize 36 spectral bands across the visible and infra red range. The measurement provides a swath width of 2300 km at 705 km of elevation and possesses an absolute irradiance accuracy of 5% when measuring at wavelengths below 3 μm (Levy et al., 2007). The DRE calculations performed

for this thesis used daily averages of AOD and cloud fraction and monthly averages of surface reflectance.

MODIS uses a well documented algorithm that operates on matching observed spectral reflectance statistics of non-cloudy pixels to lookup tables (LUT) that simulate spectral reflectance for expected aerosols conditions (Levy et al., 2010). MODIS has a coarser temporal resolution than may be desired when compared to in house ground-based remote sensing techniques such as that employed by the NASA Aerosol Robotic Network (AERONET-Holben, 1998) of solar-tracking radiometers.

2.5.1 Aerosol Optical Depth (AOD) and Cloud Fraction

AOD is the vertical column integral of the aerosol extinction coefficient (Koloutsou-Vakakis et al., 2001) represented in 2.10. AOD is used as a proxy for atmospheric loading as it is related but not directly proportional to the number concentration of particles attenuating solar radiation.

$$AOD = \int_{z_o}^{z_f} (\sigma_{bap}(z) + \sigma_{bsp}(z.RH_{reference}) f(RH)_{sp}) dz \quad (2.10)$$

AOD measurements are only possible when the line-of-sight between the instrument and sun is cloud-free. The use of satellite-based AOD measurements in the thesis necessitates the use of daily-average values. AOD values typically range 0.05 for near pristine conditions to 1.0 for areas near the source of large particulate emissions such as smoke plumes (Seinfeld and Pandis., 2006).

Cloud fraction, A_c is the fraction of the visible sky containing clouds. It is used under the box model assumption that aerosol direct radiative effects are only observed below cloudless sky.

2.6 Geophysical Variables Used In DRE and Radiative Forcing Efficiency Calculations

2.6.1 Solar Constant (S_o), Daylight Fraction (D), and Surface Reflectance (R_s)

S_o is defined as the amount of incident solar irradiance at the TOA, equal to 1370 W/m^2. Daylight fraction is the fraction of a 24 hour day that is illuminated with solar radiation. This variable was determined by assuming a monthly average based on the fraction of daylight on the 15th day of each month using the Navy Astronomical Solar altitude/azimuth lookup table. Numerical values of surface albedo and daylight fraction for each month are provided in Table 2.3.

Surface albedo, R_s is a measure of the reflectivity of the area of the earth being studied. For the DRE calculations (Section 4.3), monthly averaged single band values of R_s were used since the terrain and environment does not experience significantly day-to-day variability in surface reflectivity. R_s was retrieved based on a 3km x 3km grid centered at APP which determined the spatial resolution of the DRE calculations.

Surface albedo values due change substantially during the months of summer, which is to be expected due to increased foliage of the surrounding forest causing increased scattering of incident light penetrating the forest canopy. The winter months (DJF) have higher reflectivity due to the reduced foliage and snowfall which from the data, snow appears to

remain on the surface most often during February. Daylight fractions are also largest during summer months which will affect the amount of radiative effects. Without sunlight there can be no radiative effect. With 20% longer days in June and July as compared to December, it stands to reason that day length may alter effect values greatly.

Table 2.3. Monthly Geophysical Variables Used in DRE calculations. Numbers in parenthesis are used in certain plots as they represent the corresponding month.

Geophysical Parameters in DRE Calculations		
Month	**D**	**R_s (700nm)**
January (1)	0.41	0.11
February (2)	0.45	0.29
March (3)	0.50	0.10
April (4)	0.54	0.06
May (5)	0.59	0.11
June (6)	0.61	0.06
July (7)	0.60	0.04
August (8)	0.56	0.03
September (9)	0.52	0.04
October (10)	0.47	0.04
November (11)	0.45	0.05
December (12)	0.40	0.14

2.6.2 Atmospheric Transmission (T_{atm})

Atmospheric transmission T_{atm} represents the optical transmission of the atmosphere for a given wavelength from the TOA to the top of the aerosol layer (typically 3-4 km). It accounts for Rayleigh scattering of light by clean-air molecules and absorption by ozone and nitrogen dioxide. Values used in the DRE calculations were determined based on seasonally-averaged values.

2.7 Radiative Forcing Efficiency and Effect

2.7.1 Aerosol Radiative Forcing Efficiency

Aerosol radiative forcing efficiency, 2.12, as defined by Sheridan and Ogren (1999) is the direct aerosol radiative forcing normalized per Aerosol Optical Depth (AOD), making the calculation independent of aerosol optical loading (Delene and Ogren, 2001).

$$\frac{\mathrm{DRE}}{AOD} = -DS_o T_{atm}^2 (1 - A_c) SSA\beta \left[(1 - R_s) - \left(\left(\frac{2R_s}{\beta} \right) \left(\frac{1}{SSA} - 1 \right) \right) \right] \qquad (2.12)$$

The calculation facilitates comparison of the radiative effects of intrinsic properties measured at different sites by normalizing to AOD and using globally average values for geophysical variables. All necessary input variables for radiative forcing efficiency have been covered to this point and are listed in Table 2.3. The only aerosol optical properties acquired are SSA and b. Larger values of direct forcing efficiency imply a greater ability for aerosol types to modify the solar flux at the TOA. The sign convention is that a negative (positive) value implies a cooling (warming) effect at the TOA.

Table 2.4. All Variables with Units Used in DRE Calculations.

Variable Symbol	Variable Name	Units
DRE	Direct Radiative Effect	W/m^2
AOD	Aerosol Optical Depth	None
D	Daylight Fractional	None
S_o	Solar Constant	W/m^2
T_{atm}	Atmospheric Transmission	None
A_c	Cloud Fraction	None
SSA	Single-Scattering Albedo	None
B	Upscatter Fraction	None
R_s	Surface Reflectance (Albedo)	None

2.7.2 Direct Radiative Effect (DRE)

Direct Radiative Effect (DRE) as shown in 2.13, is the term used to describe the perturbation of climate through the scattering and absorption of solar radiation by aerosols (Charlson et al., 1992; Kiehl and Briegleb, 1993) and provides an indicator of the potential magnitude aerosols will have towards affecting climate (Haywood and Shine, 1995).

$$DRE = -DS_o T_{atm}^2 (1 - A_c) SSA\beta AOD \left[(1 - R_s) - \left(\left(\frac{2R_s}{\beta} \right) \left(\frac{1}{SSA} - 1 \right) \right) \right] \qquad (2.13)$$

Radiative effect calculations have units of W/m^2. Simplistically speaking, DRE can be described as a change in planetary albedo due to the presence of aerosols scattering and absorbing radiation. An image of this simple view is provided in Figure 2.8.

The aerosol variables used in the box model typically represent spectrally-averaged values over the shortwave solar spectrum. However, studies (Haywood and Shine, 1995) have determined that the aerosol optical properties at 700nm may be used as a reasonable estimate for the spectrally-averaged optical properties. NOAA measured SSA and calculated

upscatter fractions are both known at 700nm. MODIS-measured surface albedo is also provided very near to 700nm (within bandwidth resolution). AOD is measured by MODIS at 550nm, but this can be extrapolated to 700nm using an assumed Ångström exponent.

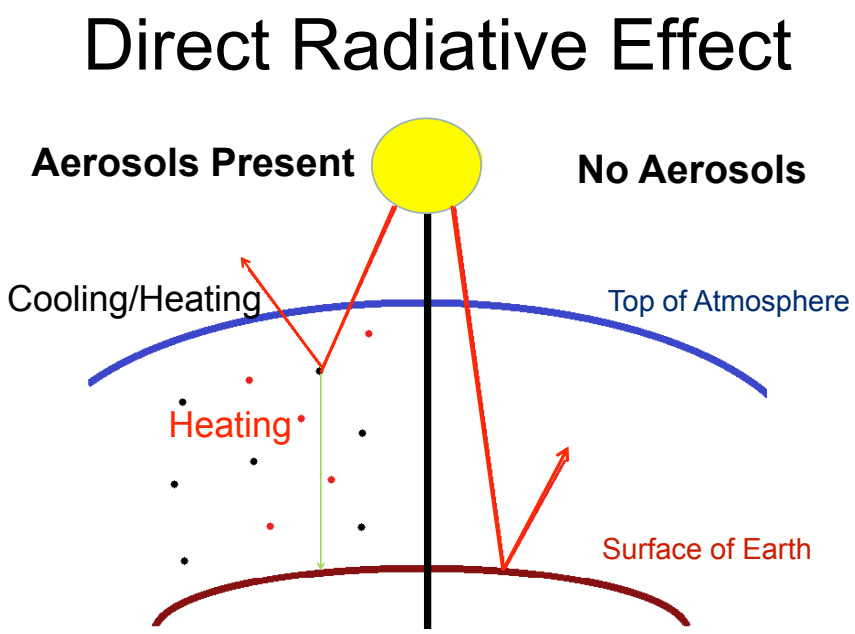

Figure 2.8. Illustration of TOA DRE theory.

2.8 Measurement Uncertainty Investigation

Accepted uncertainty of the TSI and PSAP are 15% and roughly 25% respectively (Cappa et al., 2008; Taubman et al., 2004a). The TSI uncertainty results from a 10% instrument uncertainty due primarily to an angular truncation (integrating over only 163º) and a non-Lambertian light source (Anderson et al., 1996). The PSAP has similar issues. Uncertainty arises from another non-Lambertian light source, the quartz fiber filter sample spot size, which deviates due to instrument sampling chamber seals, and the fact that particles become embedded on the filter. Since most particles are not purely absorbing, some of the attenuated signal read by the photodiodes is due to light scattering and not absorption (Bond et al.,

1999). Uncertainties for SSA and hemispheric backscatter fraction had to be propagated following the method found in Taubman et al., (2004).

Table 2.5. Several Intrinsic Aerosol Optical Properties with Uncertainties.

Variable Name	Symbol	Units	Uncertainty (δ_q)	Source/s of error	Information source and notes
Scattering Coefficient	σ_{sp}	Mm^{-1}	15%	(10%) Instrumental (11%) Sensitivity	Anderson 1996 and Taubman et al., 2004 Error source values were added in quadrature.
Absorption Coefficient	σ_{ap}	Mm^{-1}	20-30%	Combination of Instrument error and measurement uncertainty	Cappa et al., 2008 Bond et al., 1999
Single-Scattering Albedo	SSA	None	2-3%	Error associated with scattering coefficients	Calculated from above uncertainties and propagated using methods in Taubman et al., 2004
Hemispheric Backscatter Fraction	b	None	15%	Same error associated with scattering coefficients	Calculated from above uncertainties and propagated using methods in Taubman et al.,, 2004

Uncertainties can be added in quadrature since the uncertainty in measured light scattering is independent of the uncertainty in measured light absorption. The coefficients are calculated from different instruments and different methods. The mean value of SSA values for all time at APP is 0.89 $\pm$ 0.02 with the uncertainty being calculated based on equation 2.14.

$$\frac{|\Delta\omega_o|}{\omega_o} = (1-\omega_o)\left(\frac{\Delta\sigma_{sp}}{\sigma_{sp}}\right)^2 + \left(\frac{\Delta\sigma_{ap}}{\sigma_{ap}}\right)^{2^{1/2}} \quad (2.14)$$

CHAPTER 3-IMPLEMENTATION OF A HUMIDOGRAPH

A humidograph is a controlled relative humidity (RH) nephelometry system used to determine the dependence of light scattering and light back scattering coefficients (Carrico et al., 1998) on relative humidity (RH). This chapter discusses the rationale, design, and characterization of the humidograph operating at the APP site. Instrument maintenance as well as characterization and optimization of the humidograph represent my instrumentation contribution to the research group.

3.1 Measuring the Dependence of Aerosol Light Scattering on Relative Humidity

Due to the fact that the size and refractive index of aerosol particles are modified by water uptake, the magnitude and angular dependence of light scattered by aerosols depend upon ambient relative humidity (Jeong et al., 2007). One of the limiting factors influencing the accuracy of DRE calculations is the misrepresentation of the variability of relative humidity (RH) on the aerosol light scattering coefficients (Carrico et al., 1998) which ultimately modify the values of SSA and upscatter fraction used in the calculation. Aerosol light absorption is also affected by RH, but to a much smaller degree than light scattering (Jeong et al., 2007) and this effect is considered in this thesis. The aerosol optical properties measured at NOAA-ESRL sites are measured at a low reference RH of 40% or less (discussed in Chapter 2), so as to isolate the properties from their humidity dependence. Knowledge of the aerosol optical properties at a low reference RH, combined with a known

(or assumed) functional dependence of light scattering on RH, is typically used to scale aerosol light scattering and the derived intensive optical properties of SSA and upscatter fraction (β) to ambient RH for DRE calculations.

This function is commonly termed the aerosol hygroscopic growth factor f(RH), although actually referring to the dependence of light scattering on RH and not the dependence on enhanced particle size. The problems associated with this functional dependence are (1) it is different for various aerosol types (through varying hygroscopicity) measured at a given location; and (2) there are very few experimentally-derived functions with those that do exist being often based on short-term field campaigns in well dispersed parts of the world. As such, the assumed function used may or may not accurately represent the aerosol types actually being measured.

3.2 Hygroscopic Growth Factor f(RH)

While the light scattering dependence on RH is non-linear for most aerosol types, a simple 2-point curve can be used as a linear approximation, a condition that is much easier to implement experimentally (Kim et al., 2006). The curve is generated by via simultaneous measurements of light scattering made at low and elevated reference RH values, from which a ratio is taken. This ratio of scattering coefficients represents the aerosol hygroscopic growth factor as defined in 3.2.

$$f(RH) = \frac{\sigma_{sp(\sim 85\% RH)}}{\sigma_{sp(40\% RH)}} \tag{3.2}$$

While the lower limit of condensation occurs around 85% RH, most aerosol particles deliquesce prior to 85% RH, allowing the safe and more reliable operation of the humidograph at ~85% RH. As long as the low RH value remains at or below 40%, there is a negligible effect on the ratio as most aerosols have very low water uptake below 40% RH.

Following complete characterization, the humidified light scattering measurements from the RR nephelometer will be used to scale dried aerosol optical properties to ambient RH, leading to improved DRE calculations. In addition, these data will also be used to help identify various aerosol types by providing another parameter/dimension used in the aerosol-types cluster analysis.

3.3 Humidograph Design

The humidograph was designed and constructed at NOAA-ESRL and implemented at APP during September 2010. A Radiance Research nephelometer was placed down-stream of the existing TSI nephelometer separated by a humidifier element (Figure 3.1).

The RR nephelometer operates at a fixed RH of 85% while the TSI operates at low RH (<40%). As particles pass from the TSI to the RR, they are forced through the humidifier element. The humidifier element is an annular concentric tube (~35cm long and ~2cm in diameter) in which water is heated by a controlled heater tube while being passed through a Teflon membrane allowing saturation of sampled aerosol particles (Koloutsu-Vakakis et al., 1996). Water is provided and stored in a reservoir located on top of the instrument. Distilled water is used to limit the amount of impurities that may enter the humidifier diminishing the

lifetime of the element. Heater tube temperature is controlled by a Proportional-Integral-Derivative (PID) controller that produces a variable output voltage that heats a section of electrical resistance tape (Koloutsu-Vakakis et al., 1996). Constant air flow is achieved using a mass flow controller which also serves to minimize particle losses, as discussed in section 3.4.2.

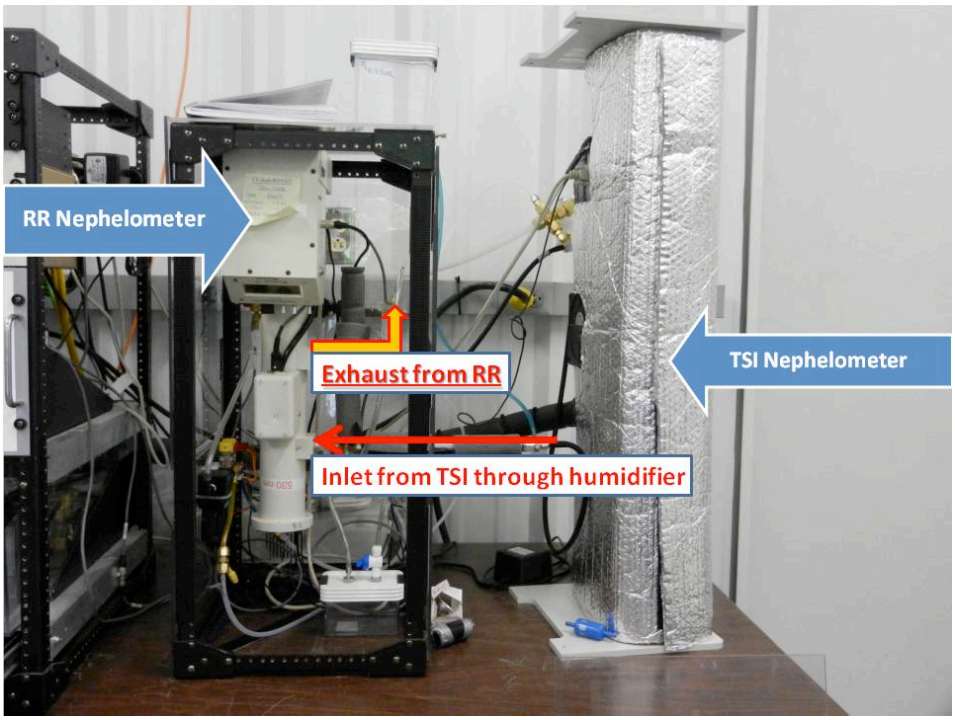

Figure 3.1. Picture of APP Nephelometry System Under Normal Operating Conditions. The TSI unit is wrapped with an insulating material to aid in limiting variations in the instrument temperature. Sampled air passes through the TSI nephelometer and is picked off (black tube leading to red inlet arrow) at the exhaust side of the TSI. After humidification (humidifier element is partially hidden by solid red arrow) the RR nephelometer samples the aerosols and performs the humidified aerosol light scattering measurements.

The RR nephelometer is operated in an inverted position which serves to prevent possible damage to the instrument electronics in the event of the instrument being flooded by water.

Flooding occurs on occasion following the rupture of the humidifier membrane. CPD2 software-activated, solenoid-actuated valves control air flow to the instrument. This is an important feature for calibrating the instrument which is to be explained later in this chapter.

3.4 Humidograph Characterization and Modifications

My contributions to the humidograph implementation include the following.

- Maintaining and troubleshooting the system.
- Development and implementing of a site specific humidograph calibration protocol while under the guidance of NOAA ESRL scientists.
- Replacing the calibrator optics with optics possessing more stable transmission characteristics.
- Instrument characterization, which includes (a) calibrating the instrument (b), quantifying the inlet particle loss correction factor, and (c) aiding in the calculation of the appropriate RR nephelometer angular truncation correction factor. Both correction factors are averaged and applied to all APP humidified light scattering data. These characterizations represent, to the best of our knowledge, the first characterization attempts conducted on the RR nephelometer at an elevated RH.

3.4.1 Calibration Routine

Humidograph measurement errors resulting from nephelometer calibration drift necessitate regular (approximately weekly) calibrations particularly when using the temperamental RR nephelometer. The employed calibration method is based on that described by Anderson et

al., (1996) and Anderson and Ogren, (1998). Calibrations employ two gases (typically filtered air and carbon dioxide) with well-known light scattering coefficients, from which an internal algorithm forms a 2-point linear interpolation fit. Filtered air is provided by a HEPA filter and passes through the nephelometer when the solenoid valves remain in the normal operation setting. By definition, filtered air should produce an aerosol light scattering coefficient of roughly 0 Mm^{-1}. To sample carbon dioxide, the solenoid-actuated valve switched to the opposite setting so that the system vacuum to allow the flow of carbon dioxide through the instrument in an opposite flow direction in which it passed through the RR nephelometer first. Each calibration gas would be sampled and offsets would be corrected using the RR nephelometer adjustment toggle switches. Since stable scattering coefficient values of the known gases were needed to judge instrument performance, the slight changes in temperature and pressure caused fluctuations in the scattering coefficients of carbon dioxide causing that portion of the calibration to be more tedious. Following successful filtered air (zero) and carbon dioxide (span) calibrations an automated system calibration designed by NOAA and controlled by CPD2 would be administered. This weekly routine provides a standard metric with predetermined instrument flush and sample times to calculate the scattering coefficients for both nephelometers and report a percent error from the expected scattering coefficients of filtered air and carbon dioxide. System zero/span checks resulting in percentage errors larger than $\pm$7% indicate that the user must repeat the calibration routine from the beginning. All errors were recorded via an online log entry in CPD2 while all instrument adjustments were recorded in a site log book. Records allow the users to monitor instrument drift and performance over long time periods (Anderson and Ogren, 1998). More detail on this procedure can be found in Appendix 3.

3.4.2 Particle Loss Correction

It is impossible for all particles entering an instrument to reach the sampling volume let alone make it to an additional downstream sampling chamber of a second instrument. Slight differences in the nephelometer geometries and slight deviations in instrument flow rates result in some particle loss. Various aerodynamic diameter particles become embedded in or around the inlets and walls of the instrument. As particle diameters increase, the momentum of the particles and the likelihood of them not being sampled increases as well which indicates a loss of instrument efficiency when sampling predominantly larger particles. Particle losses through the RR nephelometer are measured following the weekly instrument calibrations by comparing scattering coefficients of the two instruments while at equal humidity levels. During a 30-60 minute time frame, multiple measurements of scattering coefficients are used to compute and average particle loss. By taking the ratio of the RR nephelometer to the TSI nephelometer scattering coefficients, a particle loss factor is calculated and reported in an online log entry. This ratio typically lies between 0.92-0.98, indicating that between 2-8% of particles are being lost between the TSI sampling chamber and the RR sampling chamber. This is consistent with previous studies of reported particle losses of close to 5% through the RR nephelometer (Sheridan et al., 2001).

3.4.3 Radiance Research Nephelometer Correction Factor for Humidified Conditions

Substantial work has been undertaken to better quantify the correction factors that must be multiplied to the TSI 3563 nephelometer measurements of aerosol light scattering,

accounting for non-idealities of the instrument design (Anderson 1996, Anderson and Ogren 1998). The RR nephelometer has not been as well characterized especially while operating at a humidified state. A correction factor was needed to correct for the non-idealities of the instrument as well as correcting for the error that would occur from making a humidified measurement.

Using the Ångström exponent based correction method found in Koloutsu-Vakakis et al., (1996) in combination with the angular truncation correction factor for humidified air found in Muller et al., (2009) a humidified correction factor for the RR nephelometer was determined. This represents, to the best of our knowledge the first correction factor of this type for a RR nephelometer operating under humidified conditions. Without humidified measurements, a generic, size dependent correction factor would be applied to either the TSI or the Radiance Research nephelometer.

Correcting for humidified measurements requires the combination of the scattering coefficient dependence on Ångström exponent (provided in 3.3) with the relative humidity dependency on Ångström exponent. The latter is determined empirically from the light scattering coefficient data set as explained in Koloustsou-Vakakis 2001.

$$\frac{\sigma_{sp,neph(\lambda_1)}}{\sigma_{sp,neph(\lambda_2)}} = \left(\frac{\lambda_1}{\lambda_2}\right)^{-Åsp} \tag{3.3}$$

However, the scattering Ångström exponent (SAE) requires a humidity dependence correction as shown in 3.4.

$$SAE = 2 + C_1 * RH + C_2 * RH^2 + C_3 * RH^3 \quad (3.4)$$

A final corrected equation for the RR nephelometer while operating under humidified conditions was determined as shown in 3.5.

$$C_{ts} = 0.0166(2 + C_1 * RH + C_2 * RH^2 + C_3 * RH^3)^2 -$$

$$0.1305(2 + C_1 * RH + C_2 + RH^2 + C_3 * RH^3 + 1.2606 \quad (3.5)$$

The values of the correction factor coefficients as applied to the appropriate impactor size cuts are represented in Table 3.1.

Table 3.1. Correction Factor Coefficients for Humidified Measurements with a Radiance Research Nephelometer.

Particle Size Cut	**C_1**	**C_2**	**C_3**
Sub-1 µm	2.23e-2±1.67e-3	-3.73e-4±5.28e-5	1.58e-6±4.06e-7
Sub-10 µm	8.44e-3±2.05e-3	-1.95e-4±6.46e-5	9.58e-7±4.96e-7

CHAPTER 4-RESULTS AND DISCUSSION

This chapter is structured as follows.

- Section 4.1 presents monthly-binned aerosol optical property statistics, based on hourly-averaged data. The aerosol optical properties measured at APP are placed in the context of those measured at the other three U.S. NOAA-ESRL aerosol-monitoring sites mentioned in Chapter 2 in order to illustrate the high seasonal variability of aerosol optical properties measured at APP.
- Section 4.2 includes 10 years of MODIS-measured aerosol optical depth (AOD) to illustrate possible long-term AOD trends and to include seasonal variations in both variables, which serve as inputs for DRE calculations discussed in the following section.
- Section 4.3 provides the DRE calculations which employ the simple 1-D box model proposed by Haywood and Shine (1995) to estimate daily-averaged DRE for a $9km^2$ grid centered at the APP site. Calculations are based on daily-averaged aerosol optical properties, combined with satellite-measured aerosol optical depth, fractional cloud cover, and surface albedo at 700nm.
- Section 4.4 introduces preliminary aerosol hygroscopic growth measurements from the humidograph system. Results will be presented as seasonal frequency distributions with calculated mean and standard deviations for each season and for the

total time of measurements. In addition, several interesting events that will be discussed.

- Section 4.5 presents results from an agglomerative cluster analysis employed to aid in a proxy method of broadly classifying aerosol types without the use of direct chemistry instruments. Due to the large seasonal variability in aerosol optical properties, the results are shown for only summer and winter seasons as those are the most interesting and contrasting seasons. Results from the other seasons are found in Appendix 4.

4.1 Aerosol Optical Property Statistics-Comparison Between Four U.S. Sites

Multi-station plots of key aerosol optical properties measured at the four NOAA-ESRL aerosol-monitoring stations in the U.S. are presented in this section. The site names in all plots are abbreviated as follows. BND=Bondville, IL; SGP= Southern Great Plains, located in Lamont OK; THD=Trinidad Head, CA; and APP= Appalachian State University in Boone, NC. Sections 4.1.1-4.1.3 examine the aerosol light scattering and hemispheric back-scattering directly measured with the TSI nephelometer, along with the light absorption measured by the PSAP and the particle number concentration measured by the CNC. The remaining sub-sections detail variables calculated from these measurements, with particular emphasis on those used as part of the DRE calculations (section 4.3) and the cluster analysis (section 4.5) used to broadly classify aerosol types. Single-scattering albedo and hemispheric backscatter plots are also shown at 700nm, due to their approximation for broadband values used in the DRE calculations. Additional plots at both wavelengths can be found in Appendix 1.

All data at each site have been quality assured by site operators. Hourly-averaged for each site were binned by month and statistics are presented in the form of box-and-whisker plots, with the center bar representing the 50^{th} percentile, the top/bottom of box corresponding to the $75^{th}/25^{th}$ percentile, and the top/bottom of the whiskers extending to the $95^{th}/5^{th}$ percentile. Outliers are not displayed in the plots regardless of occurrence. Table 4.1 displays the convention for the breakdown of months into seasons.

Table 4.1. Convention for Seasonal Breakdown of Months. The abbreviation of each month is found in the parenthesis adjacent to the name of the month.

Convention For Seasonal Breakdown by Month			
Season	**Contributing Months**		
Spring	March (M)	April (A)	May (M)
Summer	June (J)	July (J)	August (A)
Fall	September (S)	October (O)	November (N)
Winter	December (D)	January (J)	February (F)

4.1.1 Aerosol Total Light Scattering and Light Absorption Coefficients (550nm)

Figures 4.1 and 4.2 illustrate total aerosol light scattering and aerosol light absorption coefficients respectively measured at 550nm for the four U.S. NOAA-ESRL sites. Both coefficients have units of inverse mega-meters (Mm^{-1}), where each Mm^{-1} corresponds to light attenuation due to scattering or absorption of one part per million in passing through one meter of atmosphere.

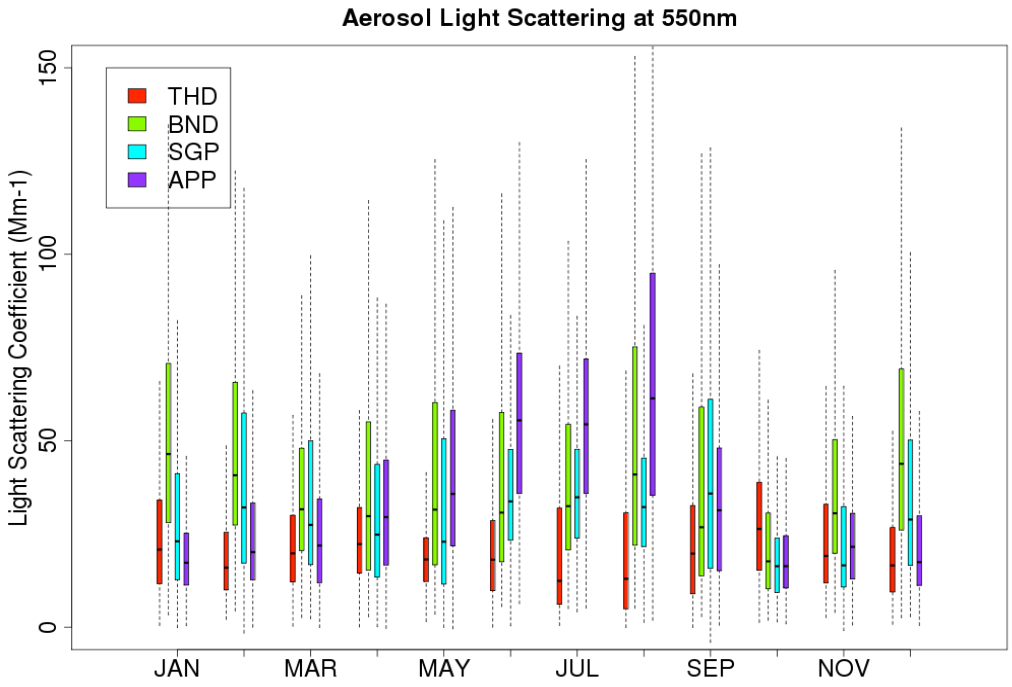

Figure 4.1. Statistical Plot of Multi-Station Aerosol Light Scattering Coefficients (Mm^{-1}) Measured at 550nm.

The highest seasonality in aerosol light scattering observed at APP is consistent with large amounts of secondary organic aerosols (SOA) produced in the south eastern U.S. during warm-season months by the oxidation of biogenic volatile organic compound (BVOC) precursor gases (Goldstein et al., 2009). SOA results from gas-to-particle conversion when the BVOCs react with gas-phase oxidants (often pollutants such as sulfur dioxide and nitric oxides) and chemical transformations occur. Variance of summer month values is roughly twice as much as during non-summer months. This variability may be due to the temperature and sunlight dependence of the emitted biogenic organic compounds.

The BND and SGP sites, located in less-forested areas with larger industrial and agricultural influences, exhibit much smaller seasonal variations, as does the THD site which is located in a temperate coastal environment in northern California which is largely influenced by sea salts on aerosol properties. This pronounced seasonality in scattering coefficients observed at APP is of key importance as it appears to be dominating other properties and will be discussed more in this chapter

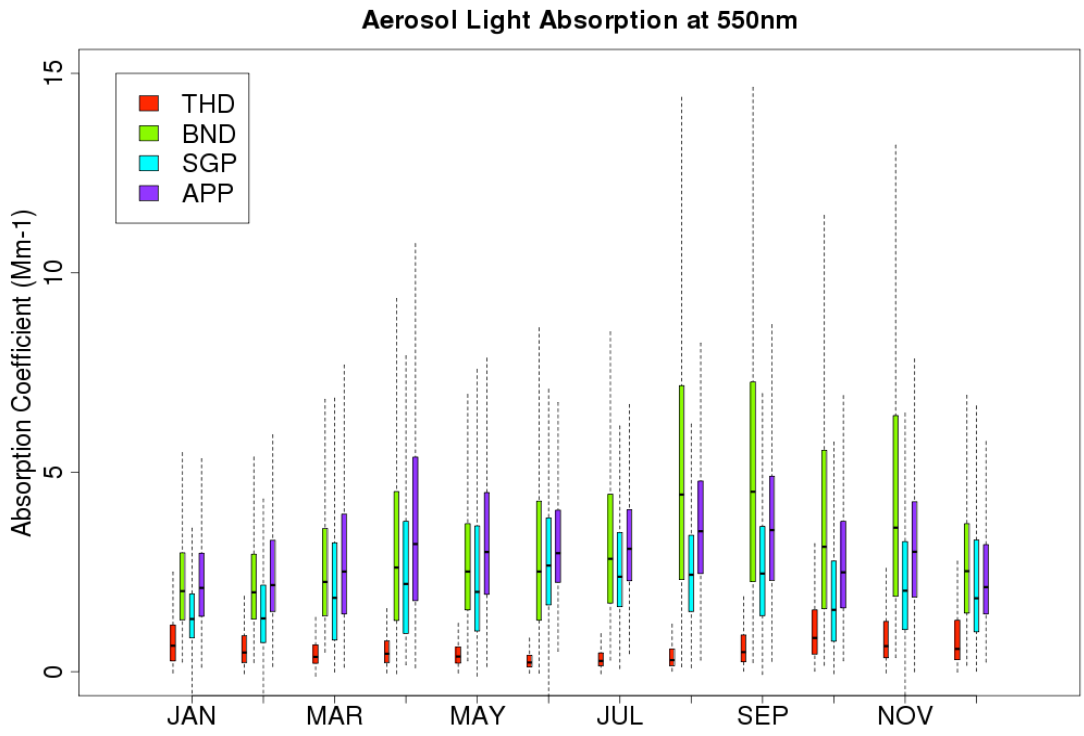

Figure 4.2. Statistical Plot of Multi-Station Aerosol Light Absorption Coefficients (Mm^{-1}) Measured at 550nm.

APP experiences an increase in absorption coefficients during spring and summer months (Figure 4.2). However, it is not as pronounced as the warm-season increase in scattering coefficients. Increased absorption coefficients during warmer months at SGP and BND are consistent with increased anthropogenic influence and mechanical disturbance of dust by

either large convection or frontal activity (Sheridan et al., 2001). THD has the lowest median values and monthly variability of absorption since the predominantly sampled aerosols are sea salts which are almost completely scattering particles (Seinfeld and Pandis, 2006). Analysis of the diurnal variability of absorption coefficients provides evidence of relatively minor influence of local anthropogenic sources on the scattering and absorption measurements made at APP. That plot and several additional plots can be found in the Appendix 1.

4.1.2 Single-Scattering Albedo SSA (550nm)

Monthly SSA statistics (Figure 4.3), defined as the fraction of light scattering to light extinction (the sum of absorption plus scattering) is a unitless variable shown in 2.5.
To place some context as to the magnitudes of values for certain particle types, highly scattering aerosols such as sulfates possess SSA values near 1.0 in the visible region while absorbing aerosols such as black carbon possess values approaching 0.21 (Haywood et al., 1997a). From Figures 4.1 and 4.2, it is seen that the large seasonal fluctuations in scattering observed at APP dominate the seasonal variability in SSA. Mean SSA values at APP are lowest compared to the other three sites during non-summer months with the exception of September and October in which BND has a lower mean value. During these non-summer months, certain particles possess SSA values below a critical value which can allow a positive radiative effect as will be seen later in this chapter. However, the abrupt change of increased SSA during summer months illustrates the possibility of large negative radiative effects driven by warm season aerosol light scattering.

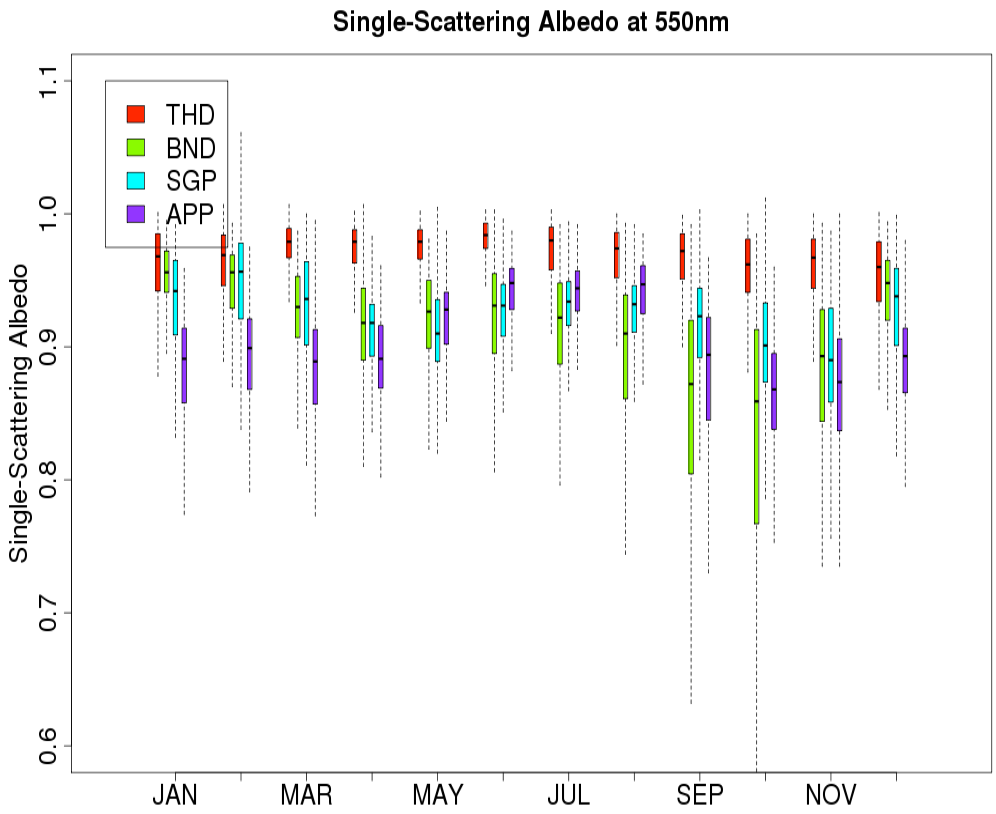

Figure 4.3. Statistical Plot of Multi-Station Single-Scattering Albedo (SSA) Measured at 550nm.

As mentioned earlier, THD samples primarily sea salts which primarily scatter light giving that site the highest SSA values. BND's SSA values are primarily attributed to sulfates from nearby coal-burning power plants. As recent as 2000, BND experienced the highest sulfate burden due to sulfates in North America (amongst current NOAA aerosol monitoring sites) which were sourced from nearby (Koloutsou-Vakakis, 2001). This explains the high values of SSA during certain months fall and winter months. The large decrease in SSA values at BND during the fall months has been attributed to farming activity next to the station.

However, as late as 2001 the agent most responsible for modifying the SSA values was unknown (Delene and Ogren, 2001)

4.1.3 Aerosol Number Concentration

Measured aerosol number concentrations, having units of particles per cm^3 are shown in Figure 4.4. Particle sizes are countable by the CNC if in the approximate range of aerodynamic diameter are approximately 25nm to 3µm. This range encompasses nearly all particles contributing to aerosol radiative effects in the SEUS and no efforts have been made to account for the particles outside of this size range.

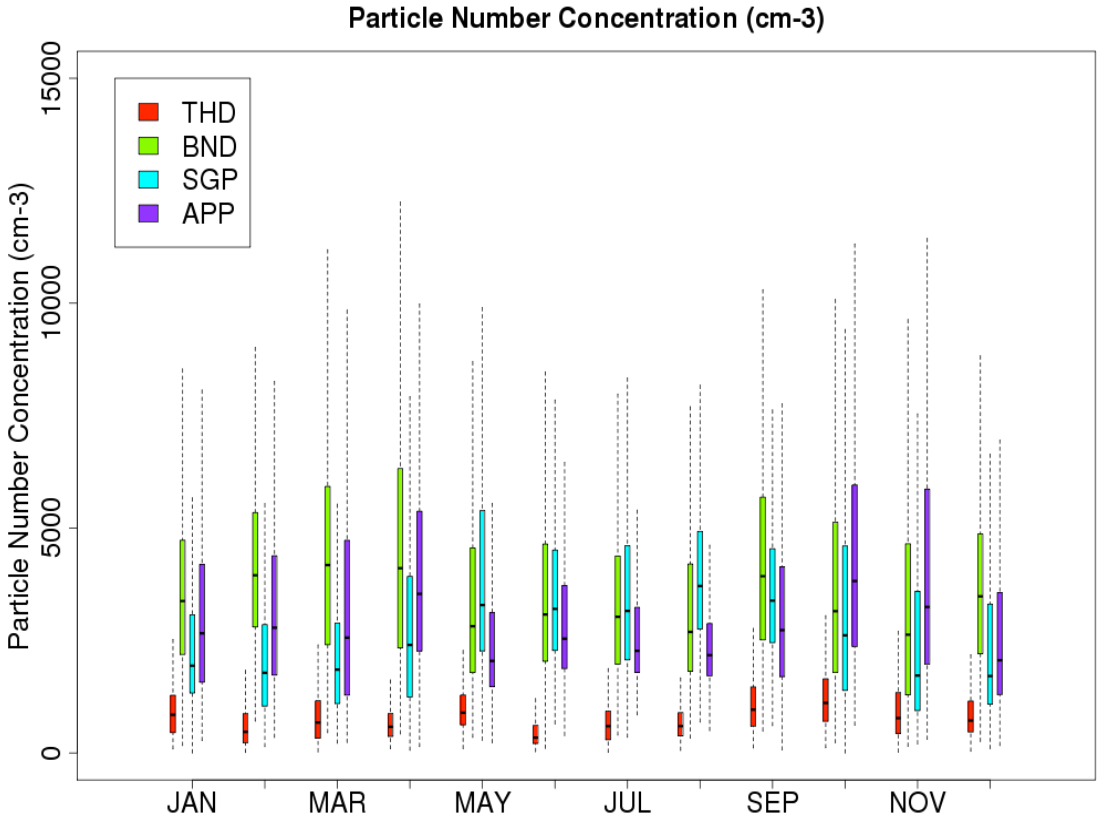

Figure 4.4. Statistical Plot of Multi-Station Aerosol Number Concentration.

Outside of summer months APP consistently displays larger concentrations than both SGP and THD. The inter-monthly variability is also reduced during summer months at APP which shows that the concentration of particles remains more similar during warmer months than during cooler months. Variability at APP in particle concentration most resembles the variability in the absorption coefficients. One possible explanation may be linked to changes in carbonaceous particles brought on by warmer temperatures and increased ambient humidity which causes similar particles to group together thereby decreasing the overall concentration during those months.

4.1.4 Hemispheric Backscattering Fraction (550nm)

Hemispheric backscatter fraction (Figure 4.5) is a unit-less parameter (□) as it is the ratio of light scattered into the backward hemisphere (90º-180º scattering angles, referenced to the direction of the illuminating light) to the total light scattered in all directions represented with 2.6.

Smaller particles (Figure 4.5) are apparent when number concentrations (4.4) are highest and the opposite occurs with larger particles having lower number concentrations. The largest particles at APP occur in the summer which may be due to increased tendencies of particle to group or bond together. APP experiences an interesting anti-correlation between SSA and *b* in which the backscatter fractions at APP are far more variable than at any other site. Fall months at APP display large variations in daily backscatter fractions when compared to the other nine months which are fairly similar. The relative size of the particles at the three other

sites remained roughly constant with THD being almost stagnant in variability of particle size throughout the year.

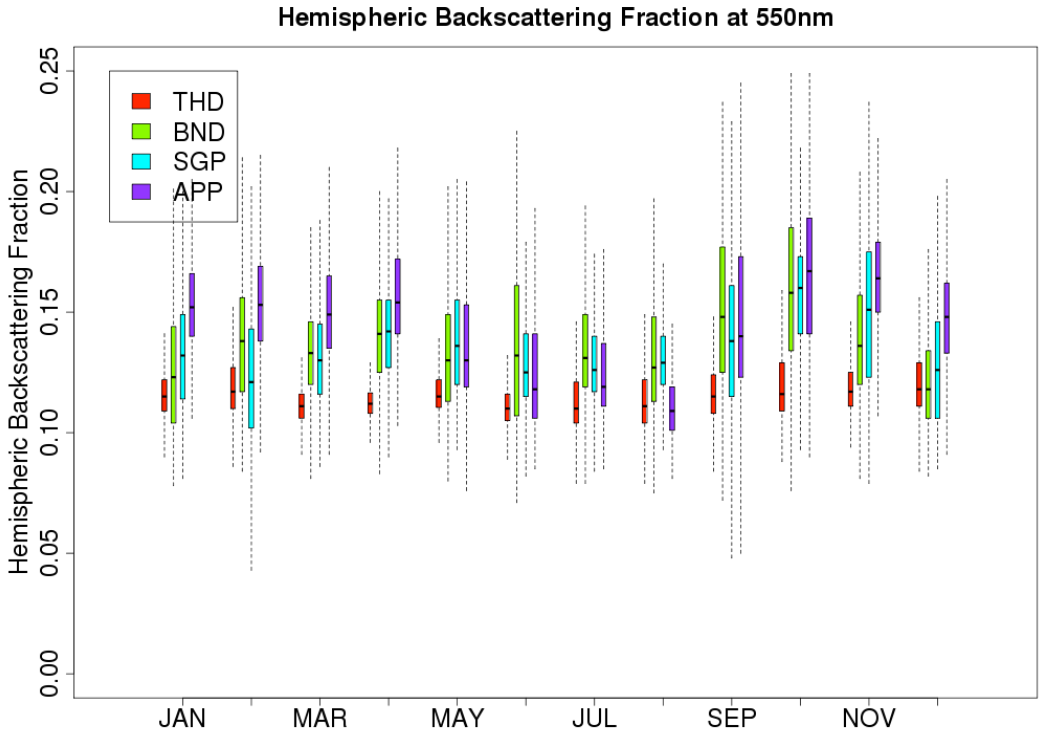

Figure 4.5. Statistical Plot of Multi-Station Hemispheric Backscatter Fractions (*b*) Measured at 550nm.

4.1.5 Submicrometer Scattering and Absorption Fractions (550nm)

Submicrometer scattering fraction (Figure 4.6) is the ratio of sub-1 μm scattering coefficients to sub-10 μm scattering coefficients. The closer the ratio is to unity, the more of an influence sub-1 μm diameter particles are having on aerosol light scattering coefficients.

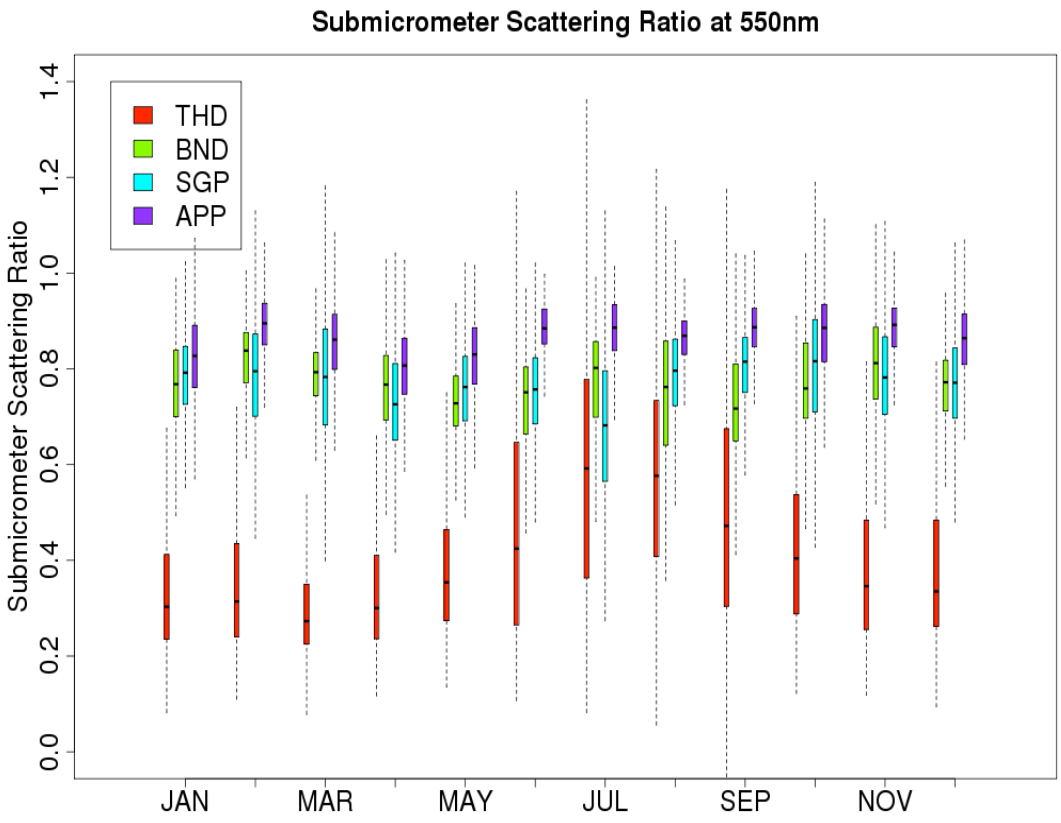

Figure 4.6. Statistical Plot of Multi-Station Submicrometer Scattering Ratio Measured at 550nm.

For all months APP has the highest values of sub-micrometer scattering fractions which indicate that the light scattering properties measured at the site are dominated by particles with diameters smaller than 1 μm. In addition to APP having the highest median values, the site also exhibits the tightest upper and lower quartile widths indicating lower monthly variability of the contributions of these smaller particles. APP experiences fair variability of the monthly median values throughout the year with THD being the site with the most monthly median variability between months. THD monitors large amounts of sea salts which are produced as larger particles causing that site to have the lowest sub-micrometer scattering ratio. The THD summer months increase in scattering fraction may be due to influence from

the mainland, possibly from biomass burning or an increase in emissions from marine vessels.

Submicrometer absorption fraction (Figure 4.7) is the ratio of light absorption coefficients between the two impactor size cuts. As this ratio approaches unity the more of an influence the sub-1 μm particles are having on the aerosol light absorption coefficients.

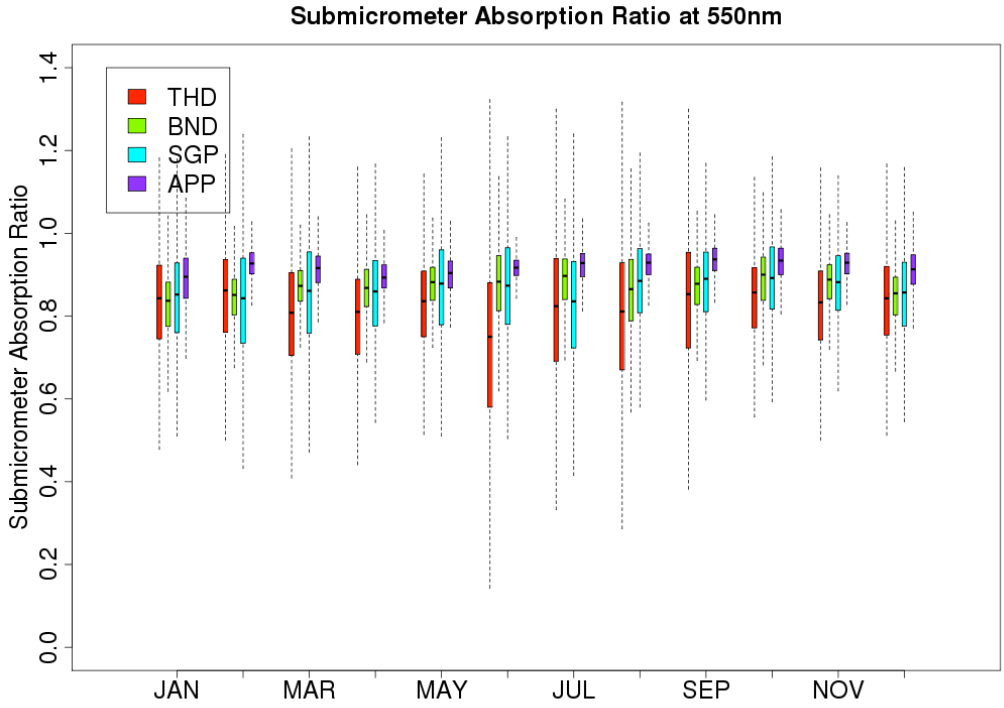

Figure 4.7. Statistical Plot of Multi-Station Submicrometer Absorption Ratio Measured at 550nm.

APP has the highest median values and least variability indicating the strongest influence of sub-micron particles on the light absorption coefficients. APP, as mentioned earlier should not sample much if any dust particles or sea salts which are larger mechanically driven primary aerosols. The very tight quartile (box) widths indicate that there are a minimal

amount of localized or extreme events affecting the value and that APP is likely sampling aerosols from a few predominant source regions fairly consistently. The increased variability at THD may be from mainland biomass burning or increased marine vessel traffic.

4.1.6 Absorption Ångström Exponent (AAE)

Monthly-binned statistics for the AAE (Figure 4.8) provide an indicator of the variation of absorption with wavelength which can be used to distinguish between OC and EC. This variable is calculated based on equation 2.8.

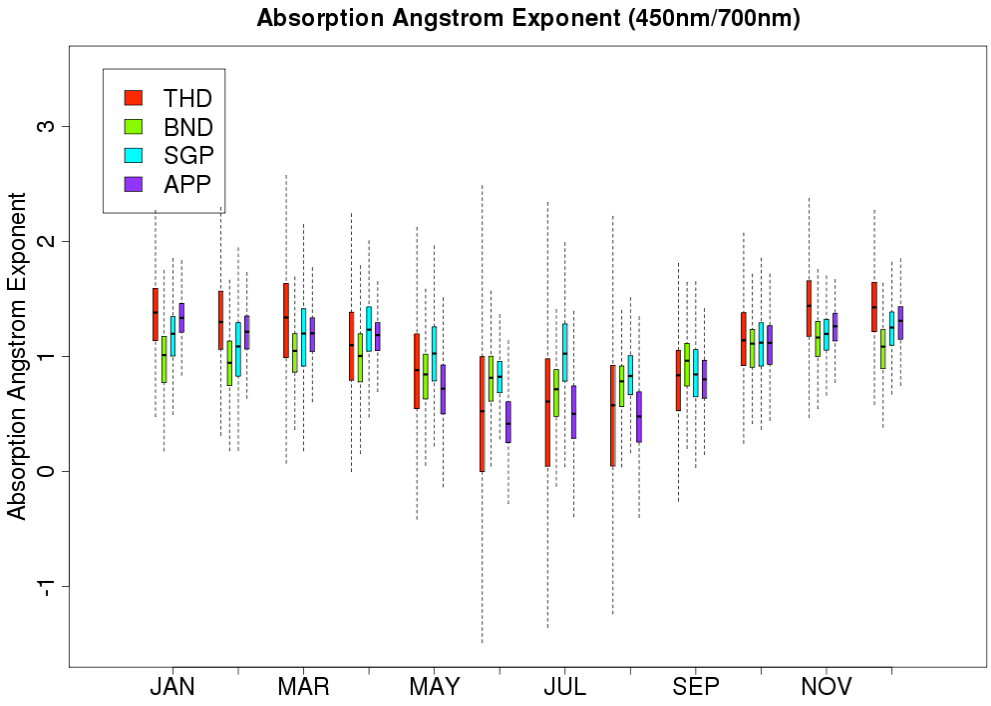

Figure 4.8. Statistical Plot of Multi-Station Absorption Ångström Exponent (AAE) Measured Between 450 nm and 700 nm.

This variable can be used as a proxy for understanding carbon source, concentration and relative age as the actual magnitudes must be considered with care due to the limited spectral band of 450nm-700nm. We shall assume for the sake of making any comparisons that the

lower the values are the more likely the particles being sampled are fresher concentrations of BC while larger values represent higher and older concentrations of OC. However, this alone cannot give chemical composition but can help diminish the ambiguities in aerosol composition analysis (Russell et al., 2010). SGP is likely to experience larger amounts of dust and biomass burning from agricultural activities which may provide a dominant signal at that site for much of the year. The reduction in median values during summer is possibly due to increased concentrations of EC. APP also changes relative position of ranking with SGP, being higher during non-summer months and lower during summer months. All sites experience a reduction of AAE values during summer months as this is consistent with reduced biomass burning for heating with exceptions due to wild fires. The mean values between all sites are fairly similar except that THD experiences a wider range of values during the same portion of time.

4.1.7 Radiative Forcing Efficiency at 550 nm and 700 nm

Aerosol radiative forcing efficiency is a normalized per unit optical depth radiative variable with units of Wm^{-2} per AOD which provides a representative number of the efficacy of a particle to alter climate (Koontz and Ogren 2003). The use of globally-averaged geophysical parameter, such as surface reflectivity, daylight fraction, and cloud fraction facilitates qualitative comparisons of aerosol optical properties (through variations in SSA in upscatter fraction) measured at different sites. The value at 550nm provides an indicator of the ability of various aerosol types to modify solar radiation near the solar peak while the value at 700nm is used as an estimate for the broadband effects

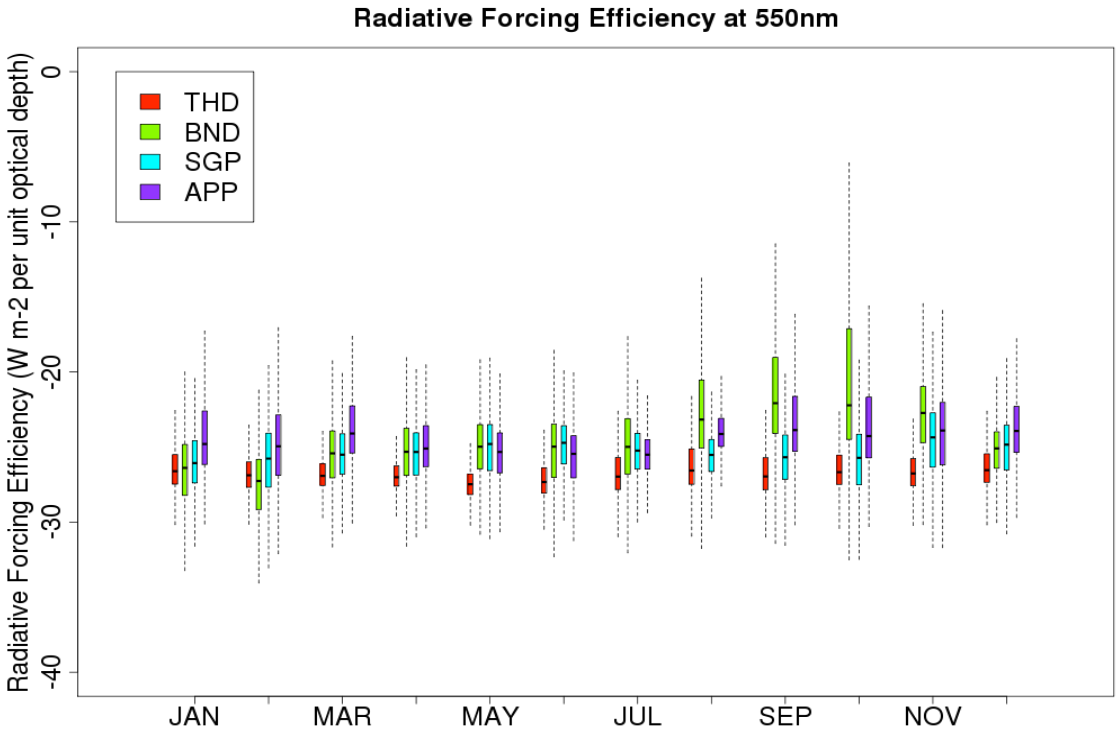

Figure 4.9. Statistical Plot of Multi-Station Radiative Forcing Efficiency Calculated at 550 nm [Wm^{-2}/AOD].

The results presented in Figure 4.9 are consistent with previous studies in that the more pronounced the changes in SSA and *b* measured at a site the more pronounced an impact on the radiative effects (Delene and Ogren, 2001) as seen in the seasonality at APP and BND. Summer months at APP experience a similar variability as seen in the scattering coefficients and σ_{sp} values but the magnitude of the variability is being buffered by the *b* values as those particles scatter less light into the backward and ultimately the upward hemisphere which may reduce the amount of radiation being reflected at the TOA. Particles at THD possess the greatest capability for altering regional climate but lower number concentrations (Figure 4.4) indicates that the magnitude of attenuated radiation may be much reduced when compared to APP or the other sites.

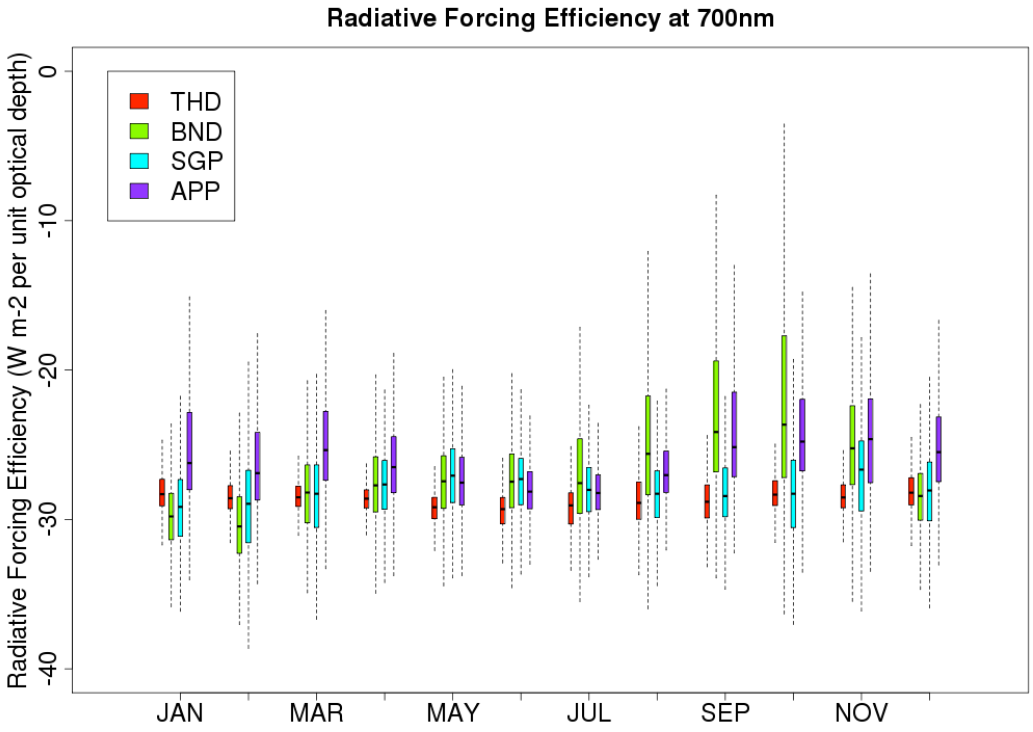

Figure 4.10. Statistical Plot of Multi-Station Radiative Forcing Efficiency Calculated at 700 nm [Wm^{-2}/AOD].

When comparing Figure 4.1.10 to 4.1.11 there is a slightly higher spectral dependence exhibited at APP as the variability and relative magnitudes of forcing efficiency change slightly when considering the longer wavelength and amongst THD and SGP but not BND. The sea salts at THD could be affecting solar radiation greatly as they are predominantly scattering particles. The buffering effect of *b* is less pronounced at 700nm as compared to 550nm at APP. A later section of this chapter will provide long term AOD values at APP which will provide the relative optical loading through the column of atmosphere over the site.

4.2 Remotely Sensed Properties and An Investigation of 10 years of MODIS AOD Values at 550 nm

4.2.1 MODIS Cloud Fraction (A_c)

As cloud fraction is needed for DRE calculations a quick investigation of the variability of that variable must precede investigation of the actual results of the DRE calculations. Figure 4.11 displays the cloud fraction measured from the MODIS (Aqua) satellite for a 9km^2 area centered at the APP site.

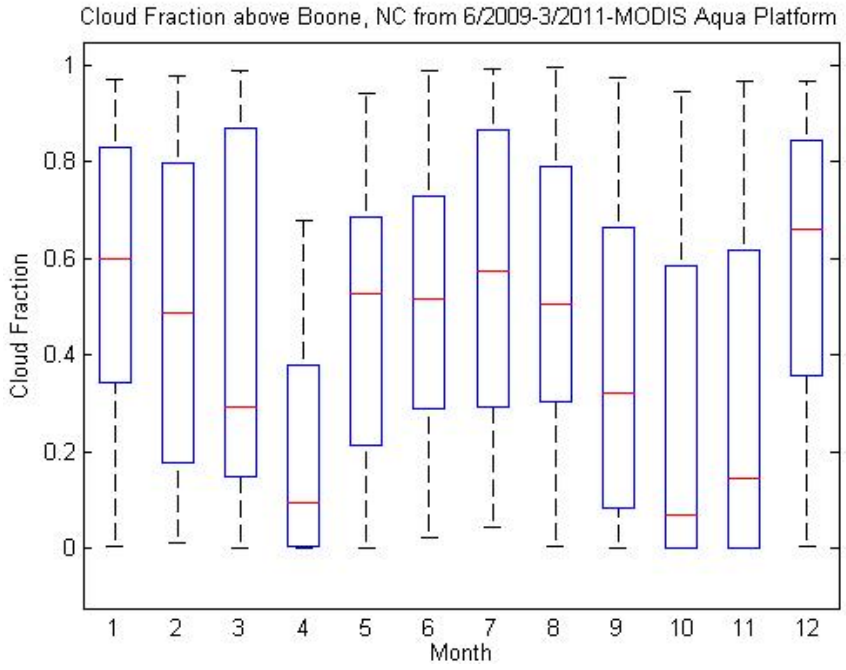

Figure 4.11. Statistical Plot of Monthly Binned MODIS Cloud Fraction Measured Over APP. Calculated using daily averaged cloud fraction values measured between 6/2009-3/2011 Month 1 corresponds to January and ends with December as months 12.

Seasonal mean values are highest during summer and winter. During the transitional months around summer such as March (3), April (4), October (10), and November (11), the lowest monthly mean values of fractional cloud covers occur.

4.2.2 MODIS AOD at 550 nm and 700 nm.

The figures below are of monthly binned MODIS provided AOD at 550nm (Figure 4.12) and 700nm (Figure 4.2.3) respectively.

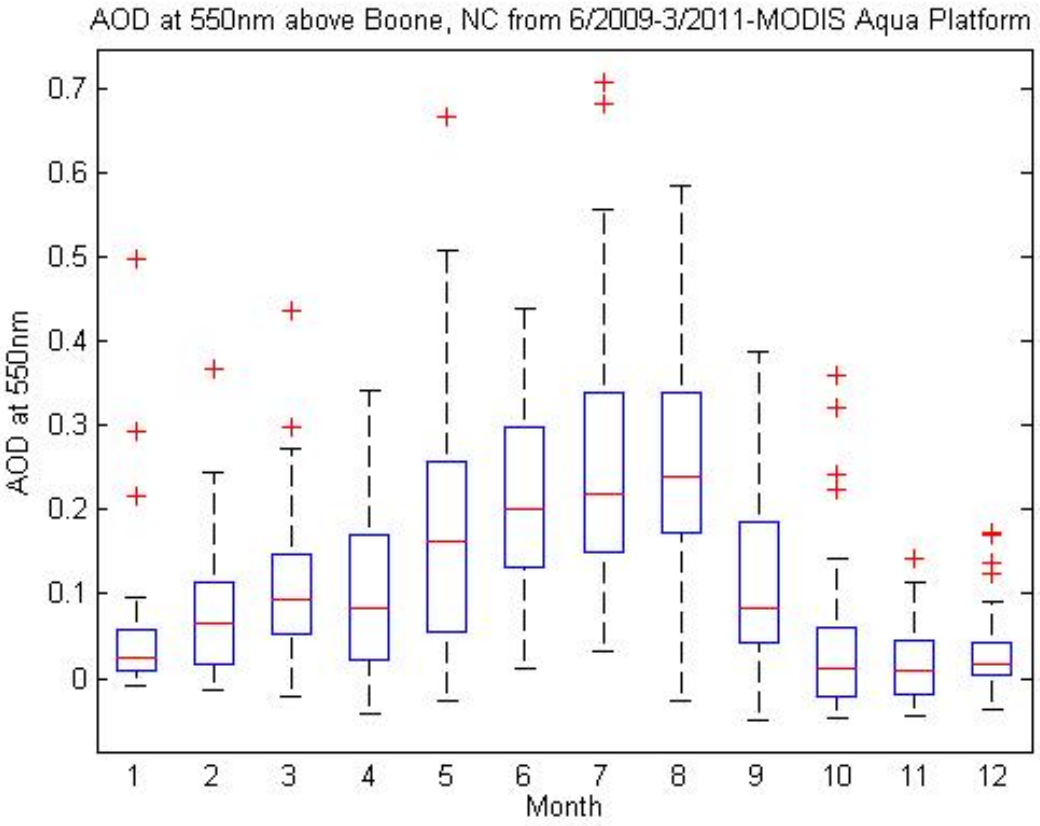

Figure 4.12. Statistical Plot of Monthly Binned MODIS AOD Measured at 550nm over APP. Calculated using daily averaged AOD (550 nm) values measured between 6/2009-3/2011.

As there is not a MODIS spectral band centered at 700nm, the value at 550nm was scaled to 700nm using the NASA AERONET retrieved Ångström exponent ($Å_{EXT}$) as represented with 4.1.

$$AOD_{700nm} = AOD_{550nm} * \left(\frac{550nm}{700nm}\right)^{Å_{EXT}} \quad (4.1)$$

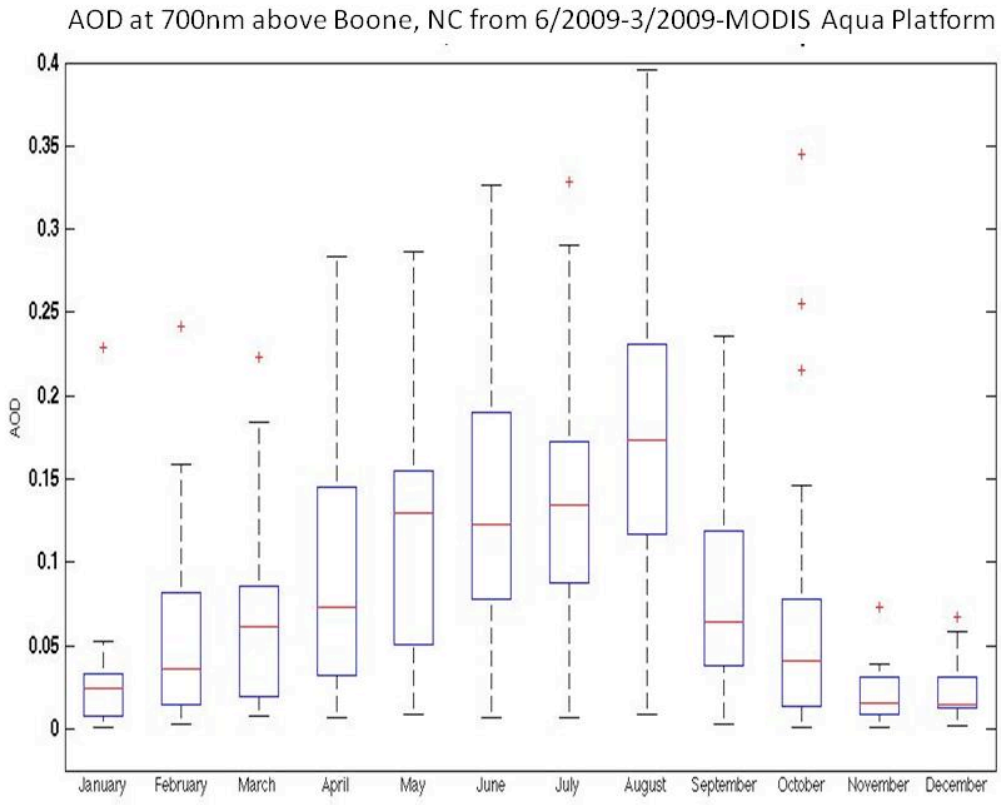

Figure 4.13. Statistical plot of monthly binned MODIS AOD (700 nm) over APP. Calculated using daily averaged AOD (550 nm) values measured between 6/2009-4/2011 and scaled to 700 nm using the NASA AERONET Ångström Exponent.

By comparison of the AOD and scattering plots, the seasonality appears to be driven by the scattering variations. There is roughly a factor of three difference between summer median values and non-summer median values. The variability between the months also increases during the warmer months. Median values and monthly variability are lowest during winter months which will also be shown later to have the lowest radiative effects.

4.2.3 Ten Years of MODIS AOD at 550nm

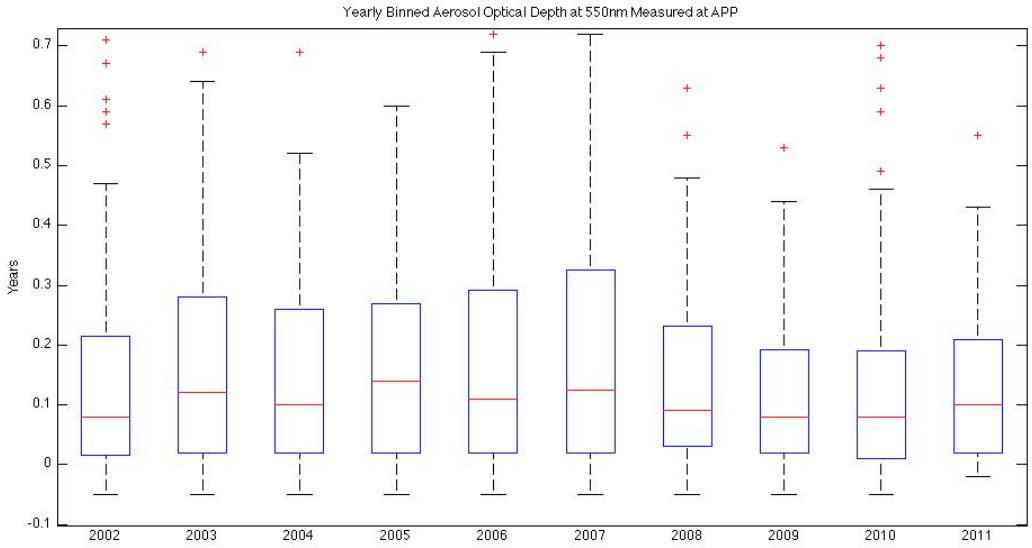

Figure 4.14. Statistical Plot of 10 Years of Yearly Binned MODIS AOD (550nm). Measured between May 2002 and May 2011.

A decade long comparison of AOD (Figure 4.14) provides information into the yearly changes in optical loading of atmospheric aerosols. What can be understood from Figure 4.14 is the reduction in yearly variance following 2007. Long-term AOD measurements, in combination with aerosol optical properties, should provide valuable information regarding the effects of recent legislation (Clean Air act and amendments) on southeastern U.S. regional aerosol loading and direct radiative effects.

4.3 Direct Radiative Effect (DRE)

Direct Radiative Effect (DRE) calculated using equation 2.13, is the term used to describe the perturbation of climate through the scattering and absorption of solar radiation by aerosols (Charlson et al., 1992; Kiehl and Briegleb, 1993). By definition, DRE is the change in the net down-dwelling radiative flux due to the presence of atmospheric aerosols (Figure 2.8).

The change in net flux is sometimes referenced to conditions of aerosol loading pre-industrial revolution but will be referenced to the zero-aerosol condition in this thesis. DRE is typically calculated at either the TOA or at the bottom of atmosphere (BOA). All calculations in this thesis refer to TOA DRE. The sign and magnitude of aerosol DRE depends on the aerosol loading in the atmospheric column, aerosol optical properties, and geophysical variables such as surface albedo.

Aerosol DRE calculations performed as part of this thesis will employ the simple box model discussed in Haywood and Shine (1995). This model makes an approximation that the investigated column of atmosphere is homogeneous which allows surface based measurements to be used as representative values throughout the atmosphere. The simple equation applies for an optically-thin atmosphere, meaning that the AOD is much less than 1.0. This condition nearly always applies at the APP location.

Monthly averages of surface reflectance were used as the daily and weekly variance was not substantial enough to justify daily values of the parameter while daily averaged values of AOD, A_c, SSA, and upscatter fraction were used for the calculations.

4.3.1 Statistics for Data Products Used in the DRE Calculations

While geophysical parameters and extrinsic aerosol optical properties are important, consideration and discussion of several intrinsic aerosol optical properties must occur to understand the variability in DRE calculations. The coupled relationship between SSA and

upscatter fraction have been shown to be two of the more influential variables in determining DRE sign and magnitude (Delene and Ogren, 2001).

Figures 4.15 and 4.16 illustrate the multi-station SSA and the APP site upscatter fractions calculated at 700nm.

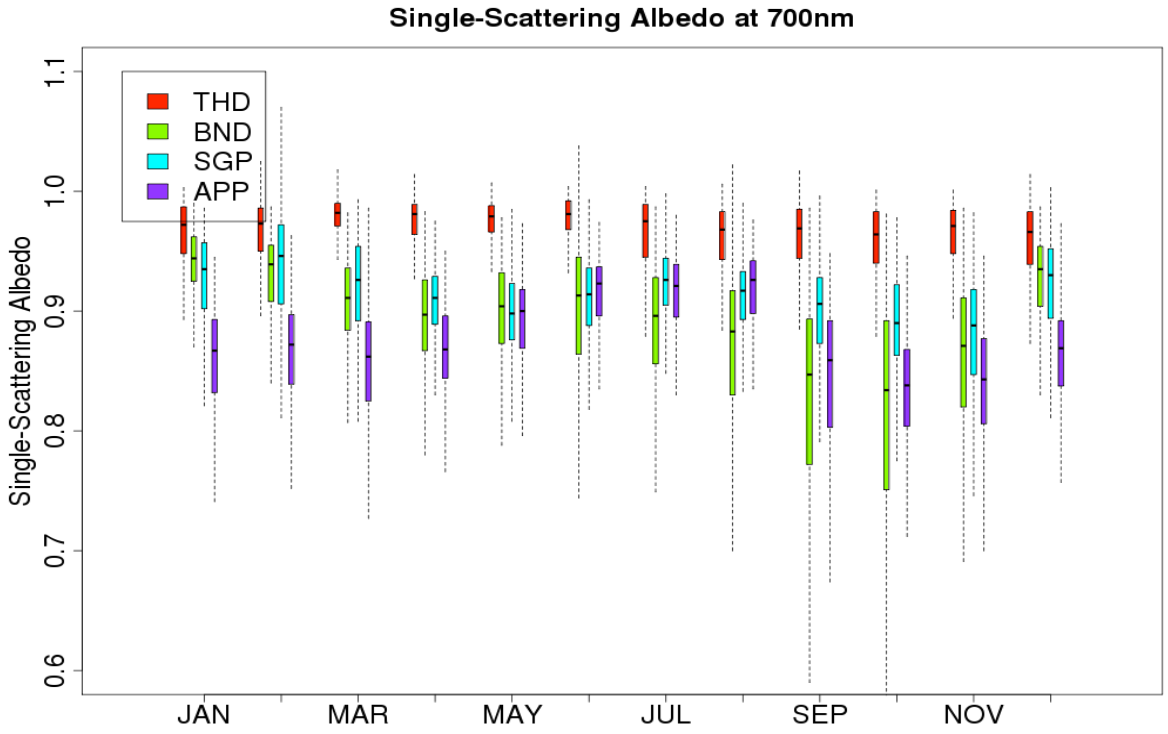

Figure 4.15. Statistical Plot of Multi-Station Single-Scattering Albedo (SSA) (700 nm).

Both figures display the same pronounced seasonality discussed in the previous section while being anti-correlated with each other. The percentage of radiation scattered upwards compared to the total scattered radiation is much reduced (~30%) during summer months as compared to the other three seasons. This is due to sampling larger particles during summer months which is consistent with the explanation by Koontz and Ogren (2003) as to the

behavior of this variable with changing particle size. However, the particles that are being sampled have very high scattering capabilities during the summer months at APP relative to the non-summer months.

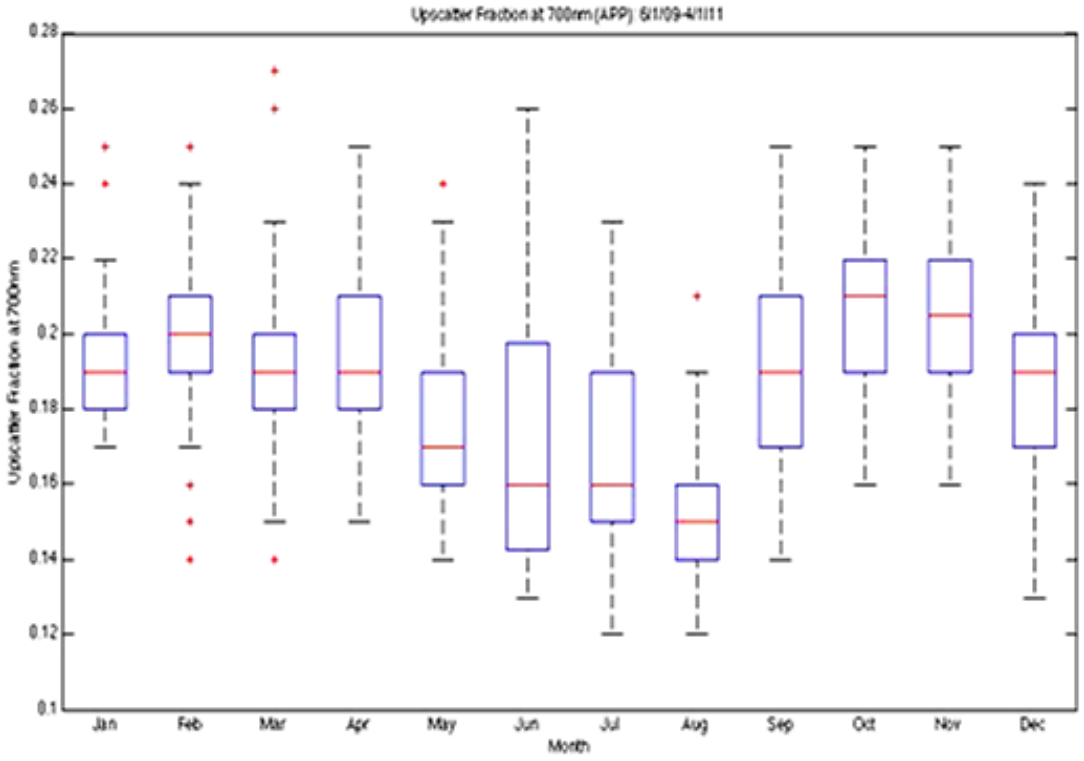

Figure 4.16. Statistical Plot of Monthly Binned Upscatter Fractions Measured at 700 nm from APP site.

4.3.2 DRE Statistics

Investigation of the preliminary results of the box model DRE calculations from APP (Figure 4.17) reveal some interesting trends and mean values.

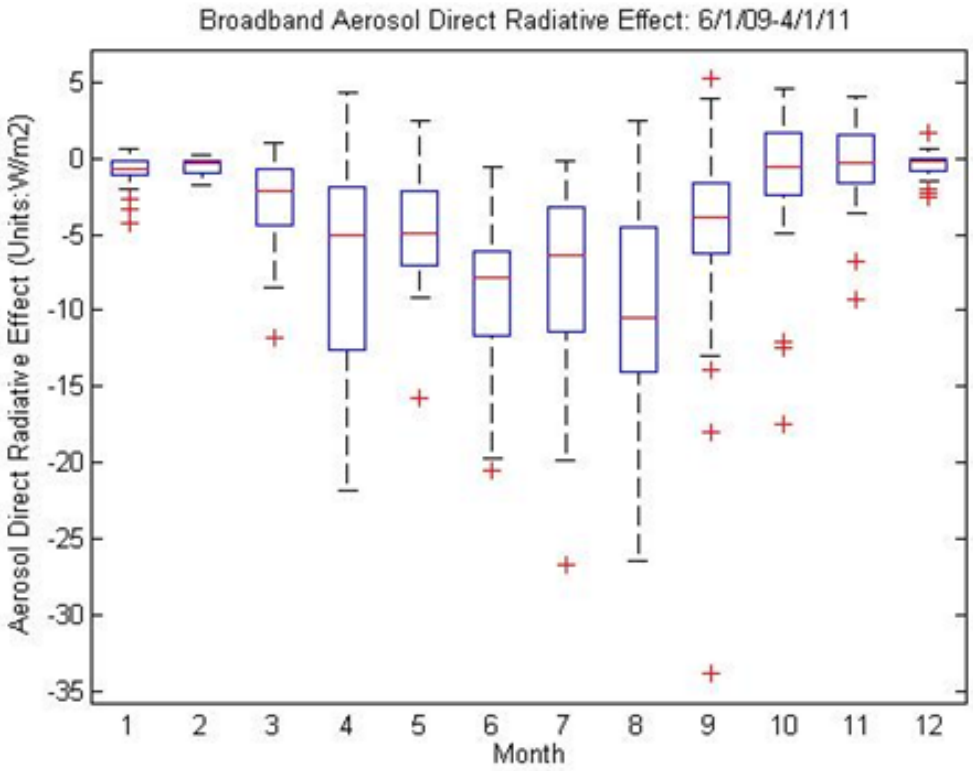

Figure 4.17. Statistical Plot of Monthly Binned Broadband DRE (700nm). Uses In Situ Intensive Optical Property Values with Remotely Sensed Data Products. Measurements Made Through the Column over APP.

The most important and salient point is the overall seasonally driven increase in magnitude of negative radiative effects during summer months. A mean summer time radiative effect of roughly -10w/m^2 was calculated based on this preliminary model. The monthly median variability most appropriately can be explained with changes in AOD. Overall trends in median DRE values most closely resemble the monthly trends in AOD. In addition, from investigation of the aerosol light scattering coefficients and SSA values, it is evident that AOD is being driven by an abundance of particles whose extinction is dominated by scattering rather than absorption. Winter has the lowest mean values which are to be expected based on several factors. There is a large reduction in AOD, roughly a factor of three or more during winter as compared to summer. Couple reduced AOD with reduced

daylight fraction and increased surface albedo and the results become reduced days of negative radiative effects. Fall experiences the most days with positive direct effect values. This is primarily due lower values of SSA and negative values of AOD.

Since much of the objectives of this long term monitoring are to gain a better understanding of the changes in regional climate, some discussion surrounding the radiative effects between years was considered and is discussed in the following.

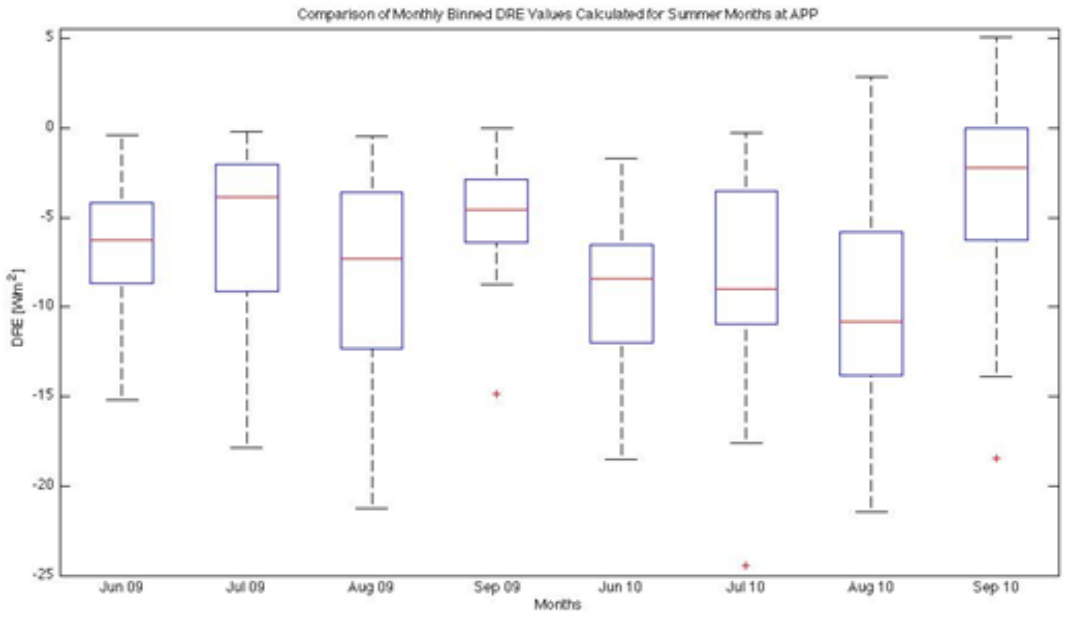

Figure 4.18. Statistical Plot of Monthly Binned Broadband (700 nm) DRE Calculations for the Summer Months Plus September of 2009 and 2010

The three warmest season months experienced more radiative effects during 2010 than in 2009. Median DRE values during June 2010 increased by nearly a factor of two as compared to 2009.

Since the production of SOAs during warm season months is consistent with emissions of temperature and sunlight dependent BVOCs, a qualitative analysis of the changes in regional BVOC emissions can be made using National Climate Data Center (NCDC) precipitation (Figure 4.19) and temperature (Figure 4.20) data.

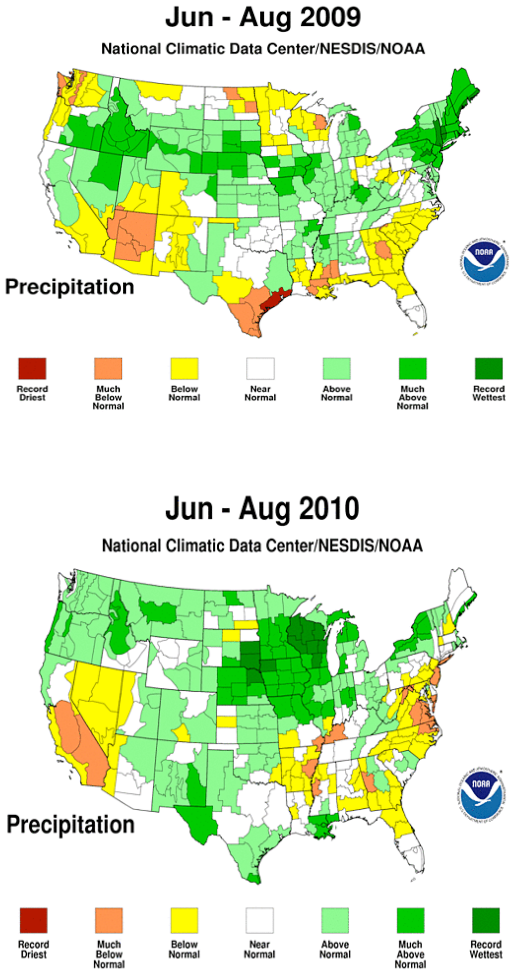

Figure 4.19. National Climate Data Center (NCDC) Precipitation Plots for Summer 2009 (top) and 2010 (bottom).

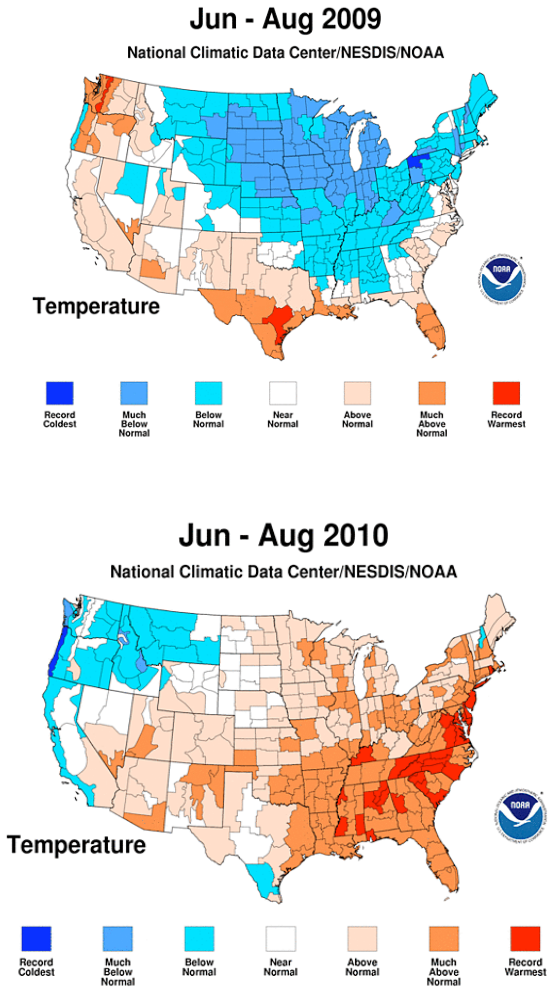

Figure 4.20. National Climate Data Center (NCDC) Temperature Plots for Summer 2009 (top) and 2010 (bottom).

From this NCDC data, 2009 experienced slightly less precipitation and cooler temperatures during summer as compared to 2010 which may have produced a feedback effect, which is caused an increased production of biogenic emissions.

4.4 Humidograph Results

The following section is intended to provide initial results of the humidograph system using the current state of characterization explained in Chapter 3. Prolonged periods of

measurements have proven to be very difficult, due to occasional humidograph membrane failures, leading to instrument flooding and subsequent loss of data. Table 4.2 provides some hygroscopic growth factors represented with 3.2 statistical results for all seasons followed by a season by season discussion.

Table 4.2. Statistics of Hygroscopic Growth Factors for Both Size Cuts for the Three Seasons of Operation

Size Cut and Season	Total Number of Occurrences	Mean f(RH) Values	f(RH) Mean Standard Deviations
Sub 10 fall	1012	2.08	0.35
Sub 1 fall	1012	1.86	0.27
Sub 10 winter	1882	1.84	0.36
sub 1 winter	1882	1.98	0.35
Sub 10 spring	1086	1.91	0.27
Sub 1 spring	1090	1.87	0.35

4.4.1 Fall Hygroscopic Growth Factor Results

Fall months (SON) have a mean value of 2.08 for all particles (Sub-10 μm) indicating the total light scattering coefficient at 85% RH to be a factor of 2.08 larger than the magnitude of the total light scattering coefficient at 40% RH. This is the largest hygroscopic growth of the three seasons (Figure 4.19), summer is expected to be highest of all seasons once the data has been accumulated and edited. However, there is insufficient data as of May 2011 to perform any analysis. Interestingly the sub-micrometer hygroscopic growth factor has the lowest

mean value of 1.86 (Figure 4.20). Perhaps due to a transitional aerosol regime that exhibits more prominence exiting summer than entering as would be seen in spring data.

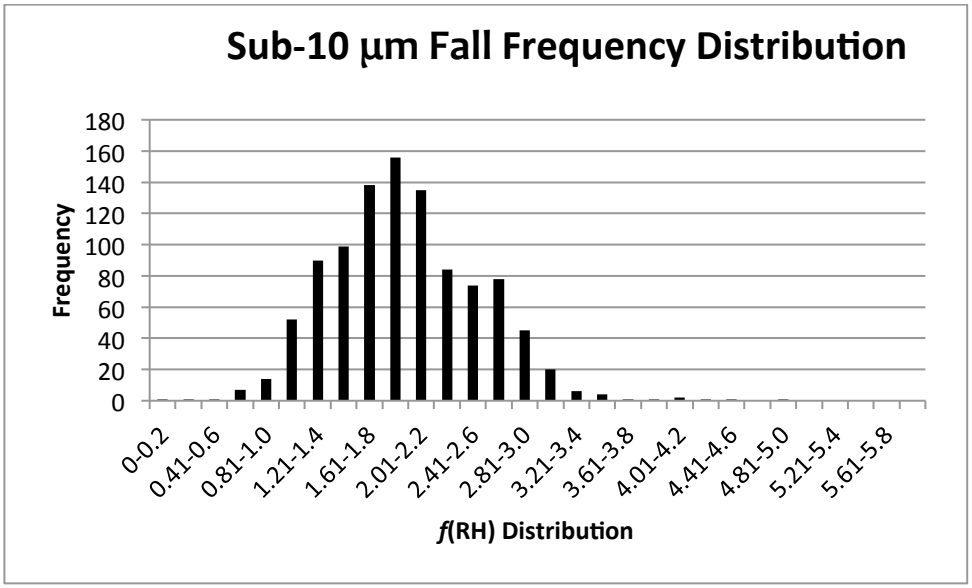

Figure 4.21. Fall Hygroscopic Growth Factor f(RH) Frequency Distribution for Sub-10 Size Cut

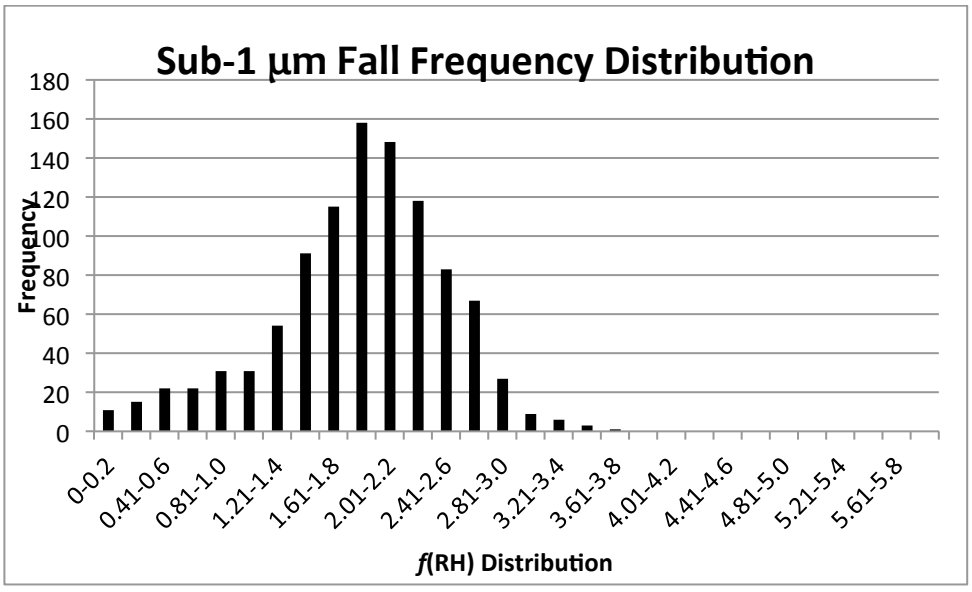

Figure 4.22. Fall Hygroscopic Growth Factor f(RH) Frequency Distribution for Sub-1 Size Cut.

4.4.2 Winter Hygroscopic Growth Factor Results

Winter months (DJF) reveal very similar distributions of hygroscopic growth factors around 1.9. There is also a different behavior compared to the other seasons where the sub-micrometer sized particles (Figure 4.21) exhibit higher hygroscopic growth factors than sub-10 micrometer particles (4.22). This indicates the scattering properties of the smaller particles are more greatly affected than similar light scattering properties for larger particles.

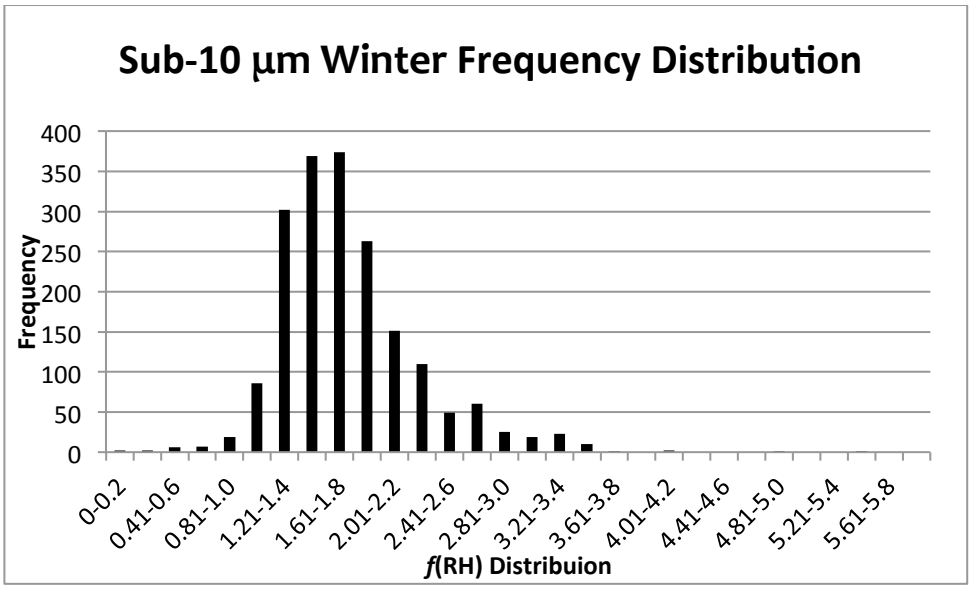

Figure 4.23. Winter Hygroscopic Growth Factor f(RH) Frequency Distribution for Sub-10 Size Cut.

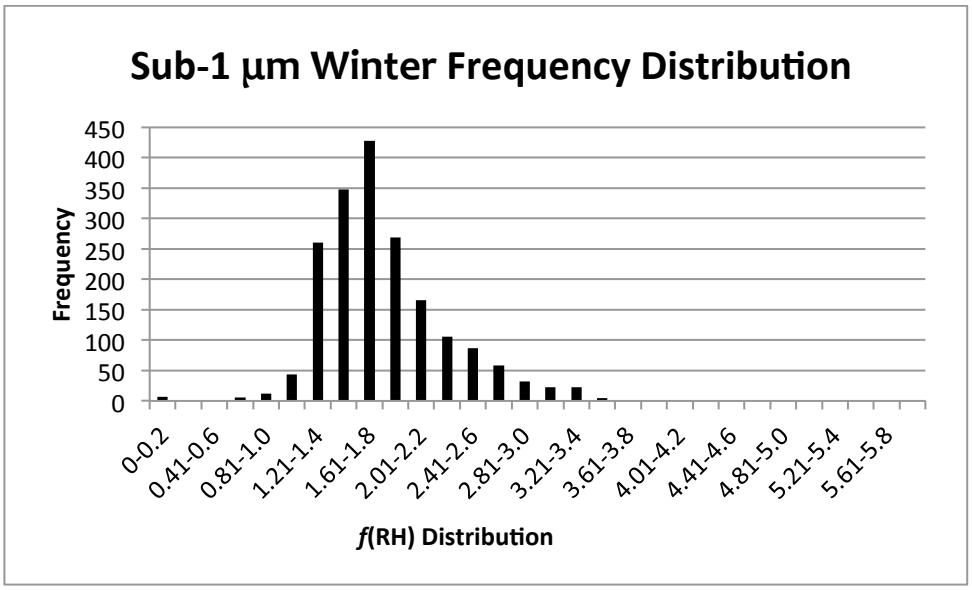

Figure 4.24. Winter Hygroscopic Growth Factor f(RH) Frequency Distribution for Sub-1 Size Cut.

4.4.3 Spring Hygroscopic Growth Factor Results

Spring exhibits the lowest variability amongst the seasons which prior to this analysis might have been thought to exhibit wide variability being the transitional months following summer where we have seen (Section 4.1) immense variability.

The lack of long-term hygroscopic growth measurements at other NOAA-ESRL site prevents detailed comparisons. The mean value for all months and size cuts was measured at APP and calculated to be 1.92±0.33. As of the time this data was available APP exhibited higher f(RH) values than another NOAA ESRL site. Sheridan et al., 2001 determined (using a duel TST nephelometer humidograph system) that the mean f(RH) value at SGP to be 1.83. APP data strangely corresponds closest with the value of 1.91±0.16 found during the monitoring of pollution events sourcing from Korea (Kim et al., 2001). Any increase in the mean value

could create results more consistent with that of the TARFOX experiment in which f(RH) values ranged from 1.81±0.37 – 2.30±0.24 (Jeong et al., 2007).

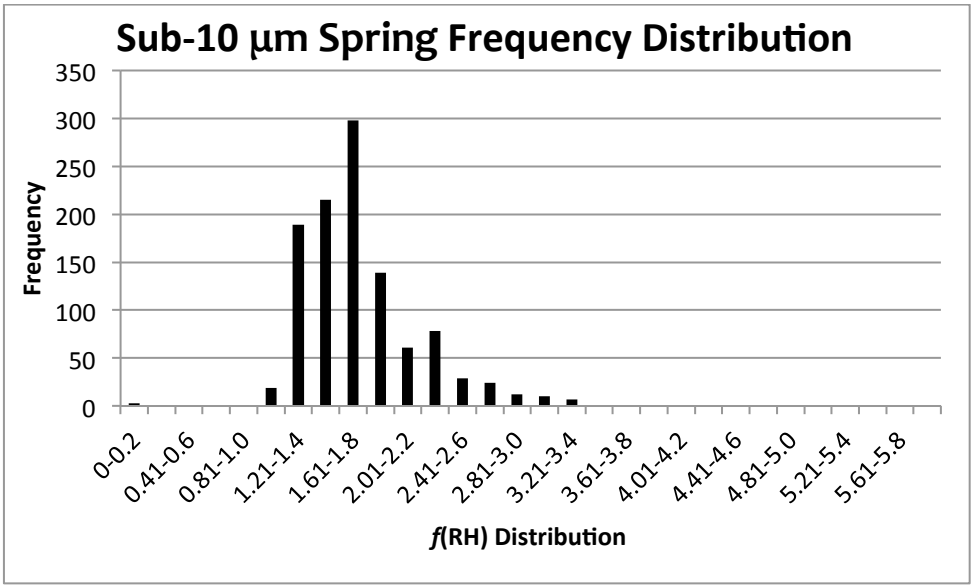

Figure 4.25. Spring Hygroscopic Growth Factor f(RH) Frequency Distribution for Sub-10 Size Cut.

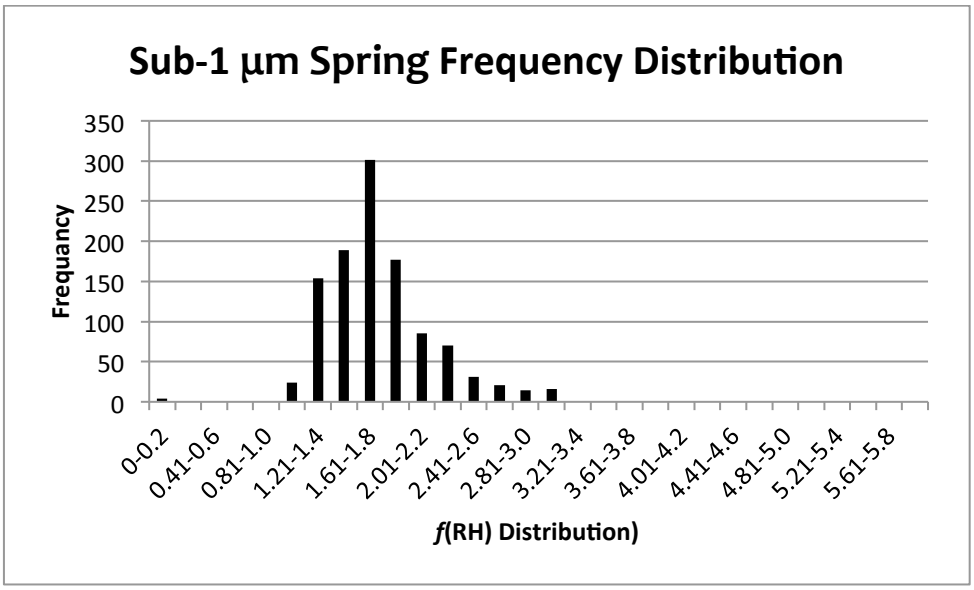

Figure 4.26. Spring Hygroscopic Growth Factor f(RH) Frequency Distribution for Sub-1 Size Cut.

4.4.4 Periods of Interesting Hygroscopicity

During the limited operation time there have been some interesting events which will be discussed below. A period of anti-correlation between hygroscopic growth factors and aerosol light scattering coefficients at 550nm was monitored and displayed below.

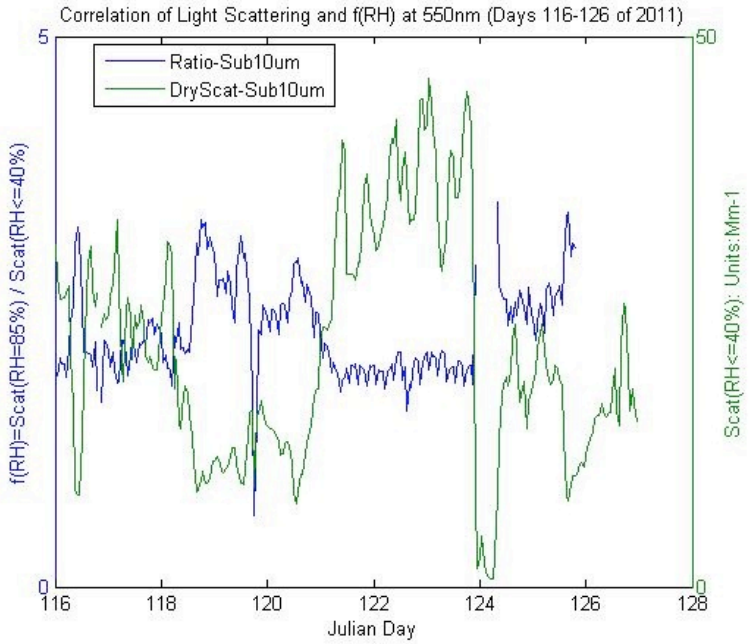

Figure 4.27. Period of Anti-Correlation Between Scattering Coefficients (550 nm) and f(RH) From APP.

The green line is scattering coefficient ratios (RR/TSI) at 550nm measured at ambient AOS humidity. The blue line represents the ratio while the RR nephelometer is at 85% and the TSI at ambient (40%) RH.

This anti-correlation is not well represented in the literature. Scattering coefficients are very low during this time period, never exceeding 25 Mm^{-1}.

Several fire events have provided interesting humidograph data in which the f(RH) values have been at their highest. Figure 4.26 displays some of the humidograph data during a moderate sized fire southwest of APP.

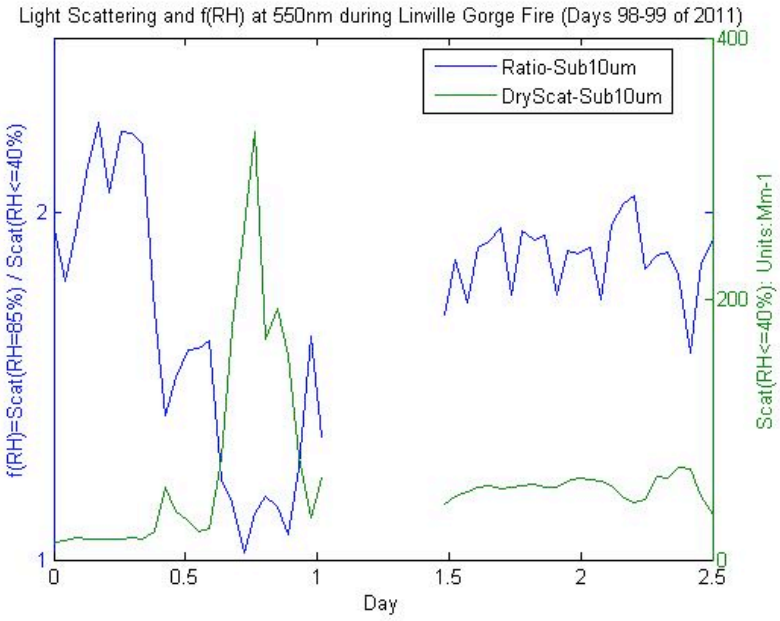

Figure 4.28. Light Scattering Coefficients and f(RH) at 550nm During Linville Gorge Fire. Days 98-99 of 2011

During this fire event the majority of the aerosols exhibited an average hygroscopic growth factor of slightly above 1. Figure 4.4.9 displays some of the humidograph data during a large fire event (~1,000 acres burned) roughly 90 miles southwest of the APP site.

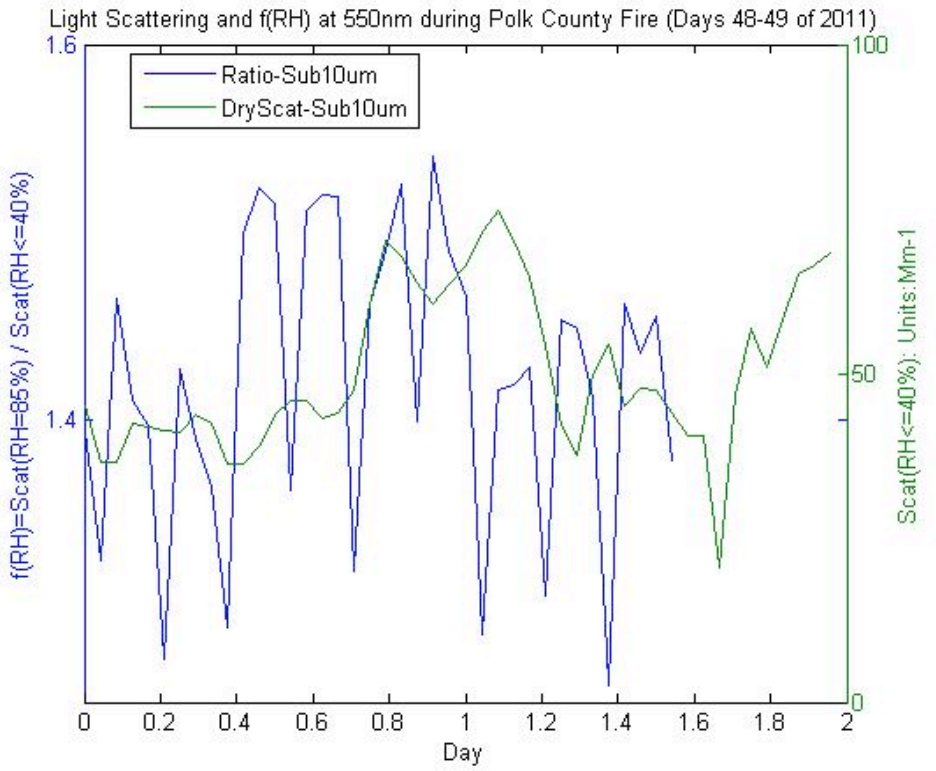

Figure 4.29. Light Scattering Coefficients and f(RH) at 550nm During Polk County Fire. Days of 48-49 of 2011.

4.5 Broadly Classified Aerosol Types Based on Cluster Analysis

Following a similar methodology to Taubman et al., (2006), a hierarchal agglomerative cluster analysis was performed to provide a better understanding of the aerosol types as cluster analyses have been shown to reduce ambiguities in aerosol-types analysis (Russell et al., 2010). Without direct chemical information, the results provide information on the sources impacting APP and their relative influences on the site (Penner et al., 1994).

4.5.1 Cluster Variables and Algorithm Synopsis

Based on the method explained in Taubman et al., (2006) using three aerosol optical property

variables, a three dimensional space defined by the three variables would allow a broad classification of aerosol types using an agglomerative cluster algorithm (Figure 4.30) in which aerosols of similar types would group together in the determined three-space.

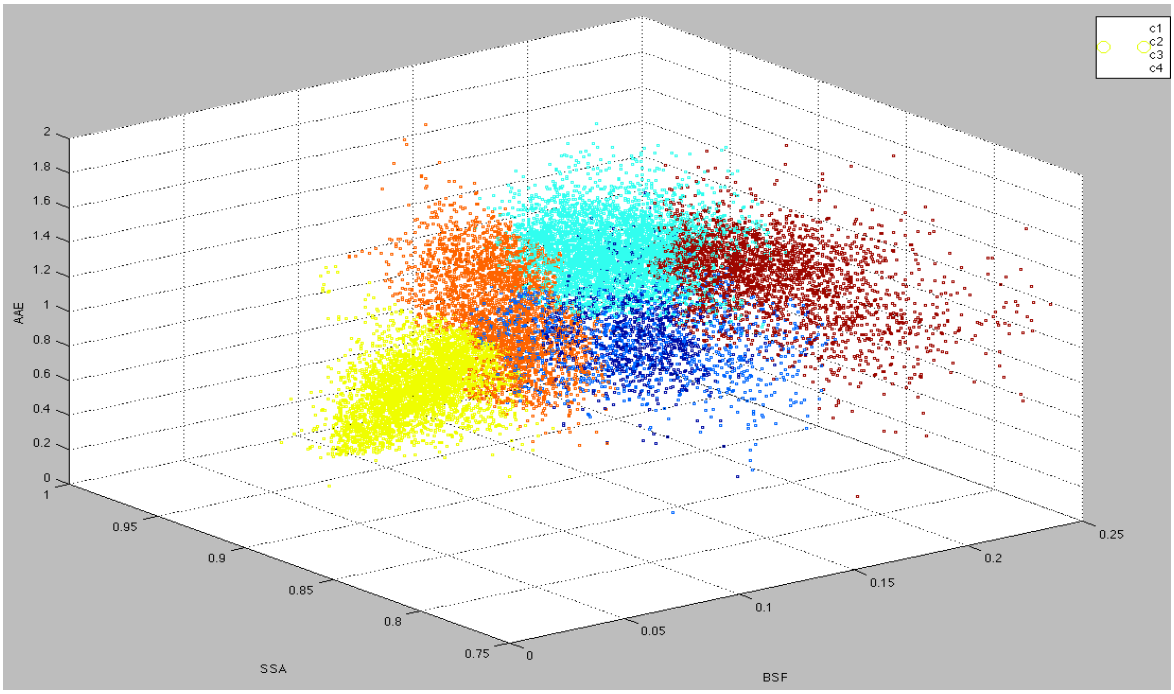

Figure 4.30. Three Dimensional Scatter Plot Illustrating Similar Aerosol Types by Color Using Total Data Set. Axes are defined as follows. Hemispheric backscatter fraction (*b*) (x-axis), Single-scattering albedo (SSA) (y-axis) and Absorption Ångström Exponent (AAE) (z-axis).

The variables being used in the cluster algorithm include Single-scattering albedo at 550 nm (SSA), hemispheric backscatter fraction (550nm) (*b*), and absorption Ångström exponent (400nm-700nm) (AAE). These variables were chosen as they adequately represent the optical and microphysical properties of various aerosol types and the values could be compared to previous research SSA describes roughly how white a particle is with

backscatter fraction providing indication of particle size and AAE exponent provides information regarding the relative amounts and age of OC and BC.

Following humidograph characterization, all data can be additionally binned by hygroscopic growth factors, which will prove useful in further distinguishing aerosol types based on the unique hygroscopicity of certain aerosol species.

The data sets represented in this section consist of the summer and winter data as they are most contrasting seasons, both of which using hourly averaged data. A concise explanation of the cluster algorithm follows. Plots from the other seasons as well as additional information including a flow chart of the cluster algorithm can be found in Appendix 4.

A standardized Euclidean distance shown in 4.2 is calculated between all pairs of data points while being normalized about the mean of each variable. Normalization was needed because of the dissimilarity in the magnitude and variability of the values used to calculate the distances.

$$D_{ij} = \sqrt{\sum_{k=1}^{n}\left(x_{ik} - x_{jk}\right)^2 + \left(y_{ik} - y_{jk}\right)^2 + \left(z_{ik} - z_{jk}\right)^2} \tag{4.2}$$

The distances were used to create an agglomerative hierarchal cluster dendrogram through using a Ward linkage function. Centroids representing the effective center of mass (centroid) of the cluster were determined by using the Ward linkage. This linkage calculates an

equivalent distance represented with 4.3 by calculating an index based on the distance between inter-cluster points of data and the distance between separate centroids.

$$d(i,j) = \sqrt{\frac{2n_i n_j}{(n_i+n_j)} \left\|\bar{x}_i - \bar{x}_j\right\|_2} \tag{4.3}$$

Centroids positions in the coordinate system determined by the three variables of interest are denoted with the notation $\bar{x}_i$ and $\bar{x}_j$ as they represent the average vector location for a cluster with n_i and n_j being the number of elements in a cluster. $\left\|\bar{x}_i - \bar{x}_j\right\|_2$ represents the Euclidean distance between centroids. Ward linkage method minimizes intra-cluster variance while maximizing the variance among disparate clusters via calculating the distance between cluster centroids, thereby partitioning aerosol particles of similar types together while separating disparate types into different clusters. The lowest equivalent distance represents the correct partitioning of aerosol types.

Cluster validation was achieved in previous studies by using the percent change in total root mean squared deviation (TRMSD) versus the number of clusters to determine the appropriate number of clusters (e.g., Taubman et al., 2006). According to these studies, the iteration prior to the steepest rate of change in TRMSD is the most likely candidate for the appropriate number of clusters and thereby the appropriate number of discrete aerosol types in the data set. In an attempt to remove some of the subjectivity in this step, the Davies-Bouldin (DB) index for cluster algorithm validation was used.

The DB index uses a measure of the dispersion within each cluster and a dissimilarity measure between clusters (Pascual et al., 2010), which complements the clustering method, as that is the basis for the Ward linkage function.

The DB index represented with 4.4, provides a means for establishing a quantitative number for cluster validation that is independent of algorithm development and data partitioning.

$$DB = \frac{1}{N}\sum_{i,j=1}^{N} R_{ij} \tag{4.4}$$

An indication of natural partitions in data sets occurs as the DB index is minimized following consecutive algorithm iterations (Davies and Bouldin, 1979) based on a similarity and dispersion value which is calculated for each cluster. Subscripts of i and j correspond to the respective variables and axis, in the case of this thesis three variables were used instead of two. The total number of data points is denoted by N and R_i represents the general cluster separation measure with respect to one variable. R_{ij} represents the general cluster separation measure with respect to all variables shown in 4.5.

$$R_{ij} = \frac{S_i + S_j}{M_{ij}} \tag{4.5}$$

M_{ij} is the Minkowski metric shown with 4.6 which represents the similarity or distance between centroids of clusters where the ideal cluster number would have the lowest Minkowski Metric value.

$$M_{ij} = \left\{\sum_{k=1}^{n_i} \left|a_{ki} - a_{kj}\right|^{p}\right\}^{1/p} \tag{4.6}$$

Since Euclidean distances are being calculated the exponential shown above in 4.6 are set at $p = 2$ (Davies and Bouldin 1979). The dispersion amongst cluster centroids are denoted with S_i and S_j represented with 4.7.

$$S_i = \left\{\frac{1}{n_i}\sum_{j=1}^{n_i}\left|n_j - \bar{x}_i\right|^q\right\}^{1/q} \tag{4.7}$$

$q = 1$ in the exponentials in 4.7 due to the use of Euclidean distance calculations (Davies and Bouldin, 1979). The dispersion amongst clusters should be maximized for the ideal number of clusters.

While to DB index adds objectivity to the determination of appropriate cluster it does not completely eliminate subjectivity from the process. If the calculated DB index was thought to be unrealistic (e.g. 1 cluster type) or indistinguishable by the instruments (e.g. 12 cluster types) caused by limitations in instrument capabilities, a reasonable cluster number would need to be determined by an investigator based the separation in mean values and the overall variance found in the statistical plots which were output by the cluster algorithm.

4.5.2 Cluster Analysis Using Summer Data

For all box-and-whisker plots in this section, the red center line is the 50th percentile, the box widths represent the 25th and 75th percentiles and the whiskers are the 99th and 1st percentiles. Summer plots of BSF (Figure 4.31), SSA (Figure 4.32), and AAE (Figure 4.33) are provided below prior to discussion.

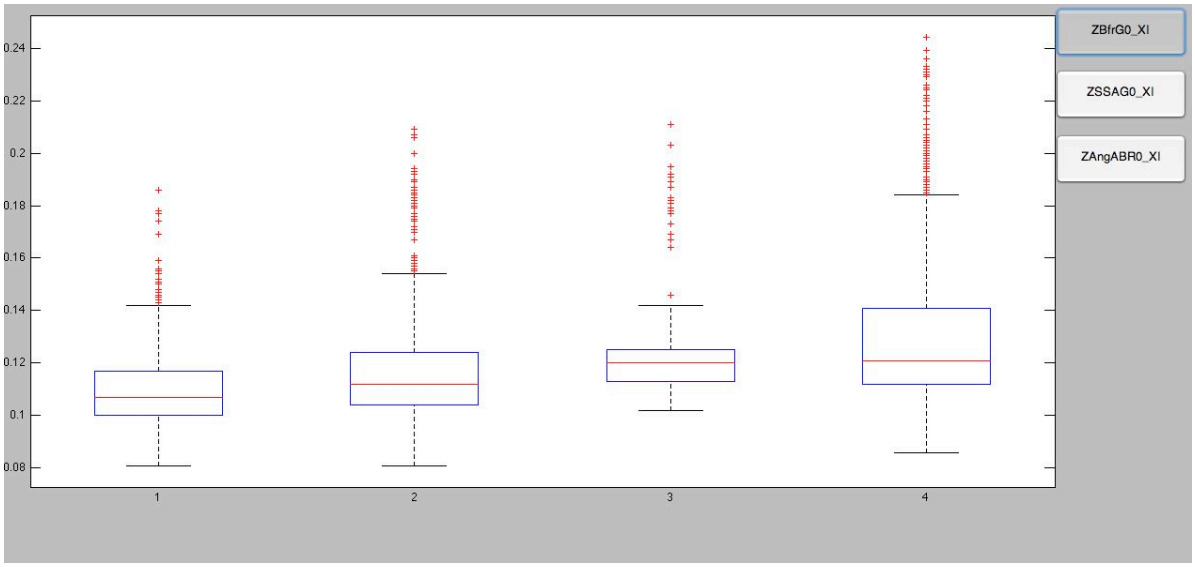

Figure 4.31. Aerosol Types Plot of (*b*) (550 nm) for Summer Data Using 4 Clusters.

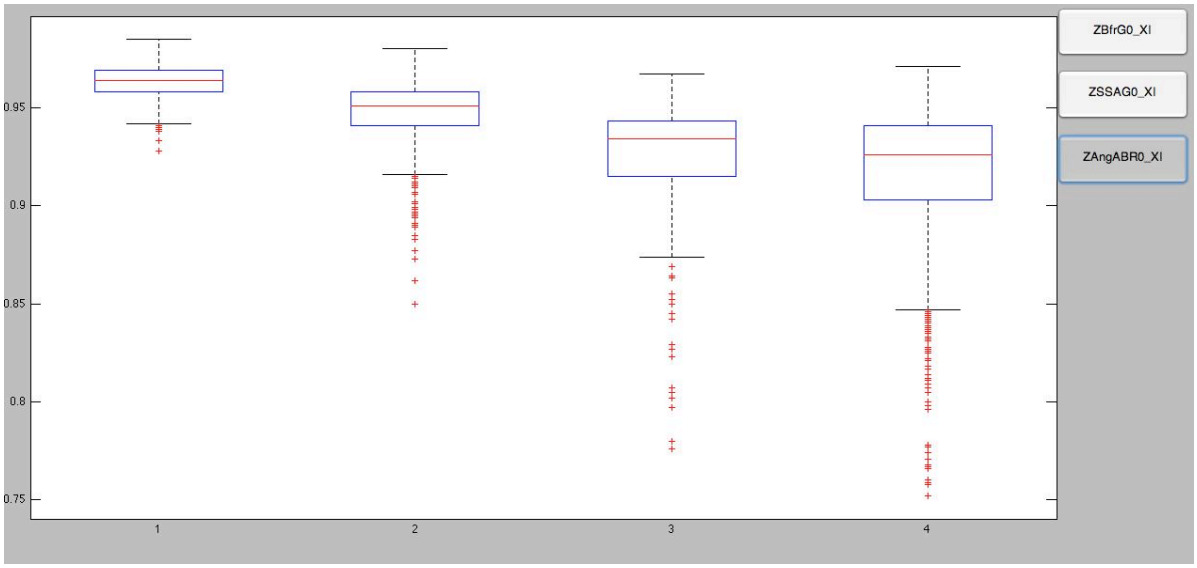

Figure 4.32. Aerosol Types Plot of SSA (550 nm) or Summer Data Using 4 Clusters.

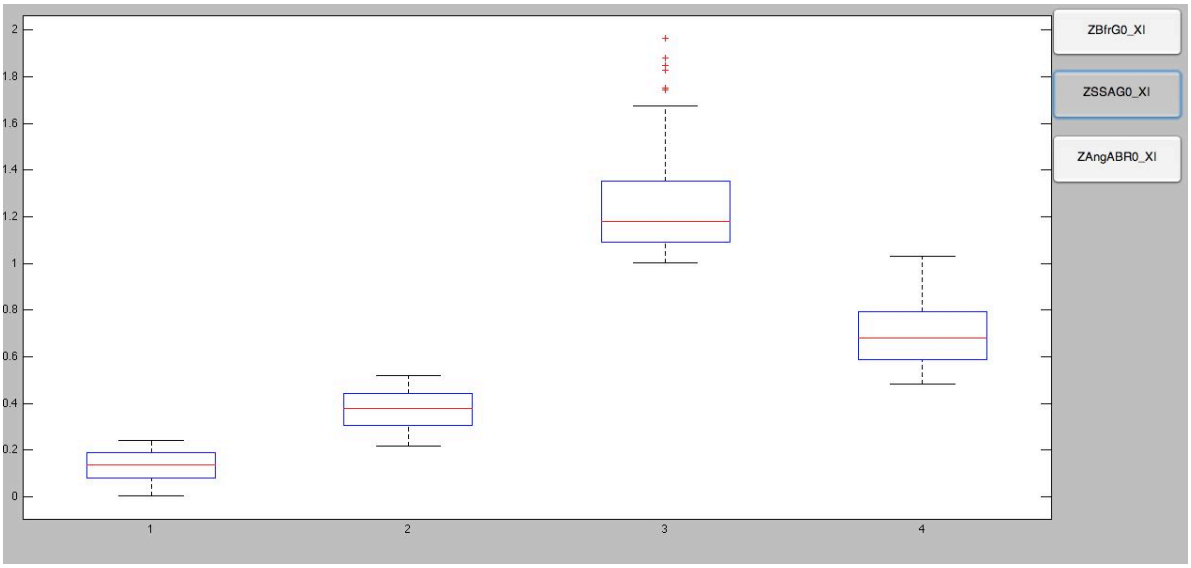

Figure 4.33. Aerosol Types Plot of AAE (450/700 nm) for Summer Data Using 4 Clusters.

The cluster analysis revealed 4 aerosol types during the summer months (Table 4.3). Type 4 could be considered an aged point source as the SSA and AAE values indicate very scattering particles with primarily OC. The larger size due to smaller *b* indicates that the particles are not fresh or close to the source proximity. Type 3 appears to be a fresh biomass type, as the low SSA and highest AAE values, coupled with large *b* values, indicate. Type 1, with the low AAE, low SSA and lower BSF may be an aged point source type. Type 2, having mid-values of SSA and AAE in between the others, this type seems represent a fresh mixed aerosol. All summer types are presented in Table 4.3.

Table 4.3. Broadly Classified Aerosol Types (4) Sampled During Summer (JJA) Months.

Summer Aerosol Types Cluster Results		
Type #	**Relative Lifetime**	**Possible Composition**
1	Aged	Point Source
2	Aged	Mixed Aerosol
3	Fresh	Biomass Burning
4	Fresh	Point Source

4.5.3 Cluster Analysis Using Winter Data

Winter plots of BSF (Figure 4.34), SSA (Figure 4.35), and AAE (Figure 4.36) are provided below prior to discussion.

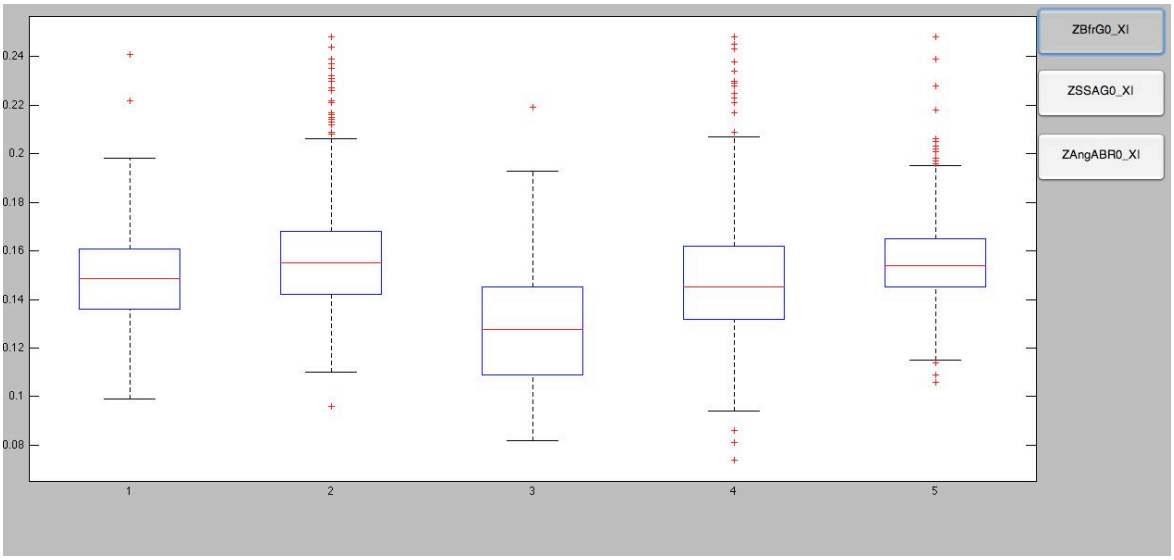

Figure 4.34. Aerosol Types Plot of (*b*) (550 nm) for Winter Data Using 5 Clusters.

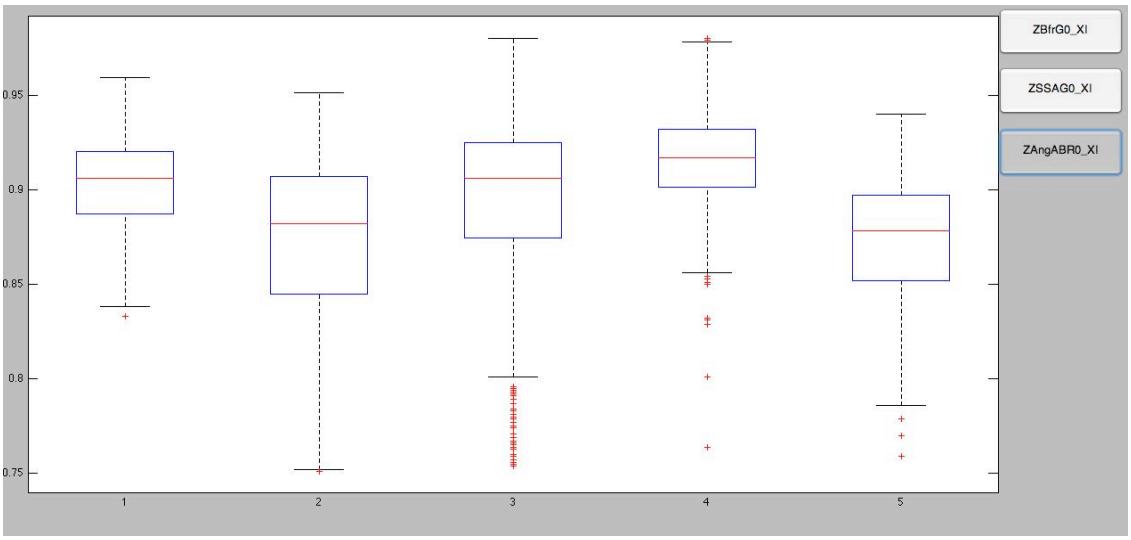

Figure 4.35. Aerosol Types Plot of SSA (550 nm) for Winter Data Using 5 Clusters.

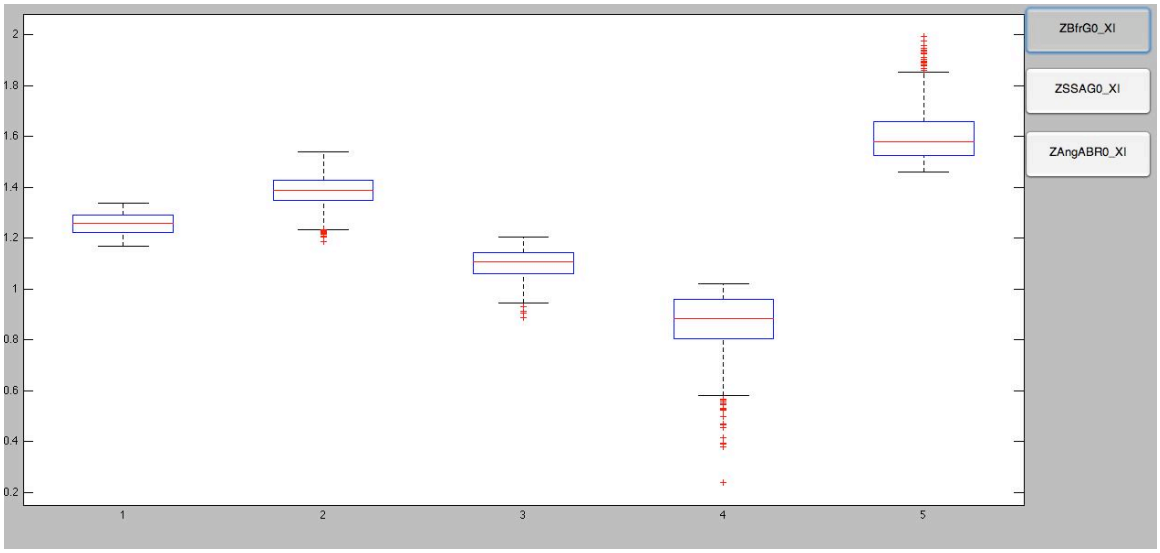

Figure 4.36. Aerosol Types Plot of AAE (450/700 nm) for Winter Data Using 5 Clusters.

5 aerosol types were determined based on the cluster algorithm for the winter data (Table 4.4).

Table 4.4. Broadly Classified Aerosol Types (5) Sampled During Winter (DJF) Months at APP

Winter Aerosol Types Cluster Analysis Results		
Type #	**Relative Lifetime**	**Possible Composition**
1	Aged	Mixture
2	Fresh	Biomass Burning
3	Aged	Mixture
4	Aged	Point Source
5	Fresh	Biomass Burning

Types1 and 3 are mixed based on those types having moderate values of AAE and SSA but having the lowest values of *b* which would correspond to a mixture of various particles while being larger in size with type 3 being slightly larger and more aged particles. Types 2 and 5 are very similar and are best defined as fresh biomass burning. The types have very similar values of SSA and *b*. However, the AAE for type 5 is the largest for the season which indicates that type to have the highest concentrations of OC. Lastly, type 4 most closely represents an aged point source. This type has the lowest AAE which indicates more BC than OC and it has the highest SSA. This combination may be indicative of an anthropogenic point source and since the particles are larger they likely are more aged than freshly emitted particles.

In the future, this analysis would be followed by a back trajectory analysis to link the aerosol types to their sourcing regions. This would provide further validation as to the validity of the

types classification while gaining an understanding of the contributions of those sourcing regions on the radiative effects measured at APP.

CHAPTER 5-FUTURE WORK AND IMPROVEMENTS TO RESEARCH

5.1 Transition From Satellite Derived MODIS To AERONET CIMEL Measurements

While MODIS provides many of the needed variables for calculating DRE, there are limitations in capabilities and precision when compared to ground based remote sensing means (Dubovik et al., 2000). Following fall 2011, APP will transition over to ground based measurements of AOD and cloud fraction, which will allow the capability to make all DRE calculations using "in house" variables.

5.2 Implementation of a LIDAR

To better understand the vertical profile and spatial distribution of aerosols through the column over APP, a micropulse LIDAR system has been implemented. However, at the time of this thesis, it had not provided a substantial amount of quantitative data. Eventually, the extracted data should provide information of the spatial distribution of certain aerosols, allowing the DRE calculations to be scaled appropriately, accounting for heterogeneous distributions through the column of atmosphere over APP.

5.3 Scanning Humidograph

The capabilities of our humidified light scattering measurements will be enhanced in 2012 through the implementation of a scanning humidograph. The Radiance Research

nephelometer will be replaced by a second TSI 3563 nephelometer. This configuration, while being more complex provides greater capability of measurements by being able to scan from 40 to 85% RH allowing for the sampling of all deliquescence points of aerosols. The RH of the sampling volume in the new instrument will be scanned from 40%-85% over a one-hour period, facilitating the measurements of a continuous aerosol hygroscopic growth curve. The major assumption in this technique is that any changes in aerosol properties during the one-hour scan period are negligible. Another advantage of using a second TSI nephelometer, as opposed to the RR nephelometer, is the capability for measuring the backscattered light; in addition to total light scattering. The hygroscopic dependence on hemispheric back-scattering (b) can be used to scale the upscatter fraction (equation 2.7) to ambient RH in DRE (equation 2.13) calculations. The ability to scale aerosol SSA and upscatter fraction (β) to ambient RH will serve to increase the accuracy of the DRE calculations made at APP.

5.4 Chemistry Instruments

With the addition of chemistry instruments, the distinction between anthropogenic and natural aerosol will finally be possible. Contribution of man-made pollution will be distinguishable from the sampled aerosols. This new data in combination with trajectory analysis will provide insight into the source region and source apportionment of the most radiatively sensitive particles.

The next steps to help increase App's efforts of more accurate and precise DRE calculation would be to use a more complex model such as the 4 stream model used by SBDART and to better understand the apportionment from source regions and types.

CHAPTER 6-SUMMARY AND CONCLUSIONS

From the research presented in this thesis there are several conclusions to be made. APP experiences the highest seasonal variability in aerosol extinction coefficients when compared to the other three continental NOAA-ESRL sites. This measured extinction at APP is being dominated by particles with sub-micrometer diameter aerosols that are exhibiting a high efficiency at scattering the incident shortwave radiation. This pronounced seasonality is consistent with the large summer formation of SOA from BVOCs and anthropogenic gaseous precursors (Goldstein et al., 2009).

A summer season driven, negative broadband radiative effect of roughly 10 Wm^{-2} was calculated based on the initial two years of data. Through continuous monitoring and advances in modeling complexity, the research at APP should advance the state of knowledge surrounding radiative effects and the associated sources in the SEUS.

While limited in days of operation, the humidograph has proven to provide some interesting data as APP experiences a higher hygroscopic growth effect for the three seasons of operation when compared to the annual mean values measured at the SGP site (Sheridan et al., 2001).

The initial broad classification results of aerosol types by cluster analysis revealed that APP samples a variety of aerosols with a wide range of optical properties throughout the year. These basic types range from both fresh to aged mixtures, point sources, and biomass burning with some variability between these types across the contrasting seasons. Changes of season result in a different number of types but with similar characteristics indicating that APP may be a baseline site for the SEUS. Further analysis through back trajectory cluster analysis should reveal the aerosol source regions and source apportionment which is needed to better understand the broadly classified types and the contributions of source regions on the radiative effects in the SEUS.

BIBLIOGRAPHY

Anderson T.L., and Ogren J.A.: Determining Aerosol Radiative Properties Using the TSI 3563 Integrating Nephelometer, Aerosol Science and Technology, 29:1,57-69, 1998.

Anderson, T. L., et al.,: Performance characteristics of a high-sensitivity, three-wavelength, total scatter/backscatter nephelometer, *J. Atmos. Oceanic Technol.,* 13, 967-968, 1996.

Anderson, T. L., Covert D. S., Wheeler J. D., Harris J. M., Perry K. D., Trost B. E., and Jaffe D. J.: Aerosol backscatter fraction and single-scattering albedo: Measured values and uncertainties at a coastal station in the Pacific NW, *J. Geophys. Res.,* 104, 26, 793-26, 807, 1998.

Bergstrom R.W., Pilewskie P., Russell P.B., Redemann J., Bond T.C., Quinn P.K., and Sierau B.: Spectral absorption properties of atmospheric aerosols, *J. Atmos. Chem. Phys*., Vol 7, 5937-5943, 2007.

Bohren C. F. and Huffman D. R.,: Absorption and Scattering of Light by Small Particles. John Wiley & Sons, Inc., New York, NY, 1983.

Bond, T. C., Anderson T. L., and Campbell D.: Calibration and intercomparison of filter-based measurements of visible light absorption by aerosol, *Aerosol Sci. Technol.*, 30, 582-600, 1999.

Cappa C.D., Lack D.A., Burkholder J.B., and Ravishankara A.R.: Bias in Filter-Based Aerosol Light Absorption Measurements Due to organic Aerosol Loading: Evidence from Laboratory Measurement. *Aerosol Sci. and Technol*. 42,:12, 1022-1032, 2008.

Carrico, C. M., Rood M. J., and Ogren J.A.: Aerosol light scattering properties at Cape Grim, Tasmania, during the first Aerosol Characterization Experiment (ACE 1), *J. Geophys. Res*., 103, No. D13, pp. 16,565-16,574, 1998.

Charlson R.J., Schwartz S.E., Hales J.M., Cess R.D., Coakley J.A., Hansen J.E., and Hofman D.J.: Climate Forcing by Anthropogenic Aerosols, *Science*, 255, 423-430, 1992.

Davies, D.l., and Bouldin, D. W.: A Cluster Separation Measure, IEEE Transactions on Pattern Analysis and Machine Intelligence, Vol. Pami-1, No.2, 1979.

Dubovik, O., Smirnov A., Holben B. N., King M. D., Kaufman Y. J., Eck T. F., and Slutsker I.: Accuracy assessments of aerosol optical properties retrieved from Aerosol Robotic Network (AERONET) Sun and sky radiance measurements, *J. Geophys. Res*., 105, 1135-1150, 2000.

Delene D.J., and Ogren J.A.: Variability of aerosol optical properties at four North American Surface Monitoring Sites *J. Atmos. Sci*., 59, 9791-9806, 2001.

Goldstein A.H, Koven C.D., Heald C.L., and Fung I.Y.: Biogenic carbon and anthropogenic pollutants combine to form a cooling haze over the southeastern United States. PNAS 2009.

Haywood J. M. and Shine K.P.: Multi-spectral calculations of the direct radiative forcing of tropospheric sulfate and soot aerosols using a column model. *Q. J. R. Meteorological*. Soc. Vol 123, No. 543, 1907-1930, 1997.

Haywood J.M. and Shine K.P.: The effect of anthropogenic sulfate and soot aerosol on the clear sky planetary radiation budget, Geophysical Research Letters, 22, 5, 603-606, 1995.

Holben, B.N., Eck T. F., Slutsker I., Tanré D., Buis J. P., Setzer A., Vermote E., Reagan J. A., Kaufman Y. J., Nakajima T., Lavenu F., Jankowiak I., and Smirnov A.: A federated instrument network and data archive for aerosol characterization, Remote Sens. Env., 66, 1-16, 2008.

IPCC: Climate Change 2007: The Physical Science Basis. Contribution of Working Group 1 to the Fourth Assessment report of the Intergovernmental Panel on Climate Change [Solomon, S., D. Qin, M. Manning, Z. Chen, M. Marquis, K.B. Averyt, M. Tignor and H.L. Miller (eds.)]. Cambridge University Press, Cambridge, United Kingdom and New York, NY, USA, 2007.

Kim J., Yoon S-C., Jefferson A., and Kim S.W.: Aerosol hygroscopic properties during Asian dust, pollution, and biomass burning episodes at Gosan, Korea in April 2001. *J. Atmos. Environment*, 40, 1550-1560, 2006.

Jeong, M.J., Li, Z., Andrews E., and Tsay S.C.: Effect of aerosol humidification on the column aerosol optical thickness over the Atmospheric Radiation Measurement Southern Great Plains site, *J. Geophys. Res.*, 112, D10202, doi:10.1029/2006JD007176., 2007.

Kahn R. A., Nelson D.L., Garay M. J., Levy R.C., Bull M.A., Diner D.J., Martonchik J.V., Paradise S.R., Hansen E.G., and Remer L.A.: MISR Aerosol Product Attributes and Statistical Comparisons with MODIS, *IEEE Transaction of Geoscience and Remote Sensing***,** 47(12), 4095-4114, 2009.

Kiehl, J.T., and Briegleb, B.P.: The Relative Roles of Sulfate Aerosols and Greenhouse Gases in Climate Forcing. *Science* 2600, 311-314, 1993.

Koloutsou-Vakakis S.: Aerosol particle light scattering at a perturbed mid-latitude continental northern hemispheric site and its dependence on relative humidity, wavelength of light, particle size and composition, Ph.D. dissertation, 162pp., Dep. of Civ Eng., Univ of Ill. at Urbana-Champaign, 1996.

Koloutsou-Vakakis S., Carrico C.M., Kus P., Rood M.J., Li Z., and Shrestha R.: Aerosol Properties at a midlatitude Northern Hemisphere continental site, *J. Geophy. Res.*, 106, D3, 3019-3032, 2001.

Koontz A.S. and Ogren J.A.: ARM AOS Processing Status and Aerosol Intensive Properties VAP. Thirteenth ARM Science Team Meeting Proceeding, Broomfield, Colorado, March 31-April 4, 2003.

Lewis K., Arnott W., Moosmüller H., and Wold C.E.: Strong spectral variation of biomass smoke light absorption and single scattering albedo observed with a novel dual-wavelength photoacoustic instrument. *J. Geophys. Res.*, Vol. 113, doi:10.1029/2007JD009699, 2008.

Levy R.C., Remer L.A., Kleidman R.G, Matoo S., Ichoku C., Kahn R., and Eck T.F.: Global evaluation of the Collection 5 MODIS dark-target aerosol products over land. *J. Atmos. Chem. and Phys.*, 10, 10399-10420., 2010.

Muller T. et al.: Angular Illumination and Truncation of Three Different Integrating Nephelometer: Implications for Empirical, Size-Based Corrections, *Aerosol Science and Technology*, 43:6,581-586, 2009.

Pascual D., Pla F., Sánchez J.S..: Cluster Validation using information stability measures, Pattern Recognition Letters, 31, 454-461, 2010.

Payton A.M. et al.: An Empirical Approach to Aerosol Model Development for Radiative Transfer Calculations, Fourteenth ARM Science Team Meeting Proceedings, Albuquerque, New Mexico, March 22-26, 2004.

Penner, J.E., Charlson R..J., Hales J.M., Laulainen N.S., Leifer R., Novakov T., Ogren J., Radke L. F., Schwartz S. E., and Travis L.: Quantifying and minimizing uncertainty of climate forcing by anthropogenic aerosols. *Bull. Am. Meteorl. Soc., 75*, 375-400, 1994.

Pereira, S., Wagner, F., and Silva, A.: Seven years of measurements of aerosol scattering properties, near the surface, in the southwestern Iberia Peninsula, *J. Atmos. Chem. Phys.*, 11, 17–29, 2011.

Portmann R.W., Solomon S., Hegerl G.C.: Spatial and seasonal patterns in climate change, temperatures and precipitation across the United States, PNAS 2009.

Russell P.B., Livingston J.M., Redemann J., Schmid B., Ramirez S.A., Eilers J., Kahn R., Chu A., Remer L., Quinn P.K., Rood M.J., and Wang .W.: Multi-Grid Cell Validation of Satellite Aerosol Property Retrievals in INTEX/ITCT/ICARTT 2004, *J. Geophys. Res*., 112, D12S09, doi:10.1029/2006JD007606, 2007.

Russell P.B., R.W. Bergstrom, Y. Shinozuka, A.D. Clarke, P.F. Decarlo, J.L. Jimenez, Livingston J. M., Redemann J., Dubovik O., and Strawa A.: Absorption Angstrom Exponent in Aeronet and related data as an indicator of aerosol composition, *J. Atmos. Chem. Phys*., 10, 1155-1169, 2010.

Saxena V.K. and Menon S.: Sulfate-Induced cooling in the southeastern U.S.: An Observational Assessment. *Geophysical Research Letters*, 26,16, 2489-2492, 1999.

Schnaiter, M., Gimmler, M., Llamas, I., Linke, C., and Schurath U.: Strong spectral dependence of light absorption by aerosols utilizing a UV-VIS extinction cell, *Aerosol Sci. Technol.*, 39:3, 249-260, 2005.

Seinfeld, J.H., and Pandis S.N.: Atmospheric Chemistry and Physics (2nd Edition), John Wiley & Sons, Inc., Hoboken, NJ, 2006.

Sheridan P. J., Delene D.J., and Ogren J.A.: Four years of continuous surface aerosol measurements from the Department of Energy's Atmospheric Radiation Measurement Program Southern Great Plains Cloud and Radiation Testbed site, *J. of Geophysical Research*, 106 (D18), 20735-20747, 2001.

Sheridan, P.J., and Ogren J.A.: Observations of the vertical and regional variability of aerosol optical properties over central and eastern North America. *J. Geophys. Res.*, 104, 16,793-16,805, 1999.

Taubman B. F.: Airborne Characterization of Regional Aerosol Origins and Optical Properties. Ph.D. dissertation., Dep. of Chemistry, Univ. of Maryland, College Park, Maryland, USA., 2004.

Taubman B. F., Hains J.C., Thompson A.M., Marufu L.T, Doddridge B.G., Stehr J.W., Piety C.A., and Dickerson R.R.: Aircraft vertical profiles of trace gas and aerosol pollution over the mid-Atlantic United States: Statistics and meteorological cluster analysis. *Journal of Geophysical Research*, 111, DS10S07. doi:10.1029/2005JD006196, 2006.

Taubman, B.F., L.T. Marufu, B.L. Vant-Hull, C.A. Piety, B.G. Doddridge, R.R., Dickerson, and Z. Li: Smoke over haze: Aircraft observations of chemical and optical properties and the effects on heating rates and stability, *J. Geophys. Res.*, 109, D02206, doi:10.1029/2003JD003898, 2004a.

Wiscombe, W.J., and Grams G.W.: The backscattered fraction in two-stream approximations *J. Atmos Sci*., 33, 2440-2451, 1976.

APPENDIX I.1

Statistical plot of UTC diurnal aerosol light absorption coefficients measured at 550 nm.

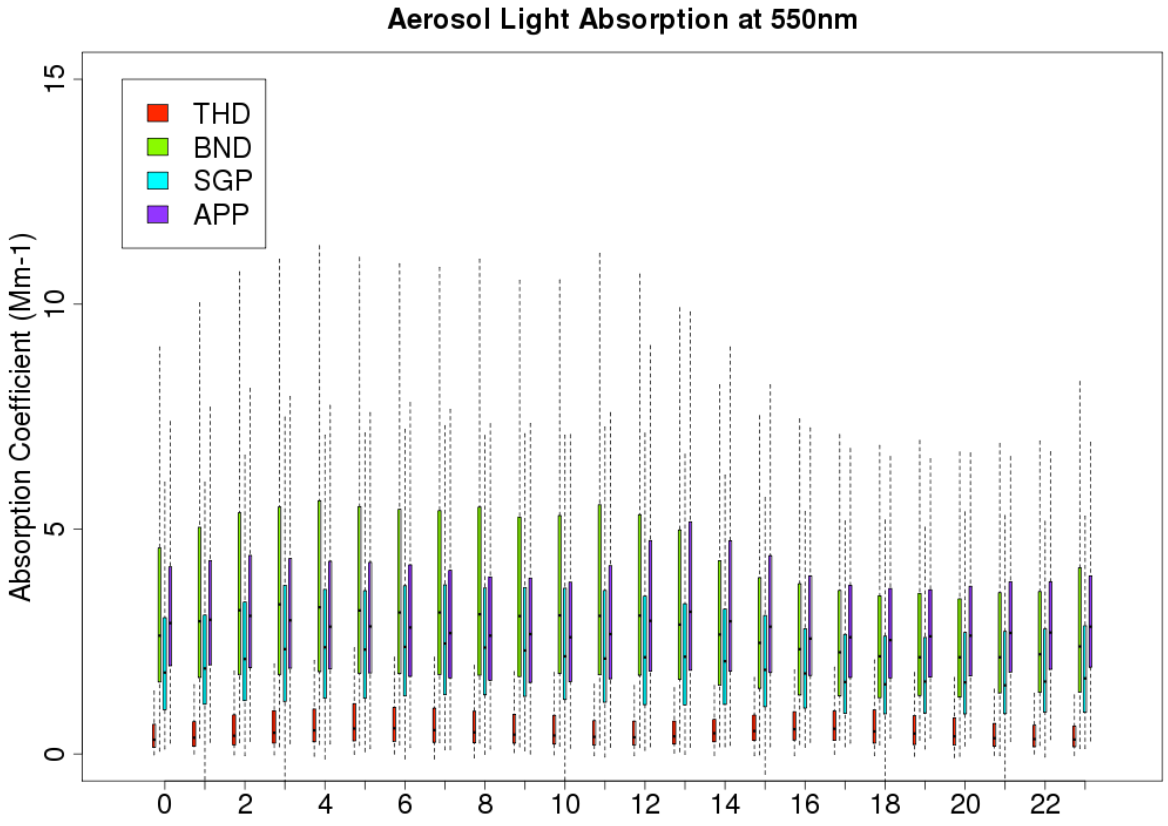

APPENDIX 1.2

Statistical plot of UTC diurnal aerosol total light scattering coefficients measured at 550 nm.

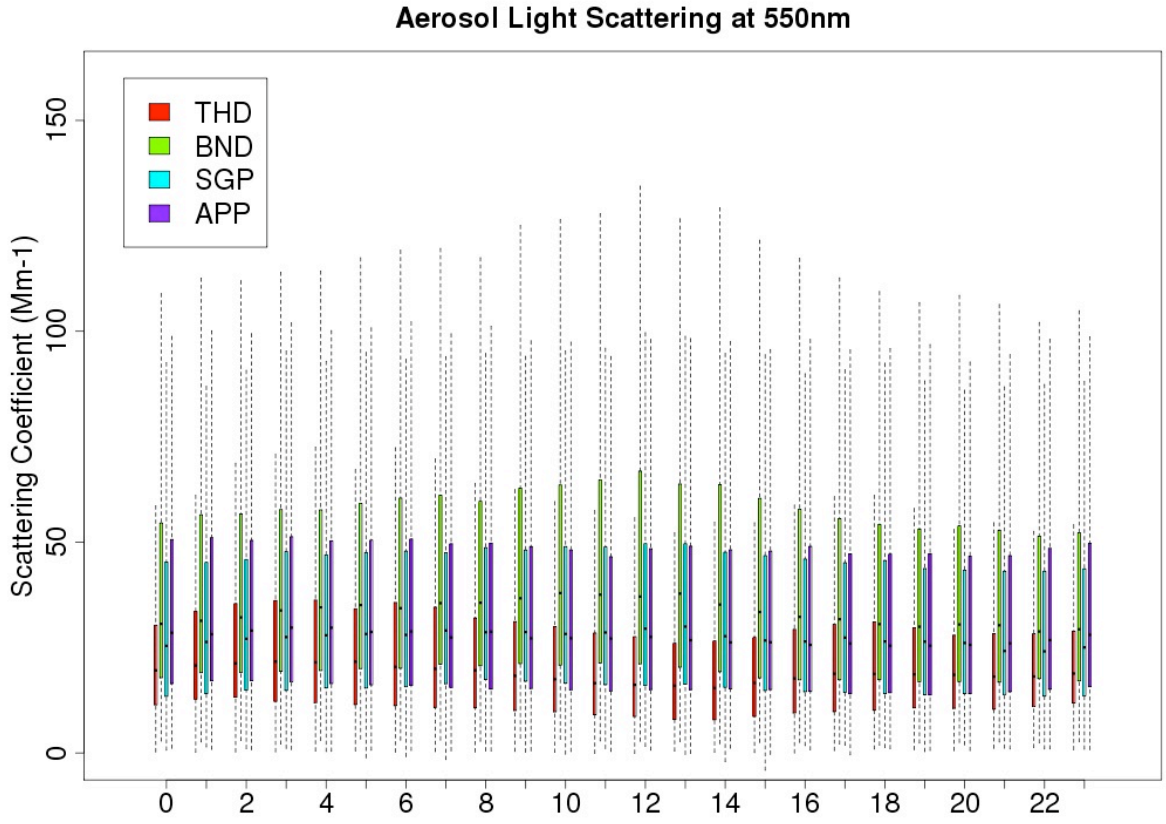

APPENDIX 1.3

Statistical plot of multi-station monthly binned aerosol light extinction coefficients measured at 550 nm.

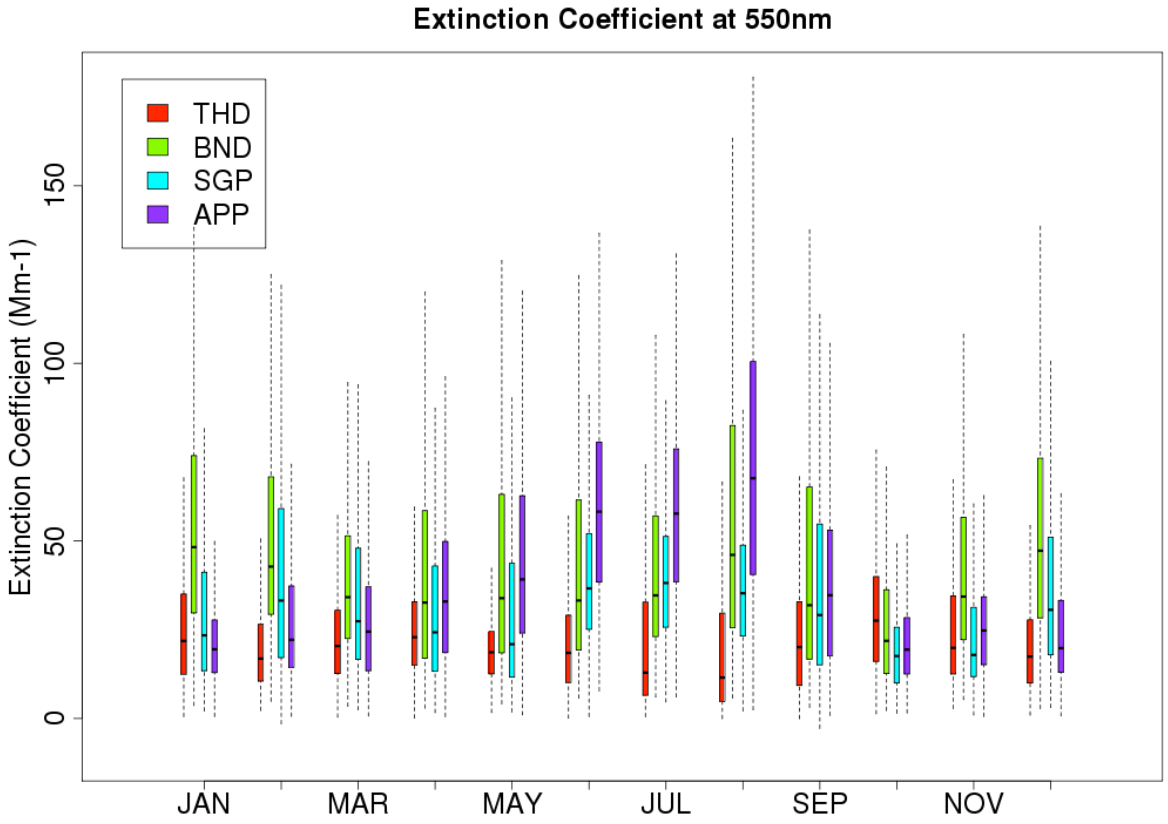

APPENDIX 1.4

Statistical plot of multi-station monthly binned aerosol light hemispheric backscatter coefficients measured at 700 nm.

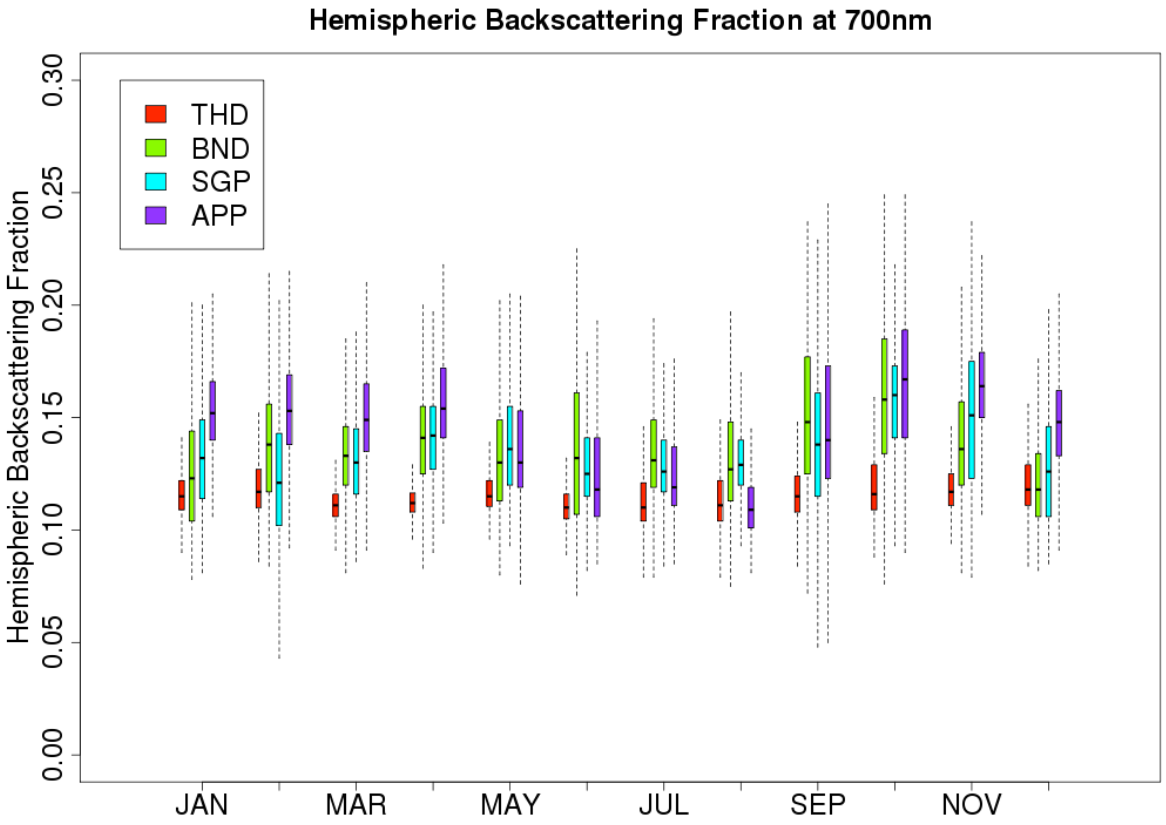

APPENDIX II.1

DB Index plot following cluster algorithm using summer data.

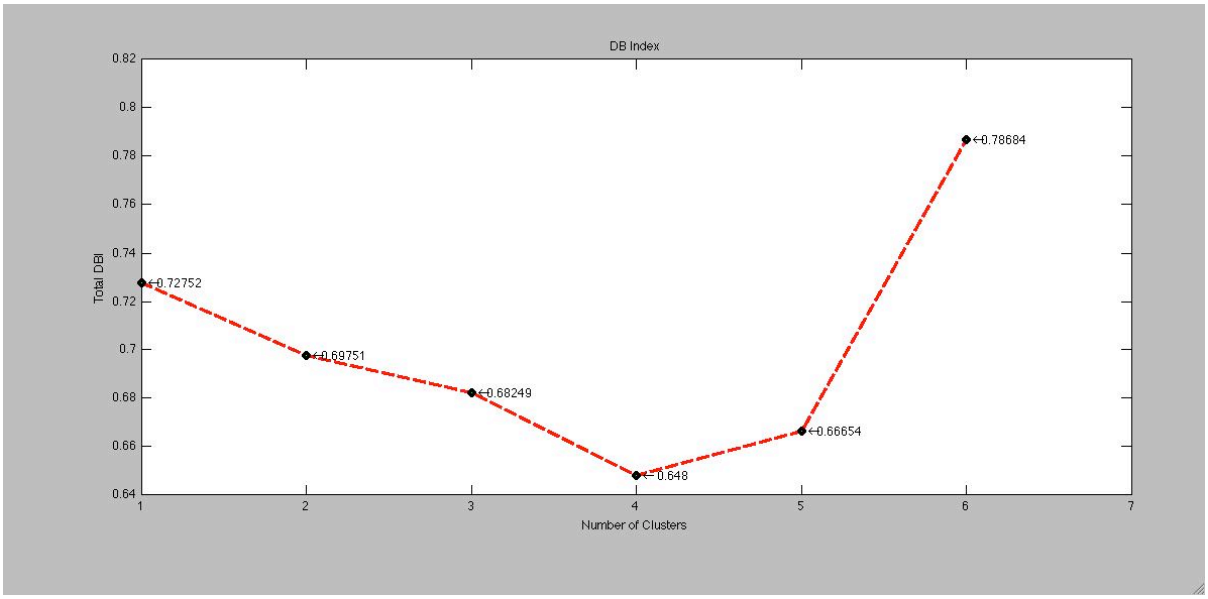

APPENDIX II.2

Cluster algorithm simplified flow chart.

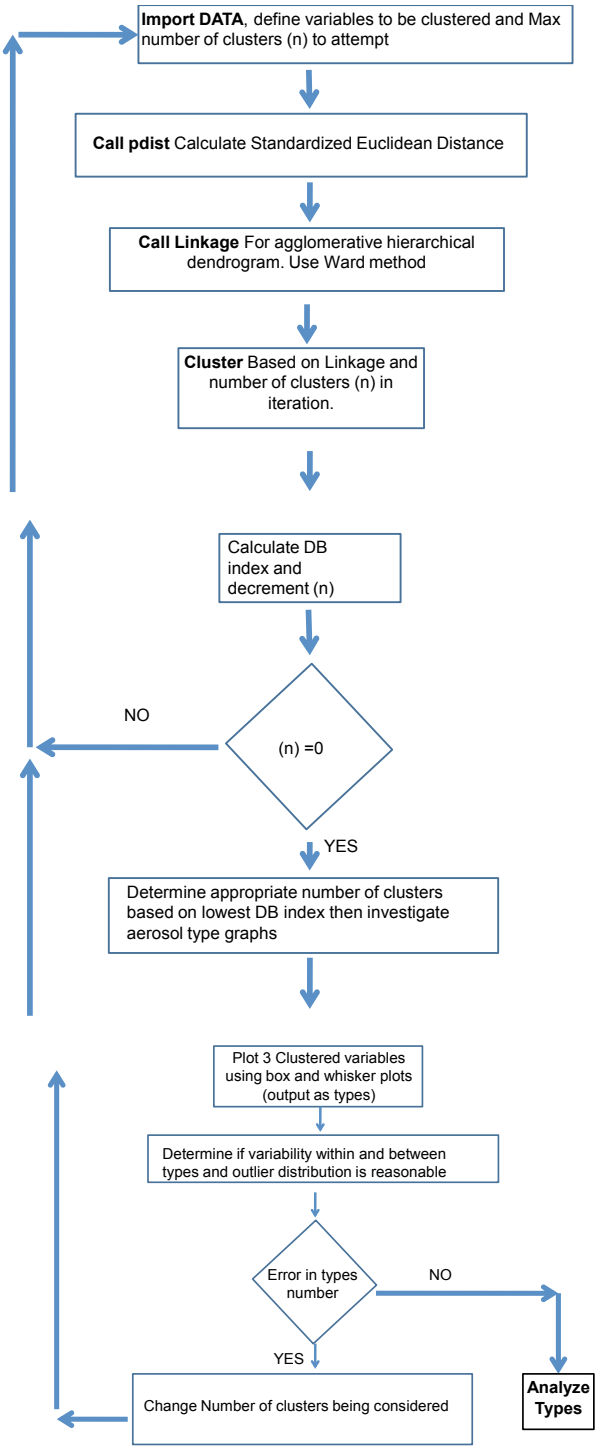

VITA

A native of North Carolina, William Bullitt Beuttell, Jr., was born in Banner Elk in1985. He graduated from Avery County High School in 2003 and enrolled at Appalachian State University in Boone, North Carolina, to pursue his Bachelor of Science in Applied Physics, which he received in 2008 while being a member of the varsity wrestling team. He then matriculated as a graduate student at Appalachian State to pursue a Master of Science in Engineering Physics with a Professional Science Master's Concentration in Instrumentation and Automation. He received his Master's degree in 2011.

While attending Appalachian, Will held a GRAM, Graduate Research Assistantship with AppalAIR, the Appalachian Atmospheric Interdisciplinary Research group and began his own business farming local hops, which he marketed to local home brewers and breweries. Will is a member of Sigma Pi Sigma Honor Society. Upon graduation with his Master's degree, Will received an Application Engineer position in the Renewable Energy group with Campbell Scientific, Inc., in Logan, Utah.